Åbo Akademi University

Jonne Niemi

Effects of Temperature Gradient on Ash Deposit Aging and Heat Exchanger Corrosion

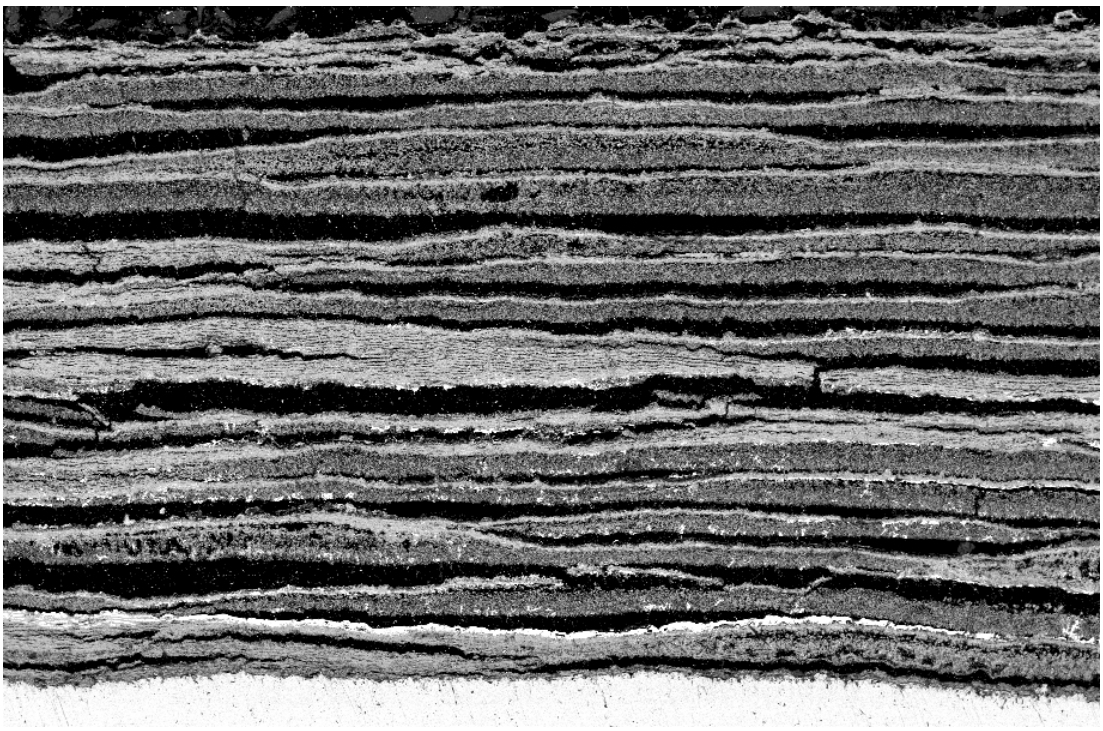

Effects of Temperature Gradient on Ash Deposit Aging and Heat Exchanger Corrosion

Jonne Niemi

Inorganic Chemistry

Faculty of Science and Engineering

Åbo Akademi University

Supervisors

Prof. Daniel Lindberg
Aalto University

D.Sc. Markus Engblom
Åbo Akademi University

Prof. Mikko Hupa
Åbo Akademi University

Opponent and Reviewer

Associate professor, Markus Broström
Umeå University

Reviewer

Associate professor, Peter Arendt Jensen
Technical University of Denmark

ISBN 978-952-12-3865-9 (printed)

ISBN 978-952-12-3866-6 (digital)

Painosalama Oy – Turku, Finland 2019

"Some writers enjoy writing, I am told. Not me. I enjoy having written."

— George R.R. Martin

Preface

This thesis work was carried out at the research group of Inorganic Chemistry of Åbo Akademi University and was funded mainly by the Graduate School in Chemical Engineering (GSCE). The work was also partly funded by Academy of Finland ("Behavior and properties of molten ash in biomass and waste combustion", Decision no. 266384, "Chemistry of biomass impurities at reducing conditions in future thermal conversion concepts" Decision no. 269277, and "Understanding the dynamics of intradeposit chemistry and morphology for control of corrosion in high temperature processes" Decision no. 310266). The work was also supported by the CLIFF (2014–2017) and CLUE (2017-2019) projects as part of the activities of the Åbo Akademi University Johan Gadolin Process Chemistry Centre. Other research partners were VTT Technical Research Centre of Finland Ltd, Lappeenranta University of Technology, Aalto University and Tampere University of Technology. Support from the National Technology Agency of Finland (Tekes, now Business Finland), ANDRITZ, Valmet Technologies Oy, Amec Foster Wheeler Energia Oy (now Sumitomo SHI FW Energia Oy), UPM-Kymmene Corporation, Clyde Bergemann GmbH, International Paper, Fortum, and Top Analytica Oy Ab is gratefully acknowledged. In addition, the financial support from the Åbo Akademi Rector Scholarship, the Swedish Academy of Engineering Sciences in Finland (STV), the Finnish Foundation for Technology Promotion, the Ella and Georg Ehrnrooth Foundation, and the Waldemar von Frenckells stiftelse is gratefully acknowledged.

I would like to express my gratitude to everyone that has helped and supported me during this journey. First, I would like to express my thanks to my supervisors, Prof. Mikko Hupa, Prof. Daniel Lindberg, and D.Sc. Markus Engblom for taking the time and guiding me during my thesis work. Your input and guidance have been invaluable, while at the same time you have given me freedom in my work and room to grow. It has been a pleasure to work with you in a supporting and inspirational working environment. I would also like to thank Prof. Leena Hupa for the positive feedback and encouragement during these years.

I am grateful to all the people who have contributed to the work presented in this thesis. I would like to thank D.Sc. Juho Lehmusto for good advice and great company. The educational and fun discussions (usually revolving around beer) have been the highlights of my workdays. I would like to thank Roland Balint for all the help and diligent work with the experiments and analysis of the results. I

would like to express my gratitude to D.Sc. Sonja Enestam and D.Sc. Hanna Kinnunen for the fruitful collaboration that has lifted the scientific value of the work and provided an essential connection to the industry. I am grateful to D.Sc. Patrik Yrjas for his comments and for the help he has provided me during the thesis work.

I would like to thank Tor Laurén and Jaana Paananen for all the help they have provided me during the years and for making everything run smoothly with the experimental equipment. Linus Silvander is gratefully acknowledged for the extraordinary patience and skill with the SEM/EDX analyses. Similarly, Peter Backman is gratefully acknowledged for carrying out the DSC/TGA analyses.

The time I spent in Toronto in 2016 is especially fondly remembered and I am grateful to Prof. Honghi Tran for inviting me to the University of Toronto and for providing me with excellent supervision and comments during and after my stay. Thank you also to Sue Mao and the rest of the gang at the U of T for making my time there both impactful and enjoyable.

I am grateful for the support and company of all the colleagues at our research group. Thank you especially to Meheretu Jaleta Dirbeba! You have been a great person to share an office with, always calm and positive in your attitude, and willing to listen to all sorts of problems and happy news. We have had many great discussions during these years and I am looking forward to many more!

While my colleagues and financiers made the work possible, I would not have finished this thesis without the emotional support from my family and friends. I would like to thank my parents and my brothers for providing me with the tools and confidence in my capability and in myself. I also want to express my gratitude to my friends, Janne, Moona, Jussi, Suvi, Kaarle, and Hanna. In addition, I am grateful to all the "Kermistit" and to the D&D group. All of you are thanked for the best of company and for providing much-needed relaxation during these past years!

Finally, the biggest thank goes to my beloved Mia, Siri, and Ebba. However frustrated or tired I have been, you always have a way of putting a smile on my face! This thesis would not have been completed without your tremendous support, thank you!

October 2019

Åbo

Abstract

Boilers firing biomass and/or waste-derived fuel have in general lower electrical efficiencies compared to coal-fired boilers. The root cause for the lower electrical efficiency lies in the high-temperature corrosion of the boiler heat exchanger tubes. The high corrosion rate in biomass and waste-fired boilers is tied to the ash composition of those fuels. The ash from the fuel forms deposits on the heat exchanger tubes of the boilers. The ash deposit composition and the heat exchanger material temperature are key parameters affecting the high-temperature corrosion. In order to minimize the corrosion risk, the final steam temperature, ergo, the material temperature is kept at a lower temperature in boilers combusting fuels with challenging ash compositions, which results in lower efficiency.

This work concentrates on ash deposit aging mechanisms as well as on high-temperature corrosion occurring in industrially relevant temperature gradients. The aging mechanisms were studied in laboratory scale and mathematical modeling was applied to validate the aging mechanisms observed in the laboratory experiments. The laboratory work revolved around synthetic alkali halide-alkali sulfate mixtures, relevant for biomass firing boilers and for black liquor recovery boilers. In addition, the behavior and interactions of $PbCl_2$ with alkali salts, relevant for waste-firing, in a temperature gradient were studied. The high-temperature corrosion of P235GH carbon steel and 10CrMo9-10 low alloyed steel was studied.

The main experimental equipment was a laboratory-scale temperature gradient probe. The probe is air-cooled and during exposure, it is inserted into a hot tube furnace, resulting in a temperature gradient from the furnace air to the probe. The probe houses two sample rings, which are covered with a deposit material. In addition, an entrained flow reactor (EFR) was used to form synthetic ash deposits on an air-cooled probe and to study the aging of the deposits. With both the temperature gradient furnace and the EFR, after exposure, the sample rings and the deposits were cut for a cross-section and analyzed using Scanning electron microscopy/Energy-dispersive X-ray spectroscopy (SEM/EDX).

Ash deposit aging was observed to occur both in the liquid and in the gas phase. Liquid phase sintering is known from earlier studies to affect the deposit density and removability. In addition to the densification of the deposits, the results from the laboratory experiments show that liquid phase sintering in a temperature gradient results in local species enrichment within ash deposits. The enrichment occurs when the liquid phase migrates within the deposits, filling pores and

solidifying in lower temperatures. In addition, temperature gradient zone melting phenomenon was observed to occur within the synthetic ash deposits. The phenomenon results in a species migration within a liquid phase due to a temperature gradient induced difference in the melt composition, i.e. concentration gradient within the liquid phase. The practical implications of the temperature gradient zone melting phenomenon are still unclear and further research on the topic is suggested.

Gas phase migration of alkali halides was observed to occur within the synthetic ash deposits when exposed to temperature gradients. The phenomenon was concluded to be due to the concentration gradient of alkali halides within the gas phase. The concentration gradient is induced by the temperature gradient and the temperature dependence of the partial pressures of the alkali halides. The partial pressure is higher in higher temperatures, which leads to diffusion of alkali halides from the higher temperature region to the lower temperature region. The mechanism was confirmed by modeling.

$PbCl_2$ was observed to migrate to and within ash deposits and to interact with alkali salts. $PbCl_2$ together with NaCl resulted in a formation of a eutectic melt but did not form new compounds. $PbCl_2$ and Na_2SO_4 reacted and formed caracolite ($Na_3Pb_2(SO_4)_3Cl$) and NaCl. $PbCl_2$ reacted with both KCl and K_2SO_4 and formed K-Pb-Cl species. In addition, $PbCl_2$ and K_2SO_4 were observed to react and form a caracolite type compound ($K_3Pb_2(SO_4)_3Cl$), which so far has not been corroborated to exist in the literature.

The corrosion mechanisms induced by alkali chlorides and alkali bromides were similar in nature and in line with the literature. The halides react with the steel and form metal halides, which have the potential to form low melting mixtures with alkali halides and/or lead chloride species. With alkali halides, fast corrosion rates were observed with steel temperature at 500 °C, while the steel temperature of 400 °C or lower resulted in slow corrosion. When lead chloride species were present in the deposit, a steel temperature of 400 °C led to catastrophic corrosion. Pure $PbCl_2$ was observed to be more corrosive than K-Pb-Cl species.

In light of the results of this thesis, ash deposit aging has the potential to affect the corrosive properties of ash deposits. In addition, the deposit density is likely to be affected, resulting in harder deposits, which are challenging to remove. This work shows that temperature gradients induce ash deposit aging mechanisms, which can drastically alter the deposit properties. Indications of the aging mechanisms have been reported before. However, this work makes an effort to systematically study the said effects and provide a broader understanding of their detailed nature and the relevance to boiler operation and design.

Svensk sammanfattning

Ångpannor som använder biomassa eller avfall som bränsle för att producera el har generellt lägre verkningsgrad än stenkolsbaserade ångpannor. Den huvudsakliga orsaken till den lägre verkningsgraden är att temperaturen i värmeväxlartuberna är lägre för att förhindra högtemperaturkorrosion. Biomassa och avfall orsakar vid förbränning påskyndad korrosion på grund av asksammansättningen. Askan från bränslen kan bilda askbeläggningar på värmeväxlartuberna. Askbeläggningens sammansättning och värmeväxlarmaterialens temperatur är nyckelparametrar som påverkar högtemperaturkorrosionen.

Avhandlingen studerar fenomen som påverkar askbeläggningarnas sammansättning och högtemperaturkorrosion vid en temperaturgradient. Fenomenen studerades i laboratorieskala och med hjälp av matematisk modellering, som användes för att bekräfta och validera de observerade fenomenen i laboratorieexperimenten. Avhandlingen fokuserade på syntetiska alkalihalid-alkalisulfat blandningar som är relevanta vid förbränning av biomassa och för sodapannor vid sulfatmassafabriker. I avhandlingen studerades även växelverkan mellan blyklorid och alkalisalter, som är relevant för avfallsförbränning. Stålmaterialen som undersöktes var kolstål (P235GH) och låg legerat stål (10CrMo9-10) för vilka högtemperaturkorrosionsmekanismerna studerades.

Laboratorieexperiment utfördes med en luftkyld temperaturgradientsond i en het ugn. Luftkylningen resulterade i en temperaturgradient från den heta luften i ugnen till den kallare sonden. I sonden fanns två stålringar övertäckta med syntetiskt beläggningsmaterial. Experiment utfördes även med en flödesreaktor (eng. entrained flow reactor, EFR) där askbeläggningsbildning och åldrande studerades. Beläggningar från både temperaturgradientsonden och EFR framställdes för att få ett tvärsnitt, som sedan analyserades med ett svepelektronmikroskop.

Resultaten visade att askbeläggningarna påverkas av mekanismer både i vätske- och gasfas. I enlighet med tidigare forskningsresultat observerades att vätskefassintring inverkar på askbeläggningarnas densitet och avlägsningsbarhet. Resultaten visade dessutom att vätskefassintring vid en temperaturgradient kan leda till lokal anrikning av föreningar i askbeläggningen. Anrikningen sker då vätskefasen rör på sig i en porös beläggning. Då vätskefasen når en lägre temperatur i beläggningen så stelnar vätskan. Så kallade zonsmälting vid en temperaturgradient påverkade sammansättningen av beläggningarna. På

grund av koncentrationsskillnader i vätskefasen vid temperaturgradienten, sker det diffusion i vätskefasen, vilket resulterar i migration av vissa föreningar i vätskefasen mot varmare temperaturen. Den praktiska innebörden av detta fenomen för askbeläggningar är ännu oklart och det bör studeras vidare.

Resultaten visade att alkalihalider rör sig mot kallare temperaturer i syntetiska askbeläggningar. En rimlig förklaring är att närvaron av temperaturgradienten leder till en koncentrationsgradient för alkalihaliderna i gasfasen. Alkalihalidernas partialtryck är en funktion av temperaturen, och partialtrycket ökar vid stigande temperatur. Diffusionsmekanismen observerades i laboratorieskala och bekräftades med hjälp av matematisk modellering.

Utifrån de erhållna resultaten observerades att $PbCl_2$ rör sig i askbeläggningar i gasfasen och interagerar med alkalisalter. $PbCl_2$ bildade med NaCl en eutektisk smälta, men utan att nya föreningar bildades. $PbCl_2$ reagerade med Na_2SO_4 till karakolit ($Na_3Pb_2(SO_4)_3Cl$) och NaCl. $PbCl_2$ reagerade med både KCl och K_2SO_4 varvid nya K-Pb-Cl föreningar bildades. Dessutom bildades en karakolitliknande förening ($K_3Pb_2(SO_4)_3Cl$) i reaktionen mellan $PbCl_2$ och K_2SO_4. Denna förening har än så länge inte bekräftats att existera enligt den vetenskapliga litteraturen.

Korrosionsmekanismerna med alkaliklorider och -bromider var lika varandra i enlighet med vad som rapporterats i den vetenskapliga litteraturen. Alkalihaliderna reagerade med stålet och bildade metallhalider, som sedan bildade smältor med låg smälttemperatur tillsammans med andra föreningar i beläggningen. Alkalihaliderna ledde till hög korrosionshastighet med de studerade ståltyperna vid 500 °C. Vid lägre temperaturer var korrosionshastigheten låg. Blykloridföreningar ledde till mycket snabb korrosion av kolstål redan vid 400 °C. Ren $PbCl_2$ var mer korrosiv än olika K-Pb-Cl-föreningar.

Avhandlingen visar hur åldrandet av askbeläggningar i en temperaturgradient kan leda till ändringar i askbeläggningarnas förmåga att påskynda högtemperaturkorrosion. Avhandlingen visar även att, askbeläggningarnas densitet påverkas av åldrandet, vilket leder till beläggningar som är svårare att avlägsna från värmeväxlarytor. Avhandlingen studerade systematiskt fenomen som påverkar askbeläggningarnas egenskaper. Åldringsmekanismerna studerades på fundamental nivå för att få en bredare kunskap för mekanismernas detaljer och dess relevans i ångpannors drift och planering.

List of publications

This thesis is based on the work contained in the following papers:

I. D. Lindberg, **J. Niemi**, M. Engblom, P. Yrjas, T. Laurén, M. Hupa, Effect of temperature gradient on composition and morphology of synthetic chlorine-containing biomass boiler deposits, Fuel Processing Technology 141 (2016) 285-298.

II. **J. Niemi**, D. Lindberg, M. Engblom, M. Hupa, Simultaneous melt and vapor induced ash deposit aging mechanisms - Mathematical model and experimental observations, Chemical Engineering Science 173 (2017) 196-207.

III. **J. Niemi**, D. Lindberg, M. Engblom, H.N. Tran, A Fundamental Study on the Change in Composition of Fireside Deposits with Time in Kraft Recovery Boilers, Journal of Science and Technology for Forest Products and Processes, 7 (2) (2018) 45-52.

IV. **J. Niemi,** R. Balint, M. Engblom, J. Lehmusto, D. Lindberg, Temperature-Gradient-Driven Aging Mechanisms in Alkali-Bromide- and Sulfate-Containing Ash Deposits, Energy & Fuels, 33 (7) (2019) 5883-5892.

V. **J. Niemi,** H. Kinnunen, D. Lindberg, S. Enestam, Interactions of $PbCl_2$ with Alkali Salts in Ash Deposits and Effects on Boiler Corrosion, Energy & Fuels, 32 (8) (2018) 8519-8529.

Contribution of the author

Paper I

The measurements were planned by Niemi together with the co-authors. Niemi performed the experimental measurements and analyzed the laboratory results. Engblom did the CFD calculations. Niemi, Lindberg, and Engblom wrote the paper collaboratively.

Paper II

The measurements were planned by Niemi together with the co-authors. Niemi performed the experimental measurements, did the modeling and analyzed the results. Niemi was the main writer of the paper.

Paper III

The measurements were planned by Niemi together with the co-authors. Niemi performed the experimental measurements and analyzed the results. Niemi was the main writer of the paper.

Paper IV

The measurements were planned by Niemi together with the co-authors. Balint performed the experimental measurements. Niemi and Balint analyzed the results together. Lindberg conducted the thermodynamic calculations. Niemi was the main writer of the paper.

Paper V

Corrosion measurements were planned by Niemi and Kinnunen. Niemi performed the experimental part of the laboratory measurements and Kinnunen conducted the analyses of the boiler deposit. Evaluation of the results was performed by Niemi and Kinnunen together with the co-authors. Kinnunen and Niemi focused on corrosion and deposit chemistry respectively. Niemi was the main writer of the paper.

Related publications not included in the thesis

I. **J. Niemi**, D. Lindberg, M. Engblom, T. Laurén, M. Hupa, Alkali chloride transport within superheater deposits due to temperature gradients, 22nd International Conference on Fluidized Bed Conversion, Turku, Finland, 2015, pp. 667-677.

II. **J. Niemi**, D. Lindberg, M. Engblom, T. Laurén, M. Hupa, The effect of temperature gradient on densification of ash deposits containing alkali salts. Nordic Flame Days 2015, Copenhagen, Denmark, in October 2015.

III. **J. Niemi**, D. Lindberg, M. Engblom, M. Hupa, Temperature gradient induced boiler deposit densification and intradeposit alkali chloride enrichment. 26th Impacts of Fuel Quality on Power Production, Prague, Czech Republic, in September, 2016.

IV. M. Engblom, D. Lindberg, **J. Niemi**, M. Hupa, Mathematical modeling of intradeposit alkali chloride enrichment in biofuel boiler superheaters. 26th Impacts of Fuel Quality on Power Production, Prague, Czech Republic, in September, 2016.

V. D. Lindberg, **J. Niemi**, M. Engblom, T. Laurén, P. Yrjas, M. Hupa, Experimental and Modeling Approaches to Simulate Temperature-Gradient Induced Intradeposit Chemical Processes with Implications for Biomass Boiler Corrosion, 23rd International Conference on Fluidized Bed Conversion, Seoul, Korea, in May 2018.

Table of contents

1 INTRODUCTION

World energy consumption increases at a steady pace, while at the same time there is an acute need for a decrease in the utilization of fossil fuels and in the greenhouse gas emissions. The European Union has set key climate goals for 2030 [1]:

- At least 40% cuts in greenhouse gas emissions (from 1990 levels)
- At least 32% share for renewable energy
- At least 32.5% improvement in energy efficiency

Renewable energy includes also combustion of renewable fuels, e.g. biomass. Although heat and power production from waste-firing can be argued to not be renewable, it is still preferable instead of landfilling. Before firing, waste fractions that can be reused or recycled are removed and only the energy fraction is fired to produce heat and power.

Electrical efficiency in biomass and waste-firing is often remarkably lower than e.g. in coal combustion. The reason for the lower efficiency is the lower final steam temperature, which is the key parameter affecting the electrical efficiency. The reason for the lower steam temperature is connected to the composition of the fuel and to the ash composition.

Biomass and waste fractions often include elements that are detrimental to the heat exchanger tubes, because they induce high-temperature corrosion. Such elements include e.g. alkali metals (Na and K) and heavy metals (Pb and Zn) together with halogens (F, Cl, and Br). In addition, higher material temperature of the heat exchanger tubes induces faster corrosion rates. There is a development toward the utilization of increasingly complicated fuels (e.g. waste and process side streams) and fuel combinations, as they are often economically lucrative for heat and power production.

In order to increase the share of renewable fuels utilized in heat and power production and to increase the electrical efficiency of the boilers, it is important to understand how different ash-forming elements behave in boilers. For the elements to affect heat exchanger tubes, they need to come in contact with the material surface. While ash deposition has been studied extensively, ash deposit aging has not seen as much interest. However, initially noncorrosive deposits may evolve, when given enough time, to highly corrosive if some key corrosive elements are enriched on the tube material surface.

1.1 Objectives

The main objective of the work reported in this thesis is to identify and to better understand the fundamental chemical and physical phenomena occurring in steam boiler ash deposits due to steep temperature gradients. The focus is on the phenomena that induce morphological and chemical changes in the ash deposits. Especially molten phase phenomena were studied because molten phases often induce catastrophic corrosion when in contact with the heat exchanger surfaces. In addition, the enrichment of corrosive alkali halides and lead chloride species, as well as their interactions with each other and with the heat exchanger material, were studied.

1.2 Research approach

The research approach is to concentrate on identifying the fundamental mechanisms and therefore this thesis mainly studies simplified synthetic deposits in well-controlled laboratory environments. The deposit materials used in this study were mixtures of alkali chlorides, alkali bromides, alkali sulfates, and lead chloride. The halide salts were chosen due to the prominent role they play in high-temperature corrosion.

The laboratory-scale experiments enable a fundamental approach where the key parameters such as the deposit composition and the temperature profile can be controlled, and their effect on the deposit morphology and chemistry can be assessed. In addition to the static deposits, experiments were conducted using an entrained flow reactor where the deposits were built-up in a fashion closer to a boiler environment. The entrained flow reactor experiments were conducted as a step closer to the realistic application environment in order to confirm that the fundamental mechanisms are present also in more complex systems.

The observed fundamental mechanisms were evaluated relative to available literature and using modeling solutions drawing from the physical prime principles. In addition, thermodynamic modeling and computational fluid dynamics were applied in order to confirm some of the results observed in the laboratory scale studies. The results from the laboratory experiments and modeling were also compared to existing results from boiler deposits.

1.3 Contribution of this work

This work is one of the first ones to conduct well-controlled experiments on the effects of temperature gradients on ash deposits, in conjunction with modeling of the said experiments. The implications regarding deposit aging are significant from the corrosion and deposit removability points of view. The experimental and

modeling results of this work confirm and validate the occurrence of aging mechanisms in ash deposits that have only been hypothesized by other research groups. In addition, this work introduces ash deposit aging mechanisms that have not been considered to occur in ash deposits before. Furthermore, this work adds to the knowledge of high-temperature corrosion mechanisms and on the corrosive nature of different chemical compounds and mixtures present in ash deposits.

2 BACKGROUND

2.1 Steam boiler working principle

The basic working principle of a steam boiler is to apply heat energy to water in order to create steam. The heat is produced by converting chemical energy into heat via a combustion process, where the fuel undergoes an overall exothermic oxidation reaction. In order to produce electrical power, the steam is fed into a steam turbine. The expansion of the high-pressure steam results in rotary motion of the turbine and thus converts the thermal energy of the steam into mechanical work. The steam from the steam turbine can still be exhausted to a condenser in order to improve the efficiency of the process. The mechanical work of the steam turbine is used to generate electrical power via an electrical generator, which is connected to the turbine.

The fuel used in the combustion process can vary greatly. Different fuels contain different amounts of moisture, volatile matter, fixed carbon, and ash-forming matter. The composition of the fuel and e.g. char carbon reactivity affect how the fuel is combusted and which kind of boiler technology is the most suitable. In addition, the amount of individual elements (e.g. C, H, N, O, and S) in the fuel affects its properties. As a rule of thumb, older fuels (coal) contain higher amounts of C and lower amounts of H and O compared to younger fuels (biomass) [2].

The heat energy generated from the combustion is used to heat and boil water and to heat the steam. The heating and boiling of the process water/steam occur with heat exchangers. Heat exchangers are typically metal tubes within the boiler. Inside the tubes there is water/steam flowing, and outside is the combustion atmosphere. Heat exchangers are placed throughout the boiler to maximize the efficiency of the heat exchange. The furnace walls are often lined with heat exchanger tubes (waterwall tubes) in order to maximize the heat transfer. The heat transfer to the waterwall tubes occurs mainly by radiation. Along the flue gas line, there are additional heat exchangers, of which the superheaters are the ones where the hottest steam is located. The heat transfer to the superheaters occurs mainly by convection. The heat from the combustion gases is transferred to the steam, resulting in a cooling of the flue gas as it travels further in the flue gas duct. Down the line, there are still heat exchangers (economizers), to utilize the remaining heat from the flue gas.

In order to maximize the electrical efficiency of the boiler, the final steam temperature, i.e. the temperature of the steam from the superheaters, should be as high as possible [3].

Different boiler technologies are utilized for firing different types of fuels. Boilers firing pulverized fuel mainly use coal as a fuel, but pulverized coal-fired boilers can also be co-fired with biomass or even be fired completely on e.g. torrefied biomass. [4]

In fluidized bed combustion (FBC), the fuel is fed into a particle bed (sand, limestone, etc.). Combustion air is blown into the bed from the bottom, resulting in the fluidization of the bed. The fluidization of the bed results in effective mixing between the combustion air and the fuel, and in rapid heat transfer. In addition, the combustion temperature is often lower than in boilers firing pulverized fuels, resulting in lower NOx emissions. FBC technologies can be divided into bubbling fluidized bed (BFB) and circulating fluidized bed (CFB) boilers, depending on the fluidization rate of the bed. In addition, FBC can either be atmospheric or pressurized. FBC can, in general, be utilized for a wide range of fuels (from coal to waste), and little fuel preparation is needed compared to pulverized fuel boilers.

In grate-fired boilers, the fuel is introduced into the furnace on a grate. Combustion air is introduced through the grate, resulting in the combustion of the fuel. The grate itself can be stationary (pile burner) or moving. Grate-fired boilers can fire a large variety of different fuels, including biomass and waste-derived fuels. Grate-fired boilers are typically used for low-grade fuels, e.g. municipal solid waste or straw. Compared to FBC, grate-fired boilers have in general lower thermal efficiency but are simpler in design, i.e. less expensive.

The black liquor recovery boiler is a special boiler, which is an essential part of a pulp mill [5]. The recovery boiler has a dual purpose as it is used as a chemical reactor to recover pulping chemicals and to produce heat and power, by combusting black liquor. Black liquor is generated when wood chips are cooked in an alkaline solution containing Na_2S and NaOH (white liquor). As a result of the cooking, cellulose is separated from the wood chips and as a byproduct, weak black liquor is generated. In addition to water, the weak black liquor consists mainly of lignin and hemicellulose, which have been separated from the wood in the pulping process, and spent pulping chemicals, i.e. Na_2SO_4, $Na_2S_2O_3$ and Na_2CO_3 [6]. In addition, the black liquor contains inorganics from the wood. The weak black liquor is passed through a series of evaporators in order to decrease the water content so that the resulting black liquor can be combusted.

The black liquor is sprayed into the recovery boiler. The lower furnace of a recovery boiler is operated at reducing conditions so that Na_2SO_4 from the black liquor is reduced to Na_2S. The inorganic process components (Na_2S and Na_2CO_3) are collected at the bottom of the recovery boiler in a molten salt mixture called the smelt. The smelt bed at the bottom furnace flows out into a dissolving tank where

the smelt is dissolved in weak white liquor from the lime mud washing process, resulting in green liquor. The green liquor is further processed in a causticizing plant where the Na_2CO_3 reacts into NaOH, resulting in white liquor, which can again be used in the pulping process [5].

High amount of inorganic material is characteristic for a black liquor recovery boiler. The organics-to-inorganics ratio in black liquor is close to 1:1 [7]. Due to the high amount of ash-forming matter, deposit build-up is fast and soot-blowing is necessary to keep the flue gas paths open. Ash deposits in black liquor recovery boilers often consist mainly of Na_2SO_4 and Na_2CO_3, with a minor amount of NaCl, Na_2S and their potassium (K) counterparts [8]. A significant portion of the work reported in this thesis was done with synthetic alkali salt mixtures relevant for black liquor recovery boilers.

2.2 Ash-forming matter in fuel

Different fuels contain different amounts of ash-forming matter and the ash composition differs greatly between different fuel fractions. For example, the ash content in fuel fractions can vary from low (<1 wt-%), in pristine wood, to high (20 wt-%), in e.g. some coal grades, waste wood and rice waste [9]. As for the composition, e.g. coal ash often consists mainly of Si, Al, and Fe, while ash from wood-derived fuels is mainly composed of Ca, K, Si and Mg [9, 10].

The ash-forming matter can be present in the fuel as [11]:

1) Organically bound matter, which includes metal ions (e.g. K, Na, Mn, Ca, Mg, Fe, and Al), bound to anionic organic groups. In addition, S, P, and Cl are common organically bound ash-forming elements.

2) Dissolved salts, which include alkali and earth alkali metal ions and small dissolved anions (e.g. Cl^-, SO_4^{2-} and phosphates).

3) Included minerals, which have naturally precipitated in the biomass (e.g. silica, calcium oxalate, iron oxides, and iron hydroxides).

4) Foreign matter/excluded minerals, which consist mainly of soil minerals (e.g. sand and clay mineral) in biomass. In waste-derived fuels, the foreign matter can be e.g. metallic aluminum in contrast to e.g. organically bound ash-forming matter in organic waste material.

Depending on the ash composition and the way the elements are associated in the fuel, the ash-forming elements are released into the furnace differently. The combustion process starts with the drying of the fuel as the moisture exits the fuel as H_2O (g). The drying is followed by pyrolysis where the volatile organic matter

volatilizes, and the fuel is devolatilized. The volatile organic species are subsequently combusted outside the fuel particle, when they come in contact with oxygen and other oxidizing agents (e.g. H_2O, CO_2), resulting in a visible flame. During the devolatilization, some reactive ash-forming elements are also released into the gas phase. After the devolatilization stage, the fuel particle experiences char burning, where the fixed carbon reacts with oxidizing agents at the surface of the fuel particle. What is left after the char burning is residual ash.

The ash formed in a boiler can be divided into bottom ash and fly ash. Bottom ash, as the name states, is left at the bottom of the boiler, while fly ash is entrained into the flue gas flow. The ratio between the bottom ash and the fly ash depends on the boiler design and the size of the ash particles. Inorganic compounds with high volatility vaporize and they can be present in the boiler in the gas phase. The gaseous compounds can subsequently nucleate homogeneously and form aerosols, contributing to the fly ash. Compounds with low volatility (e.g. silicates) are present in liquid or solid phase and are either included in the bottom ash or are entrained into the flue gas.

The ash composition varies greatly between different fuels. Coal ash is often rich in Si, Al, and Fe. In addition, a high amount of Ca and S can be present in coal ash [9]. Coal ash is usually lean in Cl, but there are coal grades that include high Cl and high alkali metal contents [12].

Ash from wood or woody biomass often consists mainly of Ca, K, Si, and Mg, with a smaller amount of P, Al, Fe, S, Na and Ti [9, 10]. Wood and woody biomass also contain some Cl but the amount is often low. Herbaceous and agricultural biomass can contain high amounts of Cl, S, and P, which makes them more problematic from the ash deposit point of view [9]. Some selected biomass fractions have even been observed to include relatively high amounts of Br [13].

Different waste fractions (e.g. Recovered waste wood (RWW), Municipal solid waste (MSW), Solid recovered fuel (SRF) and Refuse-derived fuel (RDF)) have different compositions and the fractions themselves can be highly heterogeneous. Waste fuels can include high amounts of halogens [14, 15] and high amounts of Zn and Pb have been shown to be found in waste fuels [16, 17]. In addition, significant amounts of Si, Fe Ca, Al, Na, K, C, Mg, and S have been observed in waste fuel bottom and fly ash [18].

For the purposes of a detailed study on the effects of temperature gradients in ash deposits, a handful of elements were chosen to be studied in the laboratory experiments. The elements considered in the experimental part of this thesis, their

occurrence, and sources in different fuel fractions (biomass, waste and black liquor), are considered in more detail below:

Chlorine

Cl is one of the micronutrients needed for plant growth. The concentration of Cl can vary from a relatively low concentration in wood or woody biomass [19] to a high concentration in agricultural residues, e.g. wheat straw [20, 21].

Waste fractions can include high amounts of Cl. In municipal solid waste, chlorinated non-packaging plastics include significant amounts of Cl. Another significant source of Cl is kitchen waste [22]. Waste wood fractions have been shown to include high amounts of Cl. It can originate from different wood treatments, e.g. paint and binders, but some of it also originates from the wood itself [23].

Cl is also often present in the black liquor recovery process as a non-process element and can be found in recovery boilers as an ash-forming element. Cl is introduced to the recovery process from the wood. Mills with closed-cycle may experience Cl enrichment in their liquor. In addition, mills located in coastal regions compared to inland mills experience higher Cl concentrations in the recovery cycle, due to the Cl present in the seawater [24].

Bromine

Br is present in some selected biomasses. Naturally occurring Br originates mainly from the seawater and therefore marine biomass can include high concentrations of Br. Coastal peat has also been reported to include notable concentrations of Br [13].

Waste-derived fuels can include high amounts of Br, as it is used for example in flame-retardants, which are found in municipal solid waste and solid recovered fuel. Brominated flame-retardants are used to treat plastics, which can, therefore, include several mass-percent of Br. In addition, brominated biocides are an important source of Br in waste-derived fuels. Biocides can even be present in biomass fuels [14].

Sulfur

S is present in all biomass due to it being an essential element for plant growth. S is present in biomass as inorganic sulfate anions as well as organically bound S. In addition, S can be present as a waste processing chemical (e.g. iron or aluminum sulfates) in some selected waste fractions [11].

In the black liquor recovery process, S is one of the main process elements, which results in an abundance of S in black liquor recovery boiler deposits, either as sulfate or as sulfide [8].

Lead

Pb is often present in waste-derived fuels. It can originate from a number of sources, either as metallic Pb or as Pb compound. Metallic Pb can originate e.g. from batteries, solder or electrical wiring. Pb compounds are included in crystal glass, PVC stabilizers and in different pigments and paints. Pb in municipal solid waste originates mainly from small lead batteries used in small electrical appliances, while the contribution of PVC, paints, and pigments to the Pb amount is rather small due to the low concentration of Pb in them [25]. In recovered waste wood, Pb originates mainly from the surface treatment of the wood, e.g. from pigments, dryers and biocides [26].

Sodium

Na is not a nutrient for plants, but is still present in biomass fuels, more so in fuels originating from coastal regions, where the Na originates from the seawater [27]. Na can also be included in the fuel as an exclusion, i.e. from the soil in the form of Na-silicates [11]. Waste fractions include significant amounts of Na. Recovered waste wood can have elevated Na content compared to stem wood, e.g. due to Na being present in paints [28].

Na is an important process element in the Kraft pulping process, where it is included in white liquor as Na_2S and NaOH. After pulping, the black liquor includes Na_2SO_4 and Na_2CO_3. In the recovery boiler, the Na_2SO_4 is reduced to Na_2S in order to recover the pulping chemicals. However, some of the inorganics are entrained or vaporized in the flue gas and they can form ash deposits. The ash deposits in recovery boilers consist mainly of Na compounds [8].

Potassium

K is a nutrient for plants and therefore it is abundantly present in biomass fuels. Straws have been shown to include high concentrations of K [2]. Waste fractions can also include high concentrations of K, originating e.g. from the biomass included in the waste fraction in question.

In the black liquor recovery process, K originates from the wood raw material. In a closed cycle, K can enrich in the recovery cycle and in the recovery boiler deposits. The concentration of K is higher in hardwood mills compared to softwood mills [24].

2.3 Heat exchanger deposits

Ash in the boiler can deposit on the heat exchanger surfaces and form heat exchanger deposits. Heat exchanger deposits are heterogeneous in nature, both in composition and in morphology. The heterogeneous nature is due to the combined effects of the deposit formation mechanisms and the deposit aging mechanisms.

2.3.1 Deposit formation mechanisms

Heat exchanger surfaces in boilers experience fouling. The ash-forming elements present in a boiler build-up on the heat exchanger surfaces. Heat exchanger fouling has been studied extensively using deposit probes and modeling. [29, 30] The main fouling mechanisms have been recognized to be direct condensation, thermophoresis, and inertial impaction, including eddy impaction [30].

Direct condensation of ash-forming matter on the heat exchanger surface occurs when the concentration of gaseous inorganic species is high. When the hot flue gas comes in contact with a colder heat exchanger surface and cools down, a supersaturation occurs in the gas phase resulting in heterogeneous direct condensation of inorganic species. The condensation occurs directly from the gas phase on to the heat exchanger surface. Condensation behavior of alkali halides has been observed to be affected by the temperature of the condensation surface [31] as well as by the temperature gradient [32].

Thermophoresis takes place when gaseous ash-forming elements nucleate homogeneously in the flue gas, due to supersaturation. When the formed aerosols are exposed to a temperature gradient near a heat exchanger, they experience a driving force towards the heat exchanger surface. The driving force occurs due to the temperature gradient. The flue gas molecules on the hotter side of the small particles move faster and collide more with the particles than the flue gas molecules on the colder side. The difference in the kinetic energy of flue gas molecules in different temperatures results in a force that pushes the small particles towards the colder temperature, i.e. to the heat exchanger surface. The initial deposit formation is often a result of the direct condensation and thermophoresis mechanisms.

Inertial impaction occurs when solid or liquid fly ash particles impact into heat exchanger surfaces. Depending on the flow characteristics of the flue gas, the ash particles that are entrained into it can either follow the flue gas flow and go around heat exchangers or deviate from the flue gas flow and impact into heat exchangers. Larger fly ash particles usually impact on the wind-side of the heat exchanger tubes as they deviate from the flue gas path due to their inertia.

Small fly ash particles that initially follow the flue gas stream around the heat exchanger tube can be entrained in turbulent eddies, formed near the heat exchanger tube. The eddies accelerate the particles, which then can exit the eddies, possibly impacting with the lee-side of the heat exchanger [30].

The particles that impact on the heat exchanger surface can either stick to it or bounce off. The sticking propensity depends on a number of factors, of which the amount of liquid phase in the ash particle, the amount of liquid phase in the deposits, and the particle speed are among the most important. Generally, the more liquid present in either the deposit or the particle, the more likely the particle is to stick to the deposit surface. In black liquor recovery boilers, the melt fraction of 15 wt-% has been observed to be the amount of melt, which is required for the particle to be sticky [33]. The effect of the melt fraction has been shown to be significant also in biomass-fired systems [34]. The contribution of inertial impaction to deposit build-up is high in the convective pass. The first row of superheaters on the flue gas path is often most affected by inertial impaction. Because of deposit formation on the superheaters, the amount of large fly ash particles decreases down the flue gas path, which results in less impaction with the heat exchangers. In addition, inertial impaction usually starts to affect deposit build-up more after an initial sticky deposit layer has been formed by condensation and/or thermophoresis [30].

Deposits can also grow due to chemical reactions. For example, alkali halides can react with SO_2 from the flue gas, and form alkali sulfates [35].

2.3.2 Deposit aging mechanisms

The deposit formation mechanisms affect the structure and composition of the deposits but also the aging in the boiler environment affects the deposits. However, deposit aging is not as widely covered subject as the deposit formation mechanisms. To separate deposit aging mechanisms from the deposit formation mechanisms is challenging in boiler scale studies as the formation and aging occur simultaneously. In laboratory-scale, the dynamic boiler conditions are challenging to simulate. However, a number of studies have made efforts to shed light on the deposit aging mechanisms and their role on the boiler deposit structure and chemistry.

Sintering is one of the main mechanisms affecting the deposit structure when the deposit ages. Sintering is a process in which usually fine-grained particles or powder are compacted. Sintering is spontaneous densification of fine-grained materials usually at temperatures lower than the melting point. Sintering occurs when either heat or pressure is applied to solid fine-grained material, without

melting it completely to a liquid phase. Sintering can be roughly divided into three different categories depending on the mechanism it occurs by. (1) Solid phase sintering [36] occurs with particles that are in contact with each other. The atoms or ions in the particles diffuse via solid-state diffusion to the contact point of the particles resulting in the two distinct particles growing into one larger particle. (2) Liquid state (phase) sintering [37] occurs with a liquid phase present. The liquid phase functions as a glue between particles and binds them together. Liquid phase sintering occurs quickly due to the fast movement of atoms and ions in the liquid phase. (3) Sintering can also occur by vaporization and condensation of species. The volatile species vaporize from the particles and condense in the neck region increasing the connectivity of the two particles.

Sintering can affect deposit density but not all sintering results in deposit densification. When sintering results in pore elimination within the deposit, it results in deposit densification. Sometimes sintering only results in rearrangement of the atoms. The rearrangement of the atoms results in changes in the pore shape, size and amount, but the overall porosity remains the same i.e. the deposit density remains the same. However, even sintering without densification affects the deposit properties, such as deposit removability and thermal conductivity.

Sintering has been shown to occur with different deposit materials and to be highly dependent on the deposit composition and the sintering temperature [38-41]. Sintering of deposits has been observed to affect the removability of the deposits [42, 43]. Sintering in isothermal conditions leads to homogenization of material as the atoms and ions are rearranged more evenly. However, temperature gradients induce potential differences, which affect the diffusion mechanisms. Sintering in temperature gradients via liquid phase sintering has been shown to lead in the enrichment of components in certain temperature regions [43, 44] and is one of the focal points of this thesis.

Robinson et al. [45] showed that the sintering of ash deposits in a temperature gradient leads to an increase in the thermal conductivity of the deposit material. Their results show that during the initial sintering of the deposits there is a significant increase in the thermal conductivity, while additional sintering has little effect on the thermal conductivity.

In addition to sintering, different flue gas species can penetrate the deposit and condense or react with the existing deposit [46]. Although it borders to deposit build-up – chemical reaction is counted as one of the deposit build-up mechanisms – it can also be considered a deposit aging mechanism. Flue gas often includes SO_2, which can react with alkali chlorides and form alkali sulfates [35]. Corrosion reactions are also feasible to affect the deposit aging. Formation of metal chlorides

or other corrosion products that have the ability to function as a fluxing agent in the deposit, i.e. decreasing the temperature where the melt is formed, can affect the deposit structure and composition [47, 48].

When deposits grow large enough and/or the oxide layer of the heat exchanger material flakes off, there is a chance for deposit shedding. The deposit can shed as a whole or just partly, thus deposit shedding also contributes to the deposit structure [49].

Temperature gradients induce a number of phenomena that could be of interest for ash deposit aging. Temperature gradients have been observed to induce pore motion in monolithic crystals of KCl and NaCl [50-55]. The pore motion occurs due to the vaporization-condensation mechanism of the alkali chlorides, which results in material transport towards the colder temperature and pore motion towards the hotter temperature.

Temperature gradient zone melting [56-58] is a phenomenon, which occurs in eutectic melt systems. The phenomenon occurs due to a temperature gradient over the material, which has a liquid composition depending on the temperature. The temperature gradient induces concentration differences within the liquid phase, resulting in species diffusion. Prior to this work, temperature gradient zone melting has not been reported or considered to affect boiler deposit aging. However, e.g. species migration observed by Lagerbom et al. [48] is potentially due to the temperature gradient zone melting phenomenon.

2.3.3 Deposit studies

Ash deposits from straw-fired boilers have been studied by several authors [47, 59, 60]. Ash deposits collected with a probe have been shown to form layered structures if the probe was cooled, while deposits collected with an uncooled probe resulted in more homogeneous deposits [47]. With the cooled probe, most of the collected deposits consisted of KCl, while with the uncooled probe close to no KCl was observed, which shows that the main mechanism for KCl deposition is either by condensation or by thermophoresis.

In the cooled probe experiments and in the mature boiler deposits, the innermost part of the deposits consisted mainly of KCl [47, 59, 60]. The temperature of the steel surface has been observed to affect the morphology of the innermost layer. The cooler steel surface has been shown to result in more clear crystal structures of KCl, while a hotter steel surface has been shown to result in a denser KCl layer [47]. The dense KCl layer with the hotter steel surface was hypothesized by the authors to be due to a melt formation with KCl and the corrosion products.

Mature superheater deposits collected from straw-fired boilers have been shown to be more heterogeneous compared to probe deposits [59, 60], which indicates the importance of deposit aging mechanisms. While probe deposits only consisted of two different layers (the oxide layer and a dense KCl layer with iron oxide inclusions), the mature superheater deposits have been observed to have six different layers. It is noted by Hansen et al. [60] that the innermost K_2SO_4 layer in the mature superheater deposits is likely formed from condensed KCl, which has undergone a sulfation reaction. The middle part of the mature superheater deposits is similar to the probe deposit, i.e. consisting mainly of angular KCl crystals. However, Jensen et al. [59] noted that the KCl rich layer was markedly thicker in the mature boiler deposits than in the probe deposits. The authors hypothesized that the thick KCl rich layer was due to KCl penetration through the deposit and subsequent condensation in the colder temperature range, resulting in the thicker KCl rich layer and denser deposit structure. The work presented in this thesis also suggests KCl is likely to enrich in colder temperature within deposits due to intradeposit migration.

Wu et al. [61] did similar observations from probe measurements in a boiler firing straw/grass seed chaff. They suggested that the KCl on the steel surface has most likely deposited directly from the flue gas and that there was a possibility for an intradeposit transport of KCl from the outer deposit surface towards the probe surface, with longer exposure times.

The outer parts of the mature superheater deposits collected by Jensen et al. [59] and Hansen et al. [60] were similar. The first layer consisted of a dense layer of KCl, which was concluded by the authors to have experienced temperatures above the melting temperature of KCl (771 °C [62]). Towards the flue gas, it was followed by a KCl layer with inclusions of fly ash particles. The outermost porous layer consisted of captured fly ash particles. The deposit probe measurements in a straw/grass seed chaff firing boiler by Wu et al. [61] showed deposits, which contained KCl rich regions, K, S, Ca and O, as well as an increasing amount of Si-rich particles closer to the flue gas, similar to Jensen et al. [59] and Hansen et al. [60].

Other biomass-fired boilers have been shown to experience similar deposits. Lapuerta et al. [27] collected superheater deposits from a boiler firing a mixture of exhausted olive cake and other biomass (wood, exhausted grape cake, almond shells and others). The superheater deposits were observed to be dense close to the steel, while the outer deposit layer composed of larger particles and had larger pores. The authors reported pure KCl crystals present in the inner deposit layers and in the outer deposit. In addition, the outer surfaces of the deposits had

experienced melting in the boiler, resulting in hard deposits. The deposits situated in the hotter regions, with hotter flue gas and steam temperatures, were observed to be harder. The amorphous regions in the deposits were reported to contain high amounts of Na, causing the melting and agglomeration of the deposits.

Broström et al. [63] collected probe deposits from a CFB boiler firing bark, wood, and chlorine-containing reject from a cardboard recycling facility. The deposits were collected after a four-week exposure time, with steel temperature at 400-555 °C and the flue gas temperature at ~800 °C. They collected deposits from different sides of the boiler, one of which was operated with an ammonium sulfate addition, and the other one without the addition. The collected deposits contained mainly Ca, K, S, and Cl, while O was not analyzed. The probe deposit collected from the side without the ammonium sulfate addition had a higher Cl content. In addition, the inner part of the deposit was enriched in Cl. The ammonium sulfate addition resulted in sulfation of alkali chlorides in the flue gas and in lower amounts of alkali chlorides in the deposits, on the side of the boiler with the additive.

The enrichment of alkali chlorides on the cool steel surface has also been observed in black liquor recovery boilers. Reeve et al. [24] conducted probe measurements in a recovery boiler. Their results showed enrichment of K and Cl in the inner part of the deposits. The K and Cl concentrations were the lowest in the middle of the deposits and then increased slightly in the outermost region. Costa and Paoliello [64] collected superheater deposits from a recovery boiler. They reported significant enrichment of K and Cl at the steel surface compared to the outer deposit. In addition, they reported significant corrosion of the superheater tube, which according to them is due to molten salt corrosion caused by the enrichment of K and Cl. They concluded that the enrichment was likely due to a combined effect of intradeposit gas phase migration of KCl and direct deposition of fume from the flue gas. In addition, they noted that the formation of molten phases has led to liquid phase movement in the deposits.

Waste-fired boilers have also shown similar enrichment of alkali chlorides and other volatile species on the steel surface. Persson et al. [65] conducted corrosion probe experiments in a boiler firing municipal solid waste or a mixture of municipal solid waste and PVC. Their sampling time was 10 days, with a probe temperature at 320-460 °C and flue gas temperature at 470 °C. They reported deposits composed mainly of alkali sulfates, with Cl enrichment at the steel/oxide surface and indications of $FeCl_2$ formation at the steel-oxide layer interface.

Enestam et al. [17] reported compositions of collected heat exchanger deposits from a boiler firing recovered waste wood. A deposit collected from the furnace wall before the secondary air supply was shown to consist mainly of NaCl and KCl,

with some Pb present. The authors hypothesized that the Pb species had initially deposited as either metallic Pb or as PbS, and subsequently reacted with the alkali chlorides in the deposit, to form K-Pb-Cl and Pb-Cl species. Another deposit was collected from the primary superheater of the boiler, which consisted mainly of K, S, and O, with an area enriched in Pb and Cl at the steel surface.

Kinnunen et al. [66] conducted both short-term (2h) and long-term (5 months) probe measurements in a boiler firing recovered waste wood. The authors reported only small differences between the short-term and long-term results, indicating only minor aging effects in the deposits. The long-term results from the windward side of the probe showed multilayered deposits, where the inner part consisted of corrosion products, alkali metals, Pb, and Cl, similar to the mature deposits by Enestam et al. [17]. With a hot flue gas (800 °C), the outer part of the windward side deposit consisted mainly of Ca, Si, Cl, Na, K, Fe, and O and had a porous morphology. With the colder flue gas (490 °C), the outer part of the windward side deposit consisted of Ca, S, Cl, Na, K, Pb and O, and the morphology was observed dense. The leeward side deposits were thinner than the windward side deposits but also contained corrosive K-Na-Pb-Cl mixtures, indicating that the deposition mechanism is either condensation or thermophoresis. Hedman et al. [67] also reported $PbCl_2$ and KPb_2Cl_5 compounds on the steel surface of a cooled deposit probe sampled from a waste wood firing boiler.

In addition to Cl-species, also Br has been reported to enrich in heat exchanger deposits [68]. In a study by Vainikka et al. [69], several mass-percent of Br was observed locally in waterwall deposits, while the fuel fed into the boiler contained only tens of mg kg^{-1} of Br.

The reported deposits from probe measurements and from heat exchangers are similar in many respects. Both show enrichment of volatile species on the steel surface, e.g. alkali halides and heavy metal halides. In addition, the outer parts of the deposits have a composition closer to the bulk composition of the fly ash. However, the results also suggest that there are differences between probe deposits and mature heat exchanger deposits, e.g. in straw-fired boilers, the KCl enrichment close to the steel surface in mature deposits is more pronounced compared to probe deposits. In addition, the mature deposits are more heterogeneous. The differences indicate that the deposit aging mechanisms play a vital role in the deposit chemistry and morphology, an issue that was studied in this work.

2.3.4 Synthetic deposits studied in this work

Typical carry-over deposits in black liquor recovery boilers contain high amounts of Na_2CO_3 (~50 wt-%) and Na_2SO_4 (~45 wt-%), the rest being NaCl (~2 wt-%), K-salts (~2.5 wt-%) and other components. Fume deposits in the upper and lower furnace are composed of the same elements but the concentrations differ. Fume deposits usually contain less Na_2CO_3 and more NaCl and K-salts [8]. The NaCl-Na_2SO_4 and the K-Na-Cl-SO_4 systems were chosen to be studied due to their relevance to the black liquor recovery boilers.

In the present thesis, the KCl-K_2SO_4 system was studied due to its relevance to biomass combustion. Especially fast-growing crops, e.g. wheat straw, contain significant amounts of K, Cl and S. Ash deposits collected from straw-fired boilers have been shown to compose for a large part of KCl and K_2SO_4 [20, 21]. In addition, KCl has been observed to enrich at the heat exchanger tube surfaces in straw-fired boilers [47, 59, 60]. The KCl-K_2SO_4 and the K-Na-Cl-SO_4 systems were chosen to be studied due to their relevance to the combustion of annual biomass and waste.

Local enrichment of species can drastically alter the melting properties and the corrosive nature of ash deposits. The NaCl-Na_2SO_4-Na_2CO_3 and KCl-K_2SO_4-K_2CO_3 systems have minimum melting temperatures of 612 °C and 628 °C respectively. However, e.g. the K-Na-Cl-SO_4 system has a minimum melting temperature of 517 °C, which is significantly lower than either of the minimum melting temperatures of the single cation systems [70]. For example in black liquor recovery boilers, K enrichment at the heat exchanger tube surface can lead to a decrease in the first melting temperature, possibly resulting in a molten phase in direct contact with the heat exchanger material. Such behavior has been reported in the literature [64]. The KCl enrichment and its effect on the first melting temperature locally within deposits have been studied by Engblom et al. [71]. The modeling results showed that the migration of KCl to the tube surface has the potential to lower the first melting temperature of deposits with ~10 °C in superheater deposits in black liquor recovery boilers.

In this thesis, the NaBr-Na_2SO_4 and KBr-K_2SO_4 systems were studied due to their relevance for waste-firing and for some selected biomass fuels. The enrichment of Br-species in boiler deposits [69, 72] also supported the decision in studying the systems more closely. In addition, alkali bromides were studied due to their similar molecular structure, melting characteristics and chemistry with alkali chlorides. The phenomena, which were observed initially with the alkali chloride-alkali sulfate systems were confirmed to also occur with alkali bromide-alkali sulfate systems. This indicates that the phenomena are general in nature and also applicable to other similar salt systems.

The $PbCl_2$ together with alkali salts and SiO_2 was studied due to the relevance of lead chloride species to waste-firing boilers. SiO_2 does not interact with $PbCl_2$ and the system was mainly used in order to see if there is a gas phase migration effect occurring with $PbCl_2$. The $PbCl_2$-alkali salt mixtures were chosen because Pb, K, Na, Cl, and S have all been found in heat exchanger deposits in waste-fired boilers [17, 66]. The K-salts have relevance especially with waste wood combustion, where an abundance of K is present. In addition, $PbCl_2$ together with K-salts has been shown to result in enrichment of Pb-containing species in specific temperature regions, illustrating the relevance of the temperature gradient [44].

The current study concentrates mainly on binary salt systems due to their relatively simple behavior compared to ternary or higher-order systems. With binary systems, the characteristic melting properties and phase compositions remain relatively simple, which makes the interpretation of the results possible. In addition, the gas phase chemistry remains simple, while there is no interaction with additional components and/or phases that could affect the activity of the volatile species.

2.4 High-temperature corrosion of heat exchangers

High-temperature corrosion is one of the key reasons limiting the steam temperature in boilers. The corrosion kinetics increase as a function of temperature, both due to the fact that chemical kinetics occur faster in higher temperatures and due to the increased amount of molten phase in contact with the steel surface.

High-temperature corrosion in boilers is affected by the composition of the deposit material in contact with the heat exchanger material. The final steam temperature typically decreases in boilers combusting from coal to biomass to waste. The final steam temperature is connected to the ash composition of the fuel. The alkali halides in biomass and the heavy metal halides in the waste-derived fuels tend to induce high-temperature corrosion. In order to manage the corrosion of the heat exchanger tubes, the final steam temperature is kept lower in boilers combusting fuels containing corrosive components.

Alkali halide induced corrosion is considered one of the main contributors to high-temperature corrosion in boiler environments. The focus has been on alkali chlorides but even alkali bromides and alkali fluorides have seen some research interest [73-77]. The detailed corrosion mechanism induced by alkali halides remains under debate.

Grabke et al. [78] proposed a mechanism of active oxidation. In active oxidation, HCl reacts with oxygen at the oxide layer, forming Cl_2 gas and water. They also

proposed that Cl_2 can form from the reaction of NaCl and metal oxides resulting in Cl_2 and sodium-metal-oxide. The Cl_2 subsequently reacts with metallic Fe, resulting in $FeCl_2$. The resulting $FeCl_2$ has a high vapor pressure and it can diffuse through the oxide scale in the gas phase. In higher O_2 partial pressure, the $FeCl_2$ will oxidize and result in iron oxide and Cl_2, which is again available to react with metallic Fe.

Folkeson et al. [79] proposed an alternative mechanism for high-temperature Cl-induced corrosion. They proposed a mechanism where KCl disassociates at the oxide layer in the presence of O_2 and H_2O and forms KOH and Cl^-. Simultaneously, the metallic Fe oxidizes at the metal surface, resulting in Fe^{2+} ions. The Cl^- ions diffuse across the oxide layer, react with the Fe^{2+} and form $FeCl_2$ in the grain boundaries of the steel.

The formation of $FeCl_x$ [65, 66, 78-81] and $FeBr_x$ [75, 76] have been reported by several studies. The formation of metal halides at the steel surface can induce faster corrosion rates because they have the potential to lower the melting temperature of the deposit material in contact with the steel [82]. The formation of a molten phase at the steel surface will increase the corrosion rate as has been shown by several studies [64, 66, 82-85].

The choice of steel material affects the corrosion rate. Cr is generally used in heat exchanger alloys due to its ability to form a dense protective Cr_2O_3 layer. The Cr_2O_3 layer provides protection against corrosion, but the layer can deteriorate rapidly due to reactions with the elements in the ash deposits [86].

$PbCl_2$ induced corrosion has been studied in several papers. Talus et al. [87] showed that by increasing the Pb amount in fuel, the corrosion rate of low-alloyed steel significantly increased. The corrosion was concluded to be due to $PbCl_2$ and the formation of a Pb-K-Cl melt. Similar indications have been observed by others [44, 66, 81, 85]. However, the detailed formation mechanism of Pb–K–Cl species in boiler environments is still unknown.

A number of studies have been conducted in isothermal conditions to evaluate which elements are corrosive, how different steel types corrode and what are the corrosion mechanisms occurring at high temperatures. Although some studies have considered the effects of a temperature gradient to the corrosion of heat exchangers, the studies are still a few in number. Brossard et al. [3, 88] reported an increase in the corrosion rate of steel with steeper temperature gradients. Liu et al. [89] reported similar behavior in their laboratory-scale temperature gradient set-up. Kawahara [46] showed that by cycling the temperature of the steel material and the surrounding flue gas, the corrosion rate increased. The study showed that the

temperature cycling deteriorates the protective oxide scale, making it more vulnerable for corrosion attacks. In addition, there were indications that the temperature gradient induces penetration of corrosive species to the steel surface. Covino et al. [90] studied the effect of temperature gradients on the corrosion of metallic cobalt and carbon steel. They reported that temperature gradient induced diffusion effects took place within the oxide layer.

3 EXPERIMENTAL

Ash deposits were exposed to temperature gradients in a tube furnace and in an entrained flow reactor (EFR). The aged ash deposits were characterized using scanning electron microscopy (SEM) and energy-dispersive X-ray spectroscopy (EDX). In addition, the melting behavior of the deposit material was characterized using differential scanning calorimetry/thermogravimetric analysis (DSC/TGA) and thermodynamic modeling. Thermodynamic modeling was also applied to estimate partial pressures of volatile species within the deposits and mathematical modeling was applied to estimate intradeposit alkali halide-migration rates.

3.1 Laboratory methods

3.1.1 Ash deposit material

The deposits studied in this thesis were synthetic ash deposits, composed of pre-mixed salt systems. The salts systems are summarized in Table 1.

The synthetic ashes were pre-treated, to achieve homogeneity, in a way that is consistent with a procedure used in isothermal corrosion studies [83]. The salt components were mixed together, melted together, quenched, crushed, and sieved to a desired particle size fraction. The melting occurred at a temperature above the liquidus temperature of the mixture for ~20 min. The particle size fractions were 53-250 μm for the temperature gradient furnace experiments and 90-300 μm for the entrained flow reactor experiments.

Table 1. The studied deposit compositions, their calculated and measured (in parenthesis) characteristic melting temperatures (where applicable), and the atmospheres during experiments in the temperature gradient furnace and in the entrained flow reactor.

wt-%						Temperature		Experiment atmosphere	
NaCl	NaBr	Na_2SO_4	KCl	KBr	K_2SO_4	Solidus	Liquidus	Temperature gradient furnace	Entrained flow reactor
32		68				626 (627)	626 (627)	Air	
6.4		93.6				626 (624)	817 (n.a.)	Air	Natural gas flame
16.0		84.0				626 (625)	736 (737)	Air	
25.6		74.4				626 (627)	667 (651)	Air	
86.4		13.6				626 (625)	780 (778)	Air	
			55.5		45.5	690 (685)	690 (685)	Air	
			11.1		88.9	690 (681)	969 (n.a.)	Air	Natural gas flame
			20.2		79.8	690 (681)	900 (n.a.)	Air	
			38.6		61.4	690 (681)	782 (n.a.)	Air	
			91.1		8.9	690 (681)	758 (761)	Air	
6.4		**93.6**	11.1		88.9				Natural gas flame
6.4		93.6	**11.1**		**88.9**				Natural gas flame
	31.5	68.5				622 (617)	719 (n.a.)	Air	
				40.6	59.4	670 (668)	845 (n.a.)	Air	
100								Air + $PbCl_2$ (g)	
		100						Air + $PbCl_2$ (g)	
			100					Air + $PbCl_2$ (g)	
					100			Air + $PbCl_2$ (g)	
50			50			657 (n.a.)	683 (n.a.)	Air + $PbCl_2$ (g)	

3.1.2 Temperature gradient furnace

The main experimental equipment used in this study (Papers I, II, IV, V) is a laboratory-scale air-cooled probe, shown in Fig. 1. The probe consists of three concentric tubes. The cooling air is introduced through the innermost tube. The cooling air is released into the space between the innermost and the middle tubes where it cools down the middle tube.

The middle tube houses two interchangeable steel rings on top of which the deposit samples were applied. The steel sample rings each house a thermocouple, one of which is used to control the airflow into the probe and thus the temperature of the probe and the other is used to measure and record the temperature during experiments.

The outermost protective tube functions as thermal insulation, decreasing the need for the cooling air. One additional thermocouple was placed above the deposits to measure the temperature of the furnace air during the exposure.

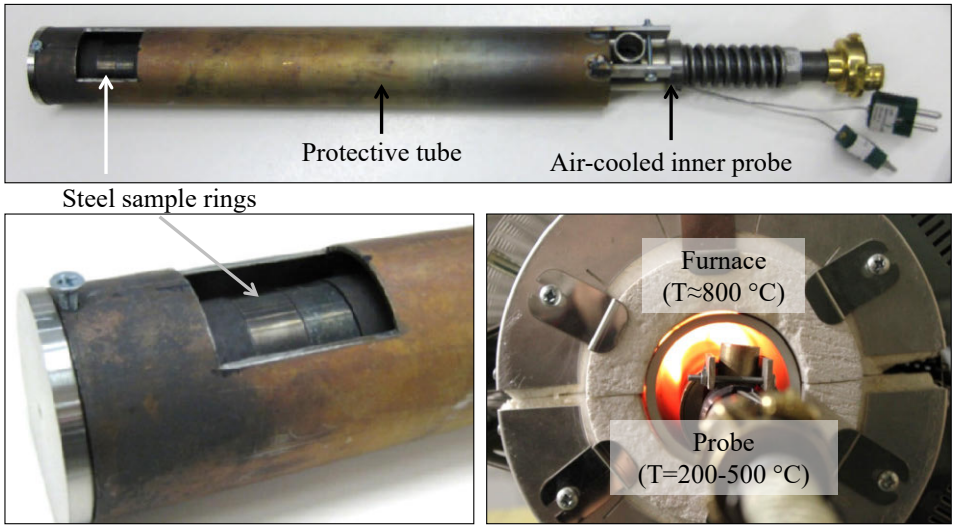

Fig. 1. Pictures of the temperature gradient probe. Adapted from Paper I.

During an experiment, the sample ring is covered with the salt deposit. A protective fire-sealant paste is applied to surround the edges of the rings, in order to maintain the salt in place in case of melting of the salts. The probe is inserted into a tube furnace, where it is heated up together with the furnace. During the experiment, the probe temperature is controlled at a constant temperature and the experiment is considered to begin once the probe reaches its target temperature. At the end of the experiment, the probe is cooled rapidly to room temperature by withdrawing it from the hot furnace and by continuing the air-cooling. A typical temperature profile during the experiments can be seen in Fig. 2. The temperature of the probe was controlled at 200-500 °C and the furnace temperature was set to 980 °C, which resulted in a measured temperature of ~800 °C above the salt deposits.

In Papers I, II, and IV, the two steel rings were either both covered with the same deposit material or only the control ring was covered with the deposit material. In Paper V, the two steel rings were covered with different deposit materials in order

to study, whether the deposit material covering one of the rings vaporizes and then condenses in the deposit covering the other ring.

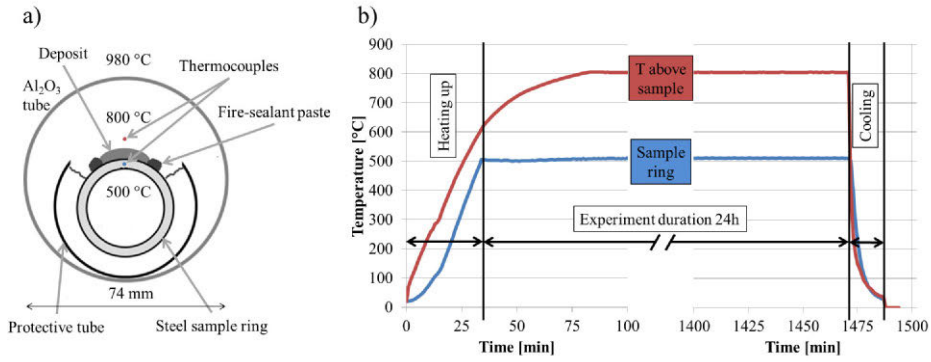

Fig. 2. (a) Schematic image of the furnace and probe cross-section showing a typical temperature profile during an experiment. (b) A figure showing the measured temperatures of the probe and the furnace as a function of time, during an experiment. The heating and cooling steps in the experiment in question were ~35 min and ~10 min respectively. Reprinted with permission from Paper II. Copyright © 2017 Elsevier.

The compositions of the steel grades of the sample rings are shown in Table 2.

Table 2. Standard chemical compositions of EN10216-2 10CrMo9-10 and P235GH steels in wt-%, the rest is Fe.

Steel	C	Si	Mn	P	S	Cr	Mo	N	Cu	Cr+Cu+Mo+Ni
10CrMo9-10	0.08-0.14	≤ 0.5	0.4-0.8	≤ 0.02	≤ 0.01	2.0-2.5	0.9-1.1	≤0.012	≤0.3	
P235GH	≤ 0.16	≤ 0.35	≤ 1.20	≤ 0.025	≤ 0.010					≤ 0.70

3.1.3 Entrained flow reactor

The entrained flow reactor of the University of Toronto was the main experimental equipment used in Paper III.

The entrained flow reactor consists of a natural gas burner, situated at the top of the reactor, and of an electrically heated section. Fuel or ash is fed into the reactor from the top. The material fed into the reactor is entrained into a natural gas flame.

In earlier work, an air-cooled deposit probe has been inserted at the bottom of the reactor in an opening, which is not heated [91]. For this work, a new probe was

designed and tested. The probe consists of two concentric tubes: an inner tube, which introduces the cooling air into the probe, and an outer tube, which is in contact with the flue gas from the reactor. As the probe is smaller in size than the deposit probe used in the earlier studies, it can be inserted into the electrically heated section of the reactor, where a temperature gradient is present from the flue gas to the probe surface.

In addition, two detachable C-rings were added to the probe. Thermocouples were placed between the probe and the C-rings to control and measure the probe temperature during experiments. The temperature of the probe was controlled at 500 °C, while the entrained flow reactor was operated at 800 °C. Figure 3 depicts the experimental set-up.

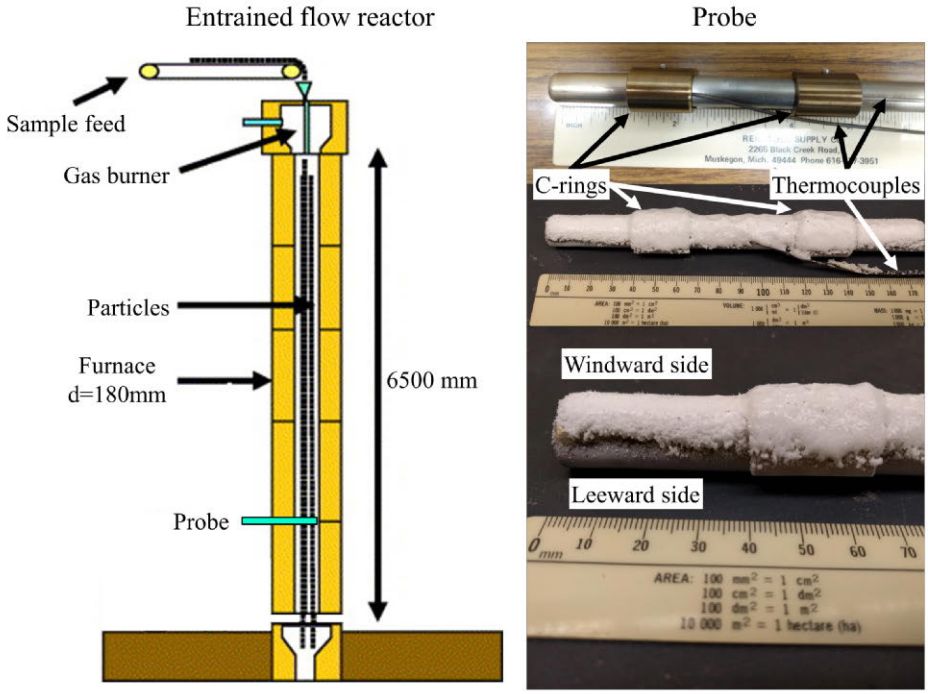

Fig. 3. Entrained flow reactor (left) and the probe before and after an experiment (right). Reprinted with permission from Paper III. Copyright © 2018 PAPTAC.

The experiments were stopped by withdrawing the probe from the hot furnace into room temperature and quenching the probe and the deposits. The cooled-down C-rings were carefully detached from the probe and prepared for analyses.

3.1.4 Sample preparation

The deposit samples from the temperature gradient furnace experiments and from the entrained flow reactor experiments were cast in epoxy resin together with the steel sample rings. The samples were cut for a cross-section. The cross-sections were polished, cleaned, carbon-coated, and subsequently analyzed using SEM/EDX.

3.2 Deposit characterization

3.2.1 Scanning electron microscopy/energy-dispersive X-ray spectroscopy

Scanning electron microscopy (SEM) was used to characterize the cross-sections of the samples. The working principle of SEM is to scan a material surface with a focused electron beam. The electrons from the beam interact with the atoms of the sample, resulting in a wide range of different signals. The main signal used in this work was the backscatter electron signal. The backscatter electrons are electrons from the beam that hit the sample and subsequently scatter back from the sample atoms. Heavier atoms hit by the electron beam result in more backscatter electrons than lighter atoms, which results in contrast in areas with different atomic compositions. The areas containing heavier atoms appear as lighter color in the images than the areas containing lighter atoms, which appear in a darker color. The SEM backscatter images were used to get information on the composition and morphology of the sample cross-sections.

The SEM was used in combination with energy-dispersive X-ray spectroscopy (EDX). The EDX is a spectroscopy technique where the sample is stimulated with X-ray radiation. The X-ray radiation excites sample electrons from the unexcited ground state to an excited state, resulting in an electron-hole on the electron shell where the electron originally resided. An electron from a higher-energy electron shell descends to the lower-energy electron shell and fills the electron-hole. Simultaneously, X-ray radiation with the energy corresponding to the difference between the higher-energy and lower-energy electron shells is emitted. The emitted X-ray spectrum is measured. The energy differences between the energy shells are element-specific, which enables the measurement of the elemental compositions of the sample. The EDX was used to analyze the atomic composition of spots and larger areas within the samples and to produce elemental maps of desired areas within the samples.

Energy-dispersive X-ray spectroscopy provides information on the elemental composition of the analyzed spot or area but does not provide information on the phase composition of the sample. However, SEM/EDX was deemed adequate for

the purposes of this study as the phase compositions of the studied salt systems are relatively simple and well known, and there were only a handful of elements present in the synthetic deposits. In addition, the SEM/EDX analyses were complemented with thermodynamic modeling. The results from the thermodynamic modeling further strengthened the indications of phase compositions. However, due to the limitations of the SEM/EDX, the solid phases in the samples were indicated but not confirmed.

The SEM/EDX analyses reported in this thesis were conducted with a LEO Gemini 1530 equipped with a ThermoNORAN Vantage X-ray analyzing system manufactured by Thermo Scientific. The resolution of the SEM is ~10 nm, while the detection limit of the EDX is ~0.1 wt-%, both of which were deemed adequate for the purposes of the work presented in this thesis.

3.2.2 Differential scanning calorimetry/thermogravimetric analysis

Differential scanning calorimetry/thermogravimetric analysis (DSC/TGA) was used to evaluate the melting properties of the salts and salt mixtures used in the experiments. DSC is a technique able to detect phase transitions from the amount of heat released or consumed during a chemical reaction of phase change. The DSC/TGA was used to characterize the melting properties of the deposit materials used in this thesis. The analyses were conducted with a TA Instruments SDT Q600 device. The mixtures were heated above the solidus or liquidus temperature and cooled down in multiple cycles. Heating and cooling rates of 20 °C min^{-1} and a gas flow of 100 mL min^{-1} of N_2 were applied. The solidus and liquidus temperatures were extracted from the raw data. The information was used together with the results from the thermodynamic modeling.

3.3 Modeling

3.3.1 Thermodynamic modeling

Thermodynamic modeling is a tool to predict the chemical behavior of a complex system. The modeling is often based on the minimization of Gibbs energy. In order to correctly predict a system by the minimization of Gibbs energy, there needs to be thermodynamic information on the phases of the system. In this thesis, the modeling software FactSage [62] was applied for the evaluation of the melting properties and phase compositions of the tested salt systems. The saturation pressures of alkali halides, which were used as input data in the alkali halide-migration model, were obtained from the FactSage calculations. The FTsalt database was used in the calculations as such, with the exception of the alkali bromide-alkali sulfate mixtures.

The FTsalt database lacks the interaction parameters for NaBr-Na_2SO_4 and KBr-K_2SO_4 systems. However, the systems have been studied experimentally [92-96] and they seem to be similar to the corresponding alkali chloride-alkali sulfate systems. Based on the experimental studies, the nonideal binary interaction parameters for the liquid phase were optimized in Paper IV. The optimization was done using the modified quasichemical model in the quadruplet approximation [97]. However, the details of the assessed thermodynamic parameters lie outside of the scope of this work.

3.3.2 Mathematical modeling

The alkali halide-migration within the gas phase was modeled in order to validate the hypothesized migration principle. The model is presented in detail in Paper II. The model relies on Fick's first law of diffusion and on the kinetic theory of gases. According to the Fick's first law of diffusion:

$$J_i = D_i \frac{dc_i}{dx} = D_i \frac{dc_i}{dT}\frac{dT}{dx} \quad (1)$$

where J_i is the diffusion flux, D_i is the diffusion coefficient and dT/dx is the temperature gradient. Concentration (c_i) of the alkali halide *i* was determined using Eq. 2, derived from the exponential dependence of alkali halide saturation pressures to the inverse absolute temperature and assuming ideal gas:

$$c_i = \exp\left(A_i T^{-1} + B_i\right) p R^{-1} T^{-1} \quad (2)$$

The derivation of Eq. 2 by temperature (T) gives Eq. 3:

$$\frac{dc_i}{dT} = pR^{-1}\left(-A_i T^{-3} \exp(A_i T^{-1} + B_i) - T^{-2} \exp(A_i T^{-1} + B_i)\right) \quad (3)$$

where p is pressure (101325 Pa), R is the gas constant, and A_i and B_i are species-dependent constants to calculate saturation pressures of alkali halides (see Table 3). Based on the kinetic theory of gases, diffusion coefficient (D_i) is determined by Eq. 4:

$$D_i = \frac{1}{3}\lambda_i \bar{c_i} \quad (4)$$

where λ is the mean free path of molecules (Eq. 5) and $\bar{c}$ is the mean speed of molecules (Eq. 6):

$$\lambda_i = k_B T\left(\sqrt{2} d_i^2 \pi p\right)^{-1} \quad (5)$$

$$\bar{c_i} = \sqrt{8RT(\pi \mu_i)^{-1}} \quad (6)$$

where k_B is the Boltzmann constant, d_i is the effective molecule diameter of *i* and μ_i is the effective mass of *i* in a N_2 atmosphere (see Table 3).

Table 3. Molecule dependent constants for determining the saturation pressures (A_i and B_i) of alkali chlorides and alkali bromides [62], effective molecular diameters in N_2 atmosphere ($d_{i,eff}$) [98-102], effective mass in N_2 atmosphere (μ_i) [98, 102], and density of solids at room temperature (ρ_i) [98].

i	A_i [K]	B_i [-]	$d_{i,eff}$ [m]	μ_i [kg]	ρ_i [kg m-3]
KCl	-26247	17.55	3.54E-10	3.38E-26	1990
$(KCl)_2$	-30058	20.61	4.48E-10	3.92E-26	1990
NaCl	-27159	17.64	3.29E-10	3.14E-26	2170
$(NaCl)_2$	-30074	20.19	4.29E-10	3.75E-26	2170
KBr	-24298	16.07	3.68E-10	3.77E-26	2750
$(KBr)_2$	-27388	18.08	4.74E-10	4.16E-26	2750
NaBr	-24850	16.19	3.41E-10	3.66E-26	3210
$(NaBr)_2$	-26308	17.25	4.54E-10	4.10E-26	3210

The model takes into account the absolute temperature of the particle on top of which the deposition occurs and the steepness of the temperature gradient. As alkali halides vaporize into the gas phase from the steel-facing side of the particles, and the outer part of the particle-of-origin is depleted of alkali halides, the alkali halides need to diffuse to the surface from the inner parts of particles. This effect is illustrated schematically in Fig. 4.

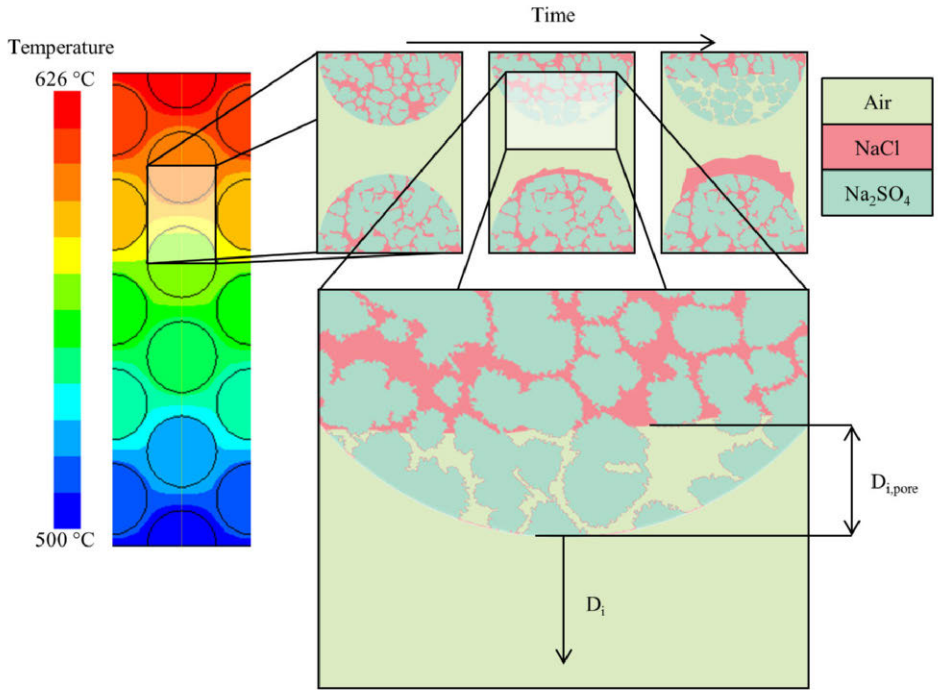

Fig. 4. On the left, a computational fluid dynamics calculation grid showing the temperature field in a two-phase solid-gas system for NaCl-Na_2SO_4 system, where temperature gradients are enhanced from particle-to-particle in comparison to bulk. On the right, a schematic image showing the alkali halide-migration effect and changes to the particle-of-origin microstructure as a function of time. The effective diffusion coefficient $D_{i,eff}$ decreases as a function of time as the contribution of D_i decreases and the contribution of $D_{i,pore}$ increases. Reprinted with permission from Paper II. Copyright © 2017 Elsevier.

In the model, the longer diffusion path within the alkali sulfate matrix decreases the effective diffusion coefficient, which is expressed in Eq. 7 [103]:

$$D_{i,pore} = D_i/\tau^2 \quad (7)$$

where tortuosity (τ) is defined according to Eq. 8 [104]:

$$\tau^2 = \varepsilon/(1-(1-\varepsilon)^{\frac{1}{3}}) \quad (8)$$

where ε is the porosity of the alkali halide depleted alkali sulfate skeleton.

Due to the similar densities of alkali chlorides and their respective sulfates, the weight fraction of the alkali chlorides in the original deposit compositions were used as the porosity values ($\varepsilon = m_{XCl}/(m_{XCl} + m_{X2SO4})$) in the calculations in the Paper II. In Paper IV, the difference of the densities of alkali sulfates and alkali

bromides were taken into account and the volume fraction of the alkali bromides was used as the porosity values ($\varepsilon = V_{XBr}/(V_{XBr} + V_{X2SO4})$). The effective diffusion coefficient $D_{i,eff}$ is calculated using Eq. 9:

$$\frac{1}{D_{i,eff}(t)} = \frac{x_i(t)}{(x_i(t)+x_{pore}(t))*D_i} + \frac{x_{pore}(t)}{(x_i(t)+x_{pore}(t))*D_{i,pore}} \quad (9)$$

which describes diffusion within the alkali sulfate network and in the particle-to-particle gap in series and where $x_i(t)$ is the particle-to-particle distance at time t (Eq. 10) and $x_{pore}(t)$ is the thickness of the depleted layer at time t (Eq. 11):

$$x_i(t) = x(0) - \Delta x(t) \quad (10)$$

$$x_{pore}(t) = \Delta x(t)/\varepsilon \quad (11)$$

where x(0) is the particle-to-particle distance at the start of an experiment and Δx(t) is the condensed layer thickness at time t. Combining Eq. 9-11 gives Eq. 12:

$$D_{i,eff}(t) = ((x(0) - \Delta x(t))/((x(0) - \Delta x(t)(1 + 1/\varepsilon)) * D_i) + (\Delta x(t)/\varepsilon)/ ((x(0) - \Delta x(t)(1 + 1/\varepsilon)) * D_{i,pore}))^{-1} \quad (12)$$

In the calculations, x(0)=50 μm was used. In Paper IV, the x(0)=50 μm was also used as a maximum layer thickness in the calculations.

The total diffused alkali halide amount was gained from Eq. 1 by substituting D_i with $D_{i,eff}$ and numerically integrating in time with 10 s intervals. The thickness of the resulting alkali halide layer is calculated using the densities (ρ) (Table 3) of pure alkali halides and adding the transported amounts of monomers and dimers.

Equation 1 shows that the diffusion flux J_i is directly proportional to the temperature gradient. Computational fluid dynamics modeling was used to estimate the particle-to-particle temperature gradient from the bulk temperature gradient over the porous region of the deposit. Simple geometry with uniformly distributed 150 μm diameter spheres, with thermal conductivity of 5 W/(m K), and a particle-to-particle distance of 50 μm in a 2-D plane was used. A thermal conductivity value of 0.05 W/(m K) was used for the air between particles. The particle-to-particle distance was chosen based on the experimental observations and so that the 1-D solids fraction in the y-axis in the model (0.75) corresponds to the solids fraction of close packing structures (0.74). The particle-to-particle temperature gradient was ~3.7 times steeper than the bulk temperature gradient over the porous deposit. The temperature field calculations were conducted using the commercial software Fluent.

Alkali halide layer thickness profiles were calculated for all of the individual temperature gradient experiments where alkali halide-migration was observable. The corresponding estimated temperature gradients and exposure times were used

in the calculations and the modeled values were compared to the measured ones in Papers II and IV.

4 RESULTS AND DISCUSSION

4.1 Salt systems/Synthetic ash deposits

The deposits formed multilayered deposit structures, which could be divided into a subsolidus region and a supersolidus region, according to whether the deposit region had experienced melting during the experiment or not. In general, the subsolidus region had retained the particulate structure of the unaged deposit. The supersolidus region had sintered noticeably, due to the formation of melt. The original particle shapes had rounded and/or the deposit supersolidus structure had changed to a dense monolith-like structure.

4.1.1 NaCl-Na_2SO_4

The NaCl-Na_2SO_4 system was studied in the temperature gradient furnace (Papers I and II) as well as in the entrained flow reactor (Paper III). The phase diagram of the system is shown in Fig. 5. The temperature gradient furnace experiments were conducted with steel temperatures ranging from 300 to 500 °C, while the exposure times varied from 4 to 72h.

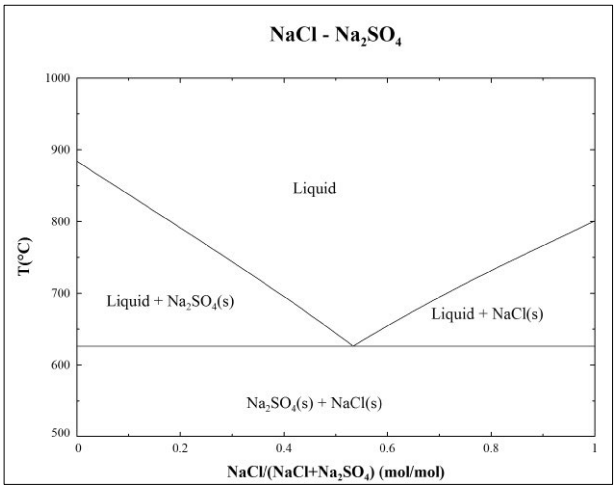

Fig. 5. Phase diagram of the NaCl-Na_2SO_4 system.

The NaCl-Na_2SO_4 system showed densification and species migration in all of the temperature gradient experiments. Next to the steel surface, a clear subsolidus region was observed in all of the experiments. Closer to the hot flue gas, a supersolidus region was observed in all of the experiments. The supersolidus region had a dense morphology, with segregation between species, in experiments with compositions deviating from the eutectic point composition of the NaCl-Na_2SO_4 system. In these experiments, the supersolidus region could be further

divided into different regions, distinguishable by the composition. An example of a deposit morphology after 24h exposure is shown in Fig. 6.

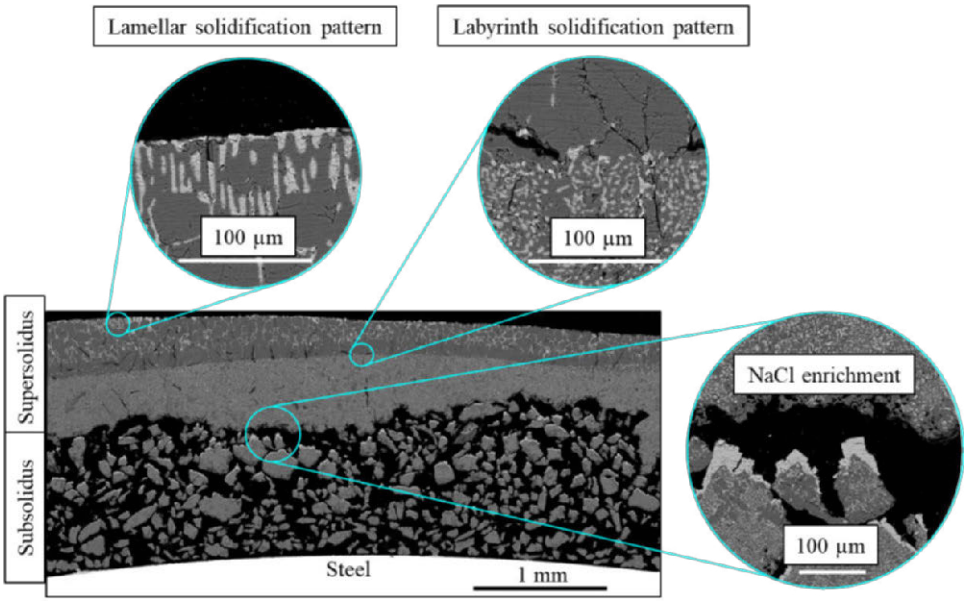

Fig. 6. Deposit cross-section of a synthetic NaCl-Na_2SO_4 deposit. The image shows the sub- and supersolidus regions, lamellar and labyrinth solidification patterns in the supersolidus region, and the NaCl enrichment on the furnace-facing sides of the salt particles in the subsolidus region.

At the interphase of the sub- and supersolidus regions, there was a region that was enriched in the "minor" component, i.e. the component not present in the primary crystallizing phase. Due to the enrichment, the region had a composition close to the eutectic point composition. In some experiments, a solidified eutectic melt surrounded the primary crystallizing phase (see Fig. 7). Moving toward the hotter temperature, sharp interphase was observed. The near eutectic composition rapidly changed to a pure composition of the primary crystallizing phase.

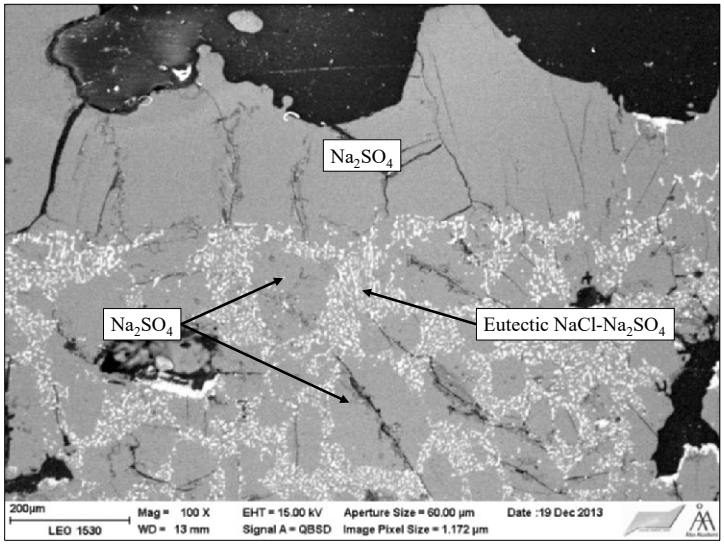

Fig. 7. SEM backscatter image showing the eutectic melt (NaCl-Na_2SO_4) surrounding primary crystallizing phase (Na_2SO_4) crystals. Adapted from Paper I.

The length of the exposure time affected the chemistry and morphology of the deposits. In the supersolidus region, for shorter exposures (4-24h), eutectic pockets were observed within the dense supersolidus layer, while for the longer exposures (72h), no such pockets were found. In a number of experiments, lamellar solidification patterns were observed in the hotter part of the supersolidus region (see Fig. 6). Lamellar structures are formed when using a large difference between the melt and quench temperatures [105]. The large temperature difference corresponds to the temperature conditions in the upper supersolidus region during quenching. The formation mechanism of the solidification pattern is further discussed in Section 4.2.3.

The steel temperature affected the distance of the supersolidus region from the steel surface, i.e. a hotter steel temperature resulted in a shorter distance. Otherwise, the steel temperature did not affect the deposit morphology in a significant way.

In the subsolidus region, a migration of NaCl towards the steel surface was observed. NaCl crystals were found on the furnace-facing sides of the deposit particles, as well as on the steel/oxide surface. The migration occurred to a higher degree, with longer exposure time and with compositions containing more NaCl. In addition, the size of the crystals increased with the local temperature within the subsolidus region of the deposit. The crystal growth was due to the vaporization of NaCl in the hotter parts of the deposit and subsequent condensation of NaCl in the colder parts of the deposit. The phenomenon is further discussed in Section 4.2.1.

Experiments carried out with the entrained flow reactor (Paper III) showed similar results as the temperature gradient furnace experiments. The only mentionable difference was that the particles in the subsolidus region were observed to be more connected to each other. The behavior occurs because the particles were in a molten phase when they hit the probe. Therefore more agglomeration occurred compared to the temperature gradient furnace experiments where the particles were never in the molten phase during the experiment.

The results from the entrained flow reactor experiments show that the initial deposit structure evolved quickly. The formation of the NaCl enriched region at the subsolidus-supersolidus interface occurred already at the build-up phase (90 min). With additional aging (150 min) the region closest to the flue gas was observed completely devoid of NaCl, as seen from Fig. 8.

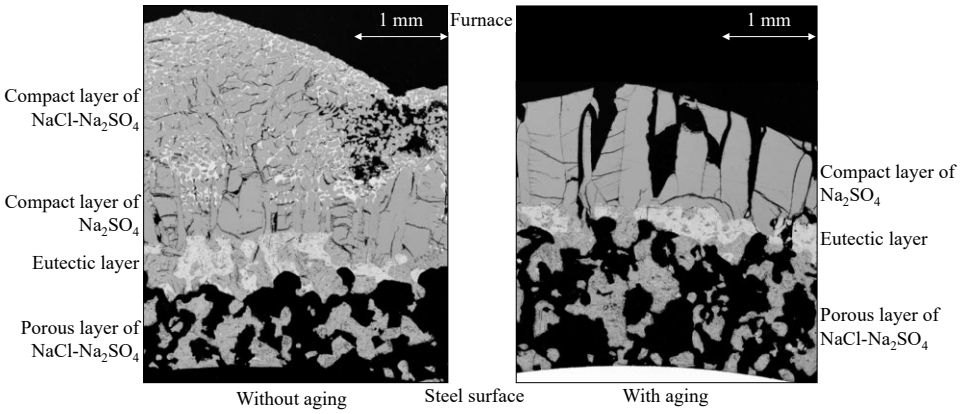

Fig. 8. SEM backscatter images of the cross-sections of the NaCl-Na_2SO_4 deposits without aging (left) and with aging (right) collected from the entrained flow reactor. Reprinted with permission from Paper III. Copyright © 2018 PAPTAC.

4.1.2 KCl-K_2SO_4

The KCl-K_2SO_4 system was studied in the temperature gradient furnace (Papers I and II), as well as in the entrained flow reactor (Paper III). The phase diagram of the system is shown in Fig. 9. The temperature gradient furnace experiments were conducted with steel temperatures ranging from 300 to 500 °C, while the exposure times varied from 4 to 72h.

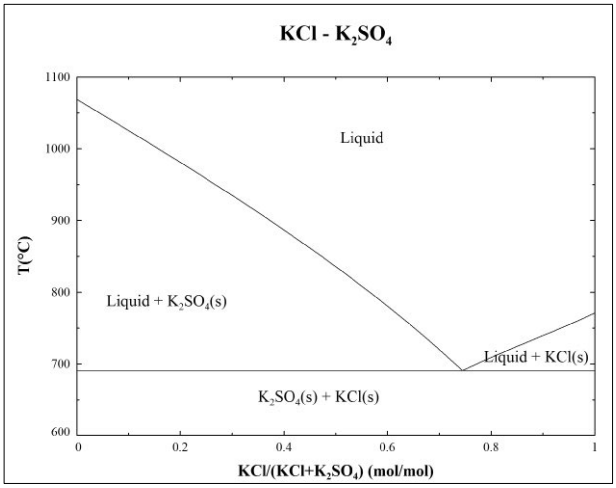

Fig. 9. Phase diagram of the KCl-K_2SO_4 system.

The KCl-K_2SO_4 system showed densification and species segregation in all of the temperature gradient experiments. A clear subsolidus region was observed in all of the experiments. Closer to the hot flue gas, a supersolidus region was found in all of the experiments. The supersolidus region had either a dense morphology or a more porous network-like structure, depending on the original deposit composition. With the 11 wt-% KCl composition, which has a low melt fraction (20-30 wt-%) at the temperature range of 690-800 °C, a network-like supersolidus structure was observed. The supersolidus structure type was mainly connected to the melt fraction of the deposit; the phenomenon will be discussed in more detail in Section 4.2.2. The steel temperature affected the ratio between the supersolidus and subsolidus; with higher steel temperature, the subsolidus layer was thinner than with lower steel temperature.

In experiments with compositions deviating from the eutectic point composition of the KCl-K_2SO_4 system, segregation between species was observed. The species segregation in the supersolidus region was observed with both dense and network-like supersolidus morphologies. Similar to the NaCl-Na_2SO_4 system, at the interphase of the sub- and supersolidus regions, a region with near-eutectic composition was found. In experiments, which displayed a dense morphology, when moving toward the hotter temperature, sharp interphase was observed. The near-eutectic composition rapidly changed to the primary crystallizing phase, with possible melt pockets within the solid structure. In the experiments with the network type supersolidus region, the interphase was not as clear.

In the subsolidus region, a migration effect of KCl was observed. KCl crystals were found on the furnace-facing sides of the deposit particles, as well as on the

steel/oxide surface. The migration was similar to the migration of NaCl, i.e. larger crystals were observed with longer exposure time, with compositions containing more KCl, and with higher local temperature within the subsolidus region of the deposit. In addition, the growth rate of KCl crystals decreased as a function of time. Similar to NaCl, the crystal growth was due to a vaporization-condensation mechanism of KCl and the phenomenon is discussed in more depth in Section 4.2.1.

Experiments carried out with the entrained flow reactor (Paper III) showed similar results as the temperature gradient furnace experiments. However, some differences were observed. In the subsolidus region, the particles were more connected to each other. In addition, the salt composition with 11 wt-% KCl used in the entrained flow reactor experiments resulted in a dense supersolidus layer, while in the temperature gradient furnace experiments it resulted in a network-like supersolidus structure, even though the particle size fraction used in the entrained flow reactor experiments was larger. The behavior, for both the subsolidus and supersolidus regions, occurred likely because the particles were in a molten phase when they hit the probe, thus leading to an initially denser deposit.

The results from the entrained flow reactor experiments show that the initial deposit structure evolved quickly. The formation of the KCl enriched region at the subsolidus-supersolidus interface had formed during the deposition stage. With additional aging, the pure K_2SO_4 region grew (60 min aging), and finally, the region closest to the flue gas was completely devoid of KCl (150 min aging), as seen from Fig. 10.

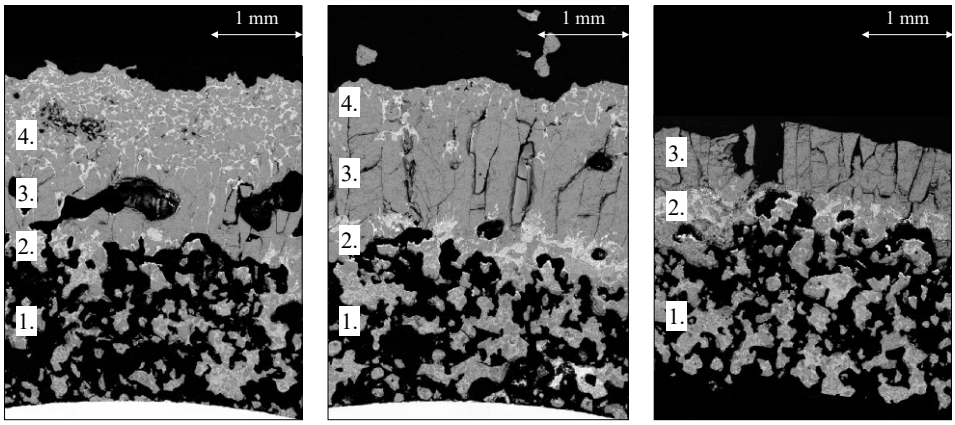

Fig. 10. SEM backscatter images of the cross-sections of the KCl-K_2SO_4 deposits without aging (left), with 60 min aging (middle), and with 150 min aging (right) collected from the entrained flow reactor. The numbered regions within the deposits were: 1. porous layer of KCl-K_2SO_4 with the original material feed composition, 2. eutectic layer, 3. K_2SO_4 rich layer, and 4. compact layer of KCl-K_2SO_4 with a composition close to the original material feed. Reprinted with permission from Paper III. Copyright © 2018 PAPTAC.

4.1.3 K-Na-Cl-SO_4

The K-Na-Cl-SO_4 system was studied using the entrained flow reactor, by using sequential feeding of NaCl-Na_2SO_4 and KCl-K_2SO_4 mixtures into the reactor (Paper III). The liquidus projection diagram of the K-Na-Cl-SO_4 system is shown in Fig. 11. The system was studied by initially feeding one mixture into the entrained flow reactor, followed by the second mixture. The amounts of the salts fed were 150 g (feed time 70 min) for the main mixture and 50 g (feed time 20 min) for the second mixture. The deposits were collected either immediately after the material feed was concluded or after an additional 150 min aging period. The experiment parameters are summarized in Table 4.

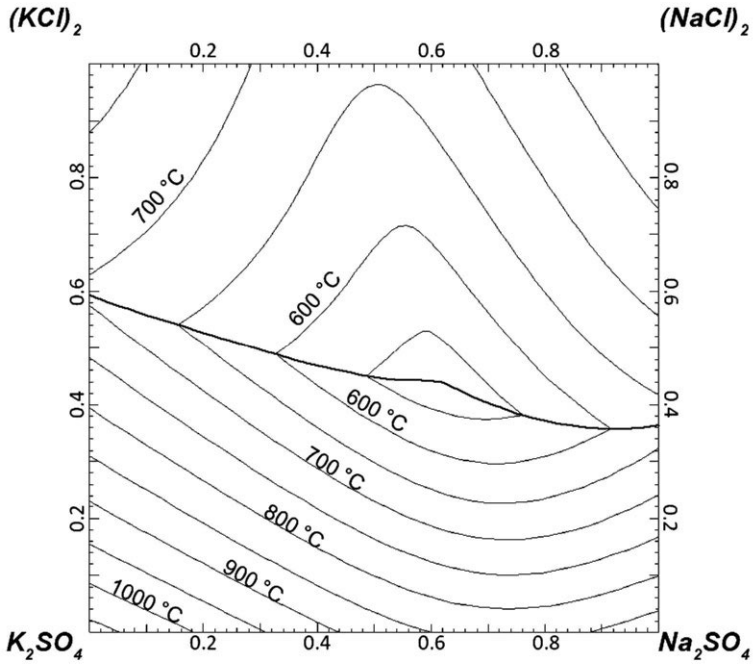

Fig. 11. The liquidus projection diagram of the K-Na-Cl-SO_4 system [70].

Table 4. Experiments conducted with the K-Na-Cl-SO_4 system in the entrained flow reactor.

Main feed		**Addition**		**Feed time**	**Aging**	**C-ring temperature**	
Material	Amount (g)	Material	Amount (g)	(min)	(min)	#1 (°C)	#2 (°C)
NaCl-Na_2SO_4	150	KCl-K_2SO_4	50	70+20	-	432	500
NaCl-Na_2SO_4	150	KCl-K_2SO_4	50	70+20	150	425	500
KCl-K_2SO_4	150	NaCl-Na_2SO_4	50	70+20	-	458	500
KCl-K_2SO_4	150	NaCl-Na_2SO_4	50	70+20	150	472	500

The unaged deposits showed only minor mixing between the two systems. The overall morphology was similar to experiments where only NaCl-Na_2SO_4 or KCl-K_2SO_4 was fed into the entrained flow reactor, but the sequential material feeding led to a formation of four distinct regions within the deposit as seen from Fig. 12. The regions are the following: 1. The region closest to the steel consisted of the material that was fed into the entrained flow reactor first and had a porous structure. 2. The following region was enriched in the alkali chloride corresponding to the material that was fed into the entrained flow reactor first. 3.

The next region consisted of alkali sulfates. The region displayed a gradient in the alkali metal ratio, i.e. the amount of the alkali metal in the main feed was higher closer to the steel and decreased towards the flue gas. 4. The outermost layer consisted of a mixture of alkali chlorides and sulfates with similar alkali metal ratio gradient as in the third layer.

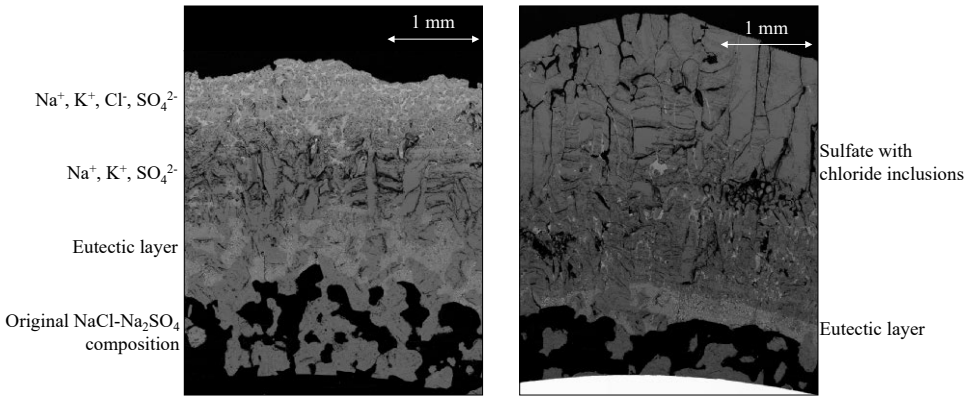

Fig. 12. Deposit of NaCl-Na_2SO_4 with KCl-K_2SO_4 addition, without aging and steel temperature at 432 °C (left), and with 150 min aging and steel temperature at 425 °C (right). Reprinted with permission from Paper III. Copyright © 2018 PAPTAC.

The aging of the deposits resulted in the evolution of the deposit chemistry and morphology. The porous region closest to the steel surface became thinner in all experiments and in one experiment no porous region could be observed. The porous region retained the bulk chemical composition of the original material fed into the reactor. The following region was dense and enriched in alkali chlorides, but differing from the unaged deposit, it contained both alkali metals. The next layer was a mixed alkali sulfate layer with both alkali metals present. Although the alkali metal ratio gradient was still observed, the alkali metals were more evenly distributed across the deposits. In addition, some alkali chloride rich inclusions were identified within the sulfate structure.

Within the porous layer, an enrichment of alkali chlorides on the furnace-facing sides of particles was observed in all of the experiments. The alkali chloride composition corresponded to the initial material fed into the reactor.

4.1.4 NaBr-Na_2SO_4

The NaBr-Na_2SO_4 system was studied in the temperature gradient furnace (Paper IV). The system was studied with varying exposure times (2, 4, and 8h), while a constant steel temperature of 500 °C was used. The overall deposit structure and the aging effect in the supersolidus region are shown in Fig. 13.

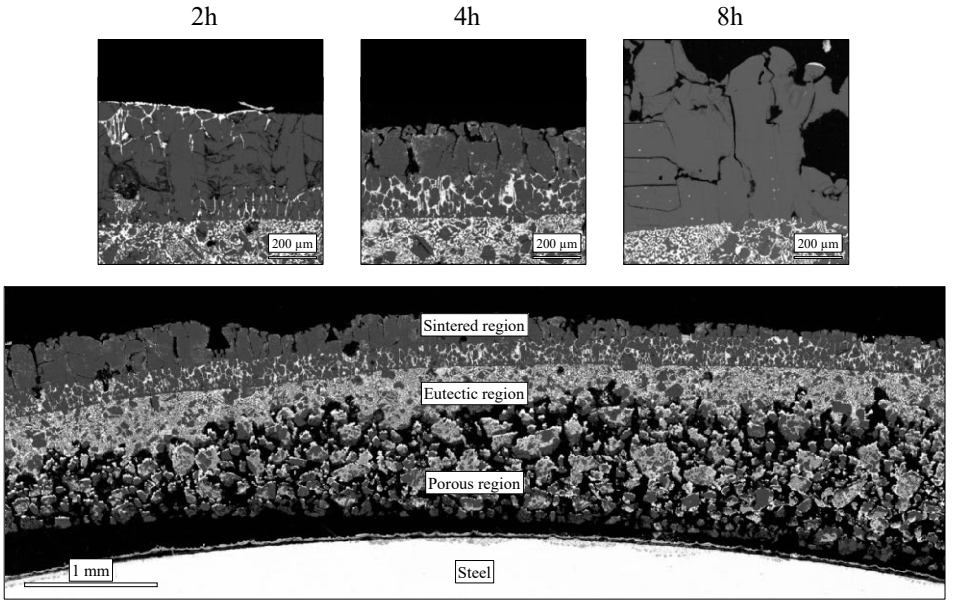

Fig. 13. SEM backscatter image of the overall deposit structure of the NaBr-Na_2SO_4 deposit and of the evolution of the supersolidus layer. Adapted from Paper IV.

The phase diagram of the system is shown in Fig. 14. The thermodynamic interaction parameters for the NaBr-Na_2SO_4 system have not been published previously and are thus not included in the FTSalt database. However, the phase equilibria of NaBr-Na_2SO_4 has been studied experimentally by Rea [92], Palkin et al. [93], Flood et al. [95], and Nyankovskaya [96].

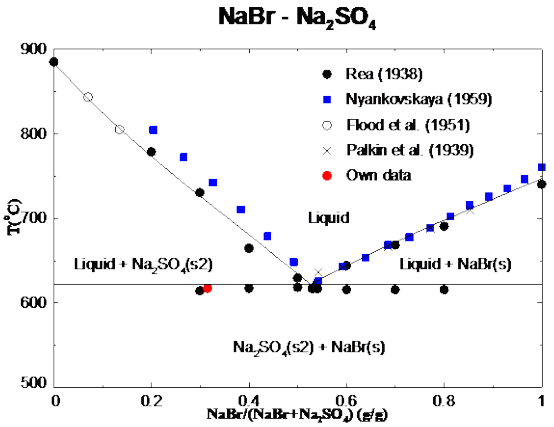

Fig. 14. Calculated phase diagram of NaBr-Na_2SO_4 on mass basis together with the experimental data of the system. Reprinted with permission from Paper IV under a CC-BY-4.0 license. Copyright © 2019 American Chemical Society.

The $NaBr$-Na_2SO_4 system showed densification and species migration in all of the temperature gradient experiments. Next to the steel surface, a porous subsolidus region was identified. Closer to the hot flue gas, a dense supersolidus region was observed in all of the experiments. Next to the porous subsolidus region, there was a NaBr enriched region, and closer to the flue gas a Na_2SO_4 enriched region was observed.

The structure of the deposits evolved as a function of time. The 2h experiments showed, in general, more alkali bromides in the uppermost layer. The amount of alkali bromides in the uppermost region decreased in the 4h and 8h experiments (Fig. 13). In general, already the 2h experiments displayed a dense supersolidus region, indicating that the densification occurred within a short time span.

In subsolidus temperatures, pure NaBr layers were found on the furnace-facing sides of particles and on the oxide layer. In addition, on the steel-facing sides of the particles, NaBr depleted areas were identified. The thicknesses of the NaBr layers within the porous region grew as functions of temperature and time. The layer thickness growth rate decreased as a function of time.

4.1.5 KBr-K_2SO_4

The KBr-K_2SO_4 system was studied in the temperature gradient furnace (Paper IV). The system was studied with varying exposure times (2, 4, and 8h), while a constant steel temperature of 500 °C was used throughout. The overall deposit structures were similar to the $NaBr$-Na_2SO_4 system.

The phase diagram of the system is shown in Fig. 15. The thermodynamic interaction parameters for the KBr-K_2SO_4 system have not been published previously and are not included in the FTSalt database. However, the phase equilibria of KBr-K_2SO_4 has been studied experimentally by Rea [92] and Gromakov [94].

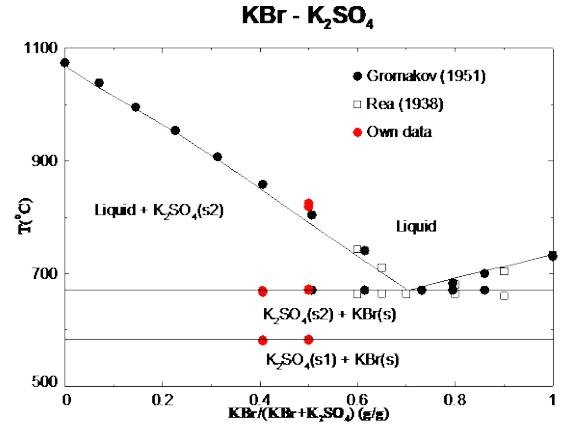

Fig. 15. Calculated phase diagram of KBr-K_2SO_4 on mass basis together with the experimental data of the system. Reprinted with permission from Paper IV under a CC-BY-4.0 license. Copyright © 2019 American Chemical Society.

The structure of the deposits evolved as a function of time. The 2h experiments showed, in general, more KBr in the uppermost layer. The amount of KBr in the uppermost region decreased in the 4h and 8h experiments (Fig. 16). The uppermost layer was dense in all of the experiments. In the 8h experiments, the uppermost layer had some porosity, which can be explained by the vaporization of the KBr into the furnace.

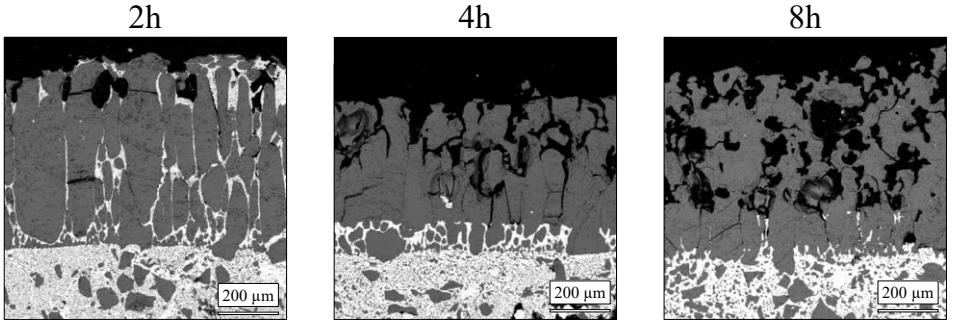

Fig. 16. The evolution of the supersolidus region of the KBr-K_2SO_4 system. Adapted from Paper IV.

Pure KBr layers were observed on the furnace-facing sides of particles and on the oxide layer, within the subsolidus region of the deposit. In addition, KBr depleted areas had formed in the steel-facing sides of the deposit particles. The thicknesses of the KBr layers grew within the porous region as functions of temperature and time. In contrast, the layer thickness growth rate decreased as a function of time.

4.1.6 $PbCl_2$-SiO_2

$PbCl_2$ and SiO_2 were studied in the temperature gradient furnace (Paper V). The $PbCl_2$ and SiO_2 were initially applied on two rings, separated by a wall, which was made out of fire-sealant paste. The approach is illustrated in Fig. 17. The gas phase migration of $PbCl_2$ into the SiO_2 deposit was studied using the steel temperatures 200 and 400 °C and for the exposure times of 4 and 24h.

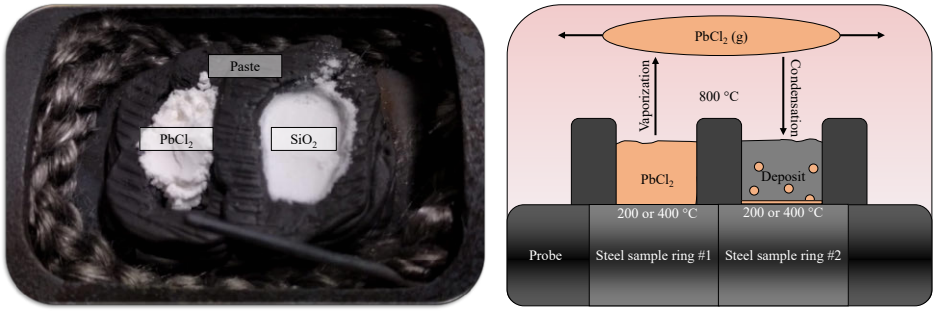

Fig. 17. On the left, a picture of the temperature gradient probe, with $PbCl_2$ and SiO_2 on different steel rings, separated by a fire-sealant paste. On the right, a schematic image of the set-up, showing the $PbCl_2$ vaporization from the source deposit and subsequent condensation within the target deposit. Adapted from Paper V.

In the experiment with steel temperature at 200 ° C, after 24h exposure, no $PbCl_2$ was observed in the SiO_2 deposit. However, $PbCl_2$ was observed to vaporize, diffuse, and condense into the SiO_2 deposit already after 4h, with steel temperature at 400 °C. The amount of $PbCl_2$ in the SiO_2 deposit seemed to decrease between the exposure times of 4 and 24h when the steel temperature was set at 400 °C. Although no $PbCl_2$ was found in the SiO_2 deposit after 24h, significant amounts of $PbCl_2$ were observed in the oxide layer at the steel surface, underneath the deposit. In addition, the amount of $PbCl_2$ in the source deposit had decreased significantly already after 4h.

The results suggest that $PbCl_2$ condensed within the SiO_2 deposit, and subsequently re-vaporized into the furnace as the partial pressure of $PbCl_2$ in the surrounding furnace air decreased due to the depletion of the source deposit.

4.1.7 NaCl-$PbCl_2$

The NaCl-$PbCl_2$ system was studied in the temperature gradient furnace. The salts were initially applied on separate test rings (Paper V). The steel temperature of 400 °C was tested for 4 and 24h exposures. The $PbCl_2$ was observed to migrate in the gas phase and to partly condense within the NaCl deposit. The condensed $PbCl_2$

induced melting in the NaCl deposit. The phase diagram of the NaCl-$PbCl_2$ system is shown in Fig. 18.

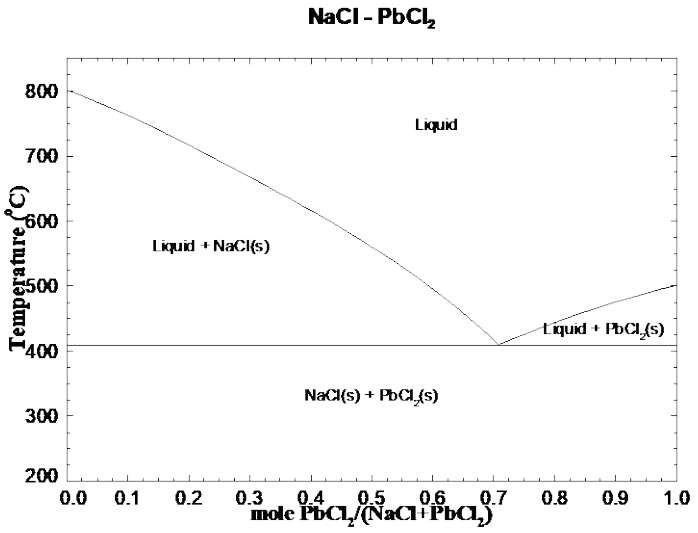

Fig. 18. Phase diagram of the NaCl-$PbCl_2$ system [106].

In the 4h experiment, the NaCl deposit showed signs of melting throughout and $PbCl_2$ was observed both within the deposit and on the oxide layer. $PbCl_2$ was entrapped within NaCl particles, indicating melting during the experiment.

In the 24h experiment, $PbCl_2$ was found only in the oxide layer. However, the whole NaCl deposit displayed an agglomerated structure, indicating that $PbCl_2$ had interacted with the NaCl deposit during the experiment. The lack of $PbCl_2$ in the deposit after 24h exposure suggests that the $PbCl_2$ later had re-vaporized from the NaCl deposit into the furnace atmosphere, similar to the $PbCl_2$-SiO_2 experiments. The $PbCl_2$ re-vaporized into the furnace due to a decrease in the partial pressure of $PbCl_2$ in the surrounding furnace atmosphere, due to the source deposit depletion.

4.1.8 Na_2SO_4-$PbCl_2$

The Na_2SO_4-$PbCl_2$ system was studied for 24h, using the steel temperatures at 200 °C and at 400 °C (Paper V). The $PbCl_2$ and the Na_2SO_4 were initially applied on separate sample rings. The vaporized and condensed $PbCl_2$ in the Na_2SO_4 deposit had induced both melting and chemical reactions in the Na_2SO_4 deposit.

With both steel temperatures, the deposit material had agglomerated during the experiments. In addition, new compounds, namely NaCl and $Na_3Pb_2(SO_4)_3Cl$ (caracolite) [107], were identified on the basis of the elemental ratios, in both of

the experiments. The compounds correspond to the reaction products in Reaction 1.

$$3\ Na_2SO_4 + 2\ PbCl_2 \rightleftharpoons Na_3Pb_2(SO_4)_3Cl + 3\ NaCl \quad (1)$$

In the experiment with the steel temperature at 200 °C, NaCl and $Na_3Pb_2(SO_4)_3Cl$ were found in a specific location within the Na_2SO_4 deposit. When comparing the deposit structure with the phase diagrams/thermodynamic calculations, the temperature in that location was assumed to have been close to 400 °C, during the experiment (see Fig. 19). Binary mixtures of NaCl-Na_2SO_4 and NaCl-$PbCl_2$ have solidus temperatures of 626 °C and 409 °C, respectively [106]. Although there is no thermodynamic data available for the NaCl-Na_2SO_4-$PbCl_2$-$PbSO_4$ system, the first melting temperature of the system is estimated to be close to the solidus temperature of the NaCl-$PbCl_2$ system, i.e. 409 °C, which corresponds well with the estimated temperature where the species were observed.

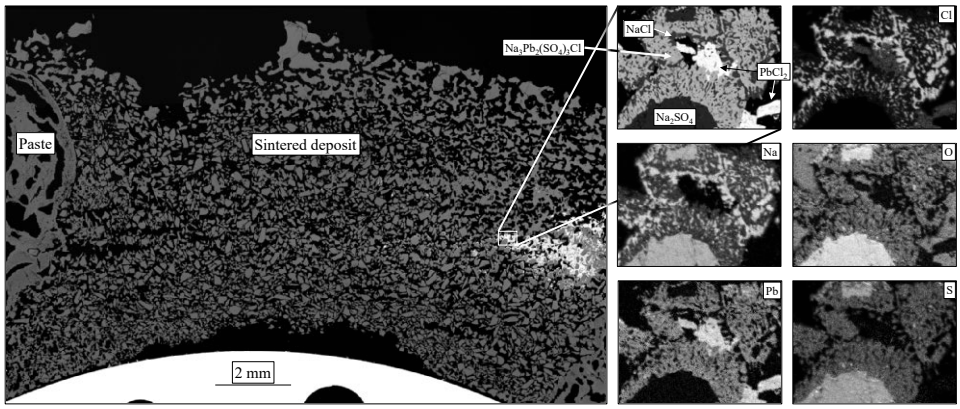

Fig. 19. Image of the Na_2SO_4 deposit after 24h, with steel temperature at 200 °C. On the right, elemental maps of the close-up, showing areas indicating NaCl, Na_2SO_4, $Na_3Pb_2(SO_4)_3Cl$, and $PbCl_2$. Reprinted with permission from Paper V under a CC-BY-4.0 license. Copyright © 2018 American Chemical Society.

In the experiment with steel temperature at 400 °C, Pb-containing species were not observed within the deposit. Instead, NaCl was found on the furnace-facing sides of Na_2SO_4 particles, indicating that Reaction 1 had taken place also in conditions experienced in the deposit during the 400 °C experiment. In the middle of the deposit, signs of melting were observed, thus indicating that melting had occurred at lower temperatures than the melting point of pure Na_2SO_4. The pure Na_2SO_4 has a melting point of 884 °C; therefore, the signs of melting indicate that Pb-containing species had been present in the deposit during the experiment. In addition, $Na_3Pb_2(SO_4)_3Cl$ was observed on top of the oxide layer, together with $PbCl_2$, which was also observed within and under the oxide layer.

4.1.9 KCl-$PbCl_2$

The KCl-$PbCl_2$ system was studied with the steel temperatures at 200 °C and at 400 °C in the temperature gradient furnace for 24h (Paper V). The salts were initially applied on separate sample rings. The $PbCl_2$ migrated via the gas phase to the KCl deposit and induced melting and reactions within the deposit.

With steel temperature at 200 °C, the uppermost KCl deposit seemed unaffected, i.e. it had not sintered and no Pb-containing species were observed. Pb-containing species were found in the form of K_2PbCl_4 in the deposit, in areas, which were estimated to have experiences the temperature range of 400-500 °C. The peritectic temperature of K_2PbCl_4 is 488 °C, which coincides well with the temperature of the region where the component was observed. The phase diagram of the KCl-$PbCl_2$ system is depicted in Fig. 20.

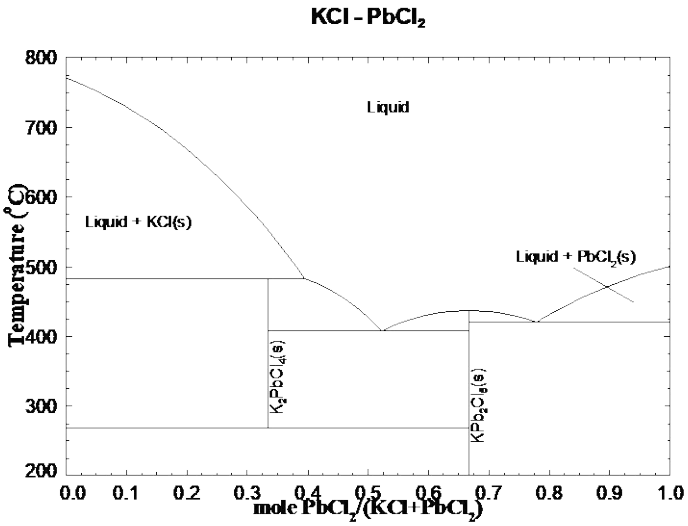

Fig. 20. Phase diagram of the KCl-$PbCl_2$ system [106].

With steel temperature at 400 °C, the results were similar, but the sintering of the deposit was more profound and more of the Pb-containing species were observed within the deposit. The Pb-containing species found within the KCl deposit were either located on the furnace-facing side of particles or entrapped within KCl particles. The Pb-containing species within the deposit were in the form of K_2PbCl_4. The possible formation mechanisms are presented in Reactions 2-4.

$$PbCl_2 + 2\ KCl \rightleftharpoons K_2PbCl_4 \quad (2)$$

$$PbCl_2 + KCl \rightleftharpoons KPbCl_3 \quad (3)$$

$$KPbCl_3 + KCl \rightleftharpoons K_2PbCl_4 \quad (4)$$

No KPb_2Cl_5 was observed within the deposit, which is likely due to the surplus of KCl compared to $PbCl_2$. $KPbCl_3$ is only present in the gas phase. The exclusive presence on the furnace-facing sides is a clear indication of gas phase migration being the responsible mechanism. Compared to the NaCl-$PbCl_2$ experiments, higher amounts of Pb-containing species were observed within the KCl deposit.

4.1.10 K_2SO_4-$PbCl_2$

The K_2SO_4-$PbCl_2$ system was studied, with the steel temperatures at 200 °C and at 400 °C in the temperature gradient furnace for 24h (Paper V). The salts were initially applied on separate sample rings.

With the steel temperature at 200 °C, only minor amounts of Pb and Cl were observed within the K_2SO_4 deposit, in between K_2SO_4 particles. In addition, the deposit particles had sintered, indicated by the necks between the particles and by the particle agglomerates. Pure K_2SO_4 has a melting point of 1069 °C and low partial pressure in the temperature range in question. Thus, pure K_2SO_4 is not expected to sinter in the temperature region experienced by the deposit. Accordingly, the sintering indicates an interaction between $PbCl_2$ and K_2SO_4.

Compared to the experiment with steel temperature at 200 °C, significantly higher amounts of Pb and Cl were observed within the deposit when the steel temperature was at 400 °C. In addition, the whole deposit displayed a sintered structure. Close to the steel surface, a compact region, enriched in both Pb and Cl was observed (Fig. 21). The compact region is similar to the region reported by Kinnunen et al. [44]. Pb and Cl were also found both above and below the compact region. The elemental ratios of the Pb-containing areas analyzed within and above the compact region corresponded to $K_3Pb_2(SO_4)_3Cl$, which is a component first suggested by Kinnunen et al. [44] in deposits consisting of K, Pb, S, and Cl. So far, the proposed $K_3Pb_2(SO_4)_3Cl$ phase has not been fully identified and corroborated to exist. However, chemical analysis of the phase in the experiments in this thesis, strongly suggests the existence of a phase similar to caracolite. In addition to the caracolite-like phase, K, Pb, and Cl, in molar ratios corresponding to the compound K_2PbCl_4, were found within the compact region, below the compact region, and on the oxide layer. Furthermore, minor amounts of KCl were found within the deposit. These findings support the formation of $K_3Pb_2(SO_4)_3Cl$, according to Reaction 5.

$$2\ PbCl_2 + 3\ K_2SO_4 \rightleftharpoons K_3Pb_2(SO_4)_3Cl + 3\ KCl \quad (5)$$

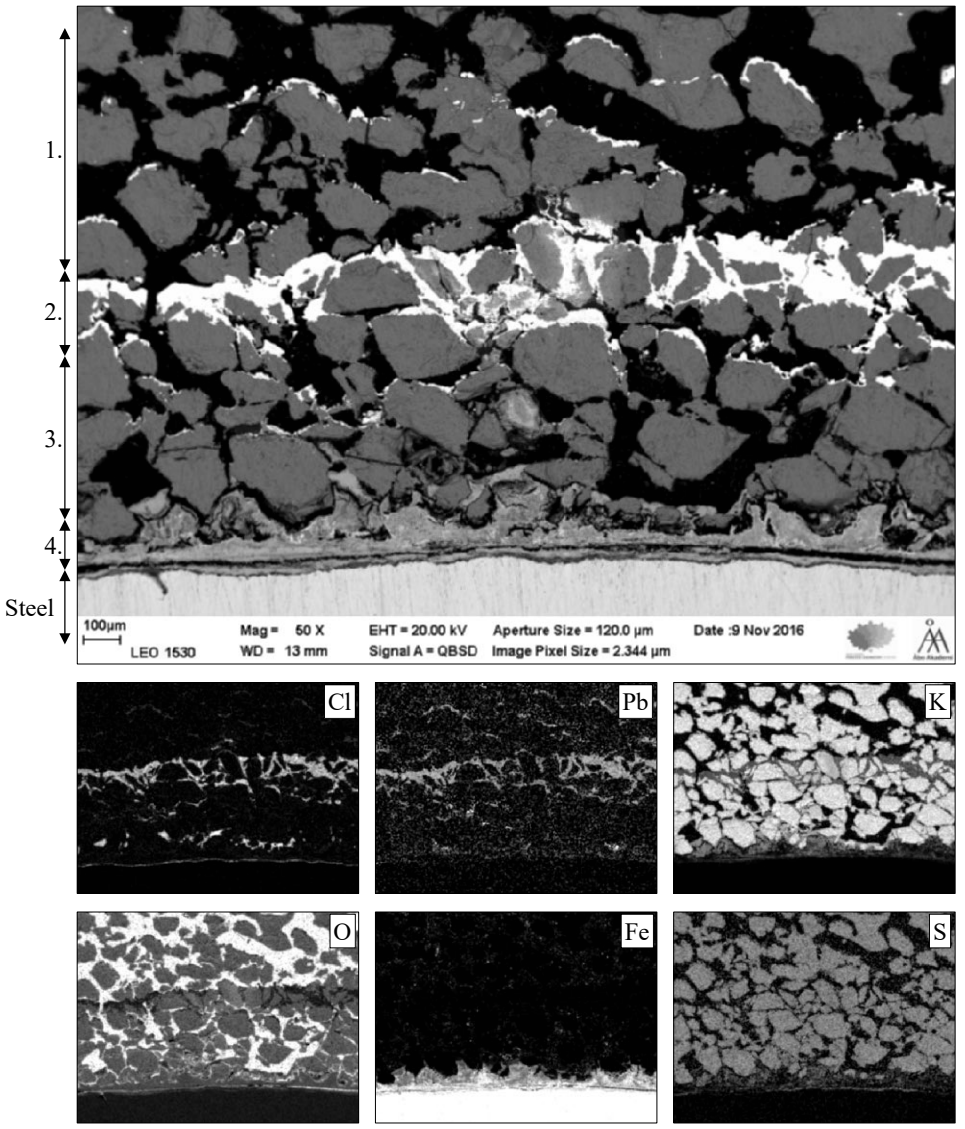

Fig. 21. SEM backscatter image and EDX elemental maps of the K_2SO_4-$PbCl_2$ cross-section with steel temperature at 400 °C. The elemental ratios suggest the following phases: (1) $K_3Pb_2(SO_4)_3Cl$ on top of K_2SO_4 particles, (2) the Pb and Cl enriched region, (3) K_2PbCl_4 and some $K_3Pb_2(SO_4)_3Cl$ on top of K_2SO_4 particles, and (4) the oxide layer. Reprinted with permission from Paper V under a CC-BY-4.0 license. Copyright © 2018 American Chemical Society.

The formation of KCl within the deposit can lead to further reactions with $PbCl_2$ to form K_2PbCl_4, which is a plausible explanation as to why only minor amounts of KCl were found while larger amounts of the proposed $K_3Pb_2(SO_4)_3Cl$ phase were observed within the deposit.

4.1.11 KCl-NaCl-$PbCl_2$

The KCl-NaCl-$PbCl_2$ system was studied, using the steel temperatures of 200 °C and 400 °C in the temperature gradient furnace for 24h (Paper V). The pre-melted and crushed KCl-NaCl salt (50:50 wt-%) and the $PbCl_2$ salt were initially applied on two separate sample rings.

Regardless of the steel temperature, K_2PbCl_4 was observed on the furnace-facing side and within the KCl-NaCl particles. The layers of K_2PbCl_4 included also some Na, in the cation ratio of 1:8:4 for Na:K:Pb. The ratio corresponds well to the SEM/EDX point analysis results by Kinnunen et al. [66] for a deposit collected from a recycled wood firing CFB boiler. In this work, KCl in the original mixture particles had reacted with $PbCl_2$. Accordingly, the original (K,Na)Cl-(Na,K)Cl matrix was substituted by a K_2PbCl_4-(Na,K)Cl matrix (Fig. 22).

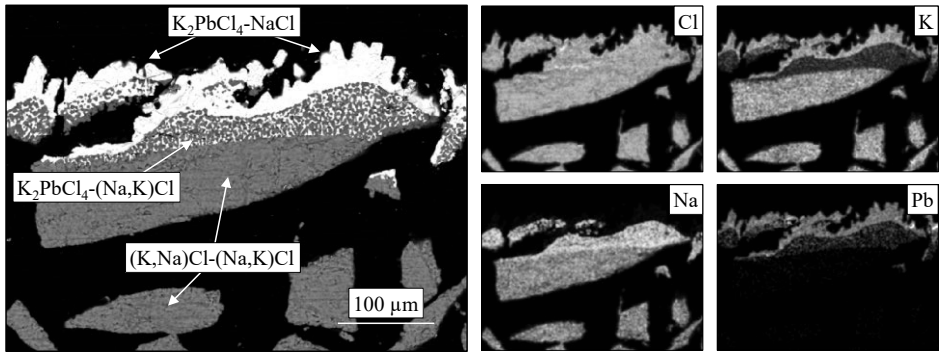

Fig. 22. SEM backscatter image and EDX maps of a salt particle in the outer part of the KCl–NaCl deposit in the 24h experiment with steel temperature at 200 °C. The image shows how the Pb-species are enriched on the furnace-facing sides of the salt particles and even penetrate into the original salt particles. Reprinted with permission from Paper V under a CC-BY-4.0 license. Copyright © 2018 American Chemical Society.

With the steel temperature at 400 °C, the salt particles were observed to have a different microstructure depending on the local temperature within the deposit. In the colder range of the deposit temperatures, the particles were more homogeneous than in the higher temperatures where the two different alkali chloride phases could be identified more clearly (Fig. 23). In the higher temperature ranges of the deposit, the furnace-facing sides were observed to be enriched in NaCl. A plausible explanation for the NaCl enrichment is the K_2PbCl_4 formation at the furnace-facing side of the particles, followed by the vaporization of KCl, $KPbCl_3$, and $PbCl_2$.

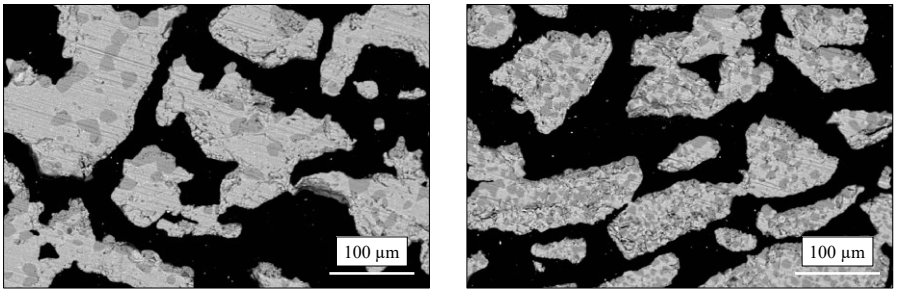

Fig. 23. SEM backscatter images of the different particle structures within the upper (left) and lower (right) porous region in the KCl-NaCl-$PbCl_2$ 24h experiment with steel temperature at 400 °C.

The experiment with steel temperature at 200 °C showed agglomeration at the upper edge of the deposit, indicating only minor amounts of $PbCl_2$ present in the deposit. This is in agreement with the reported eutectic point 379 °C for the system KCl-NaCl-$PbCl_2$ [106] and the reported solidus temperature 398 °C for the system K_2PbCl_4-KCl-NaCl [66]. Both of these temperatures are low and sintering was expected to occur if significant amounts of $PbCl_2$ had reached the target deposit. In the experiment with the steel temperature at 400 °C, the whole deposit had sintered. The upper part had a compact structure and the lower part had a network-like structure.

4.2 Deposit aging mechanisms

4.2.1 Gas phase migration

Gas phase migration of volatile species in a temperature gradient occurred with alkali chlorides (Papers I-III), alkali bromides (Paper IV) and Pb-containing chloride species (Paper V). In papers I-IV, the alkali halides were found to enrich on the furnace-facing sides of deposit particles and on the oxide/steel surface. The alkali halide layers showed typical cubic shapes of rock salt. In addition, the steel-facing sides of the deposit particles were devoid of the more volatile species (i.e. alkali halides in an original alkali halide-alkali sulfate mixture). The migration of $PbCl_2$ from the source deposit to the target deposit was also observed and is suggested to be due to gas phase migration.

The saturation pressures of alkali halide species increase with temperature, i.e. in higher temperatures, the species have higher saturation pressures (Fig. 24). In cases where solid alkali chlorides or alkali bromides are present, their surrounding gas phase is saturated with their gaseous species in equilibrium. If the system is exposed to a temperature gradient, it results in a concentration gradient in the gas phase within the deposit due to higher concentration in regions where the

temperature is higher, compared to colder regions with lower concentration. The concentration gradient leads to the diffusion of species to balance out the concentration gradient. The volatile species from the higher concentration diffuse towards the lower concentration, i.e. the diffusion occurs from the higher temperature to the lower temperature.

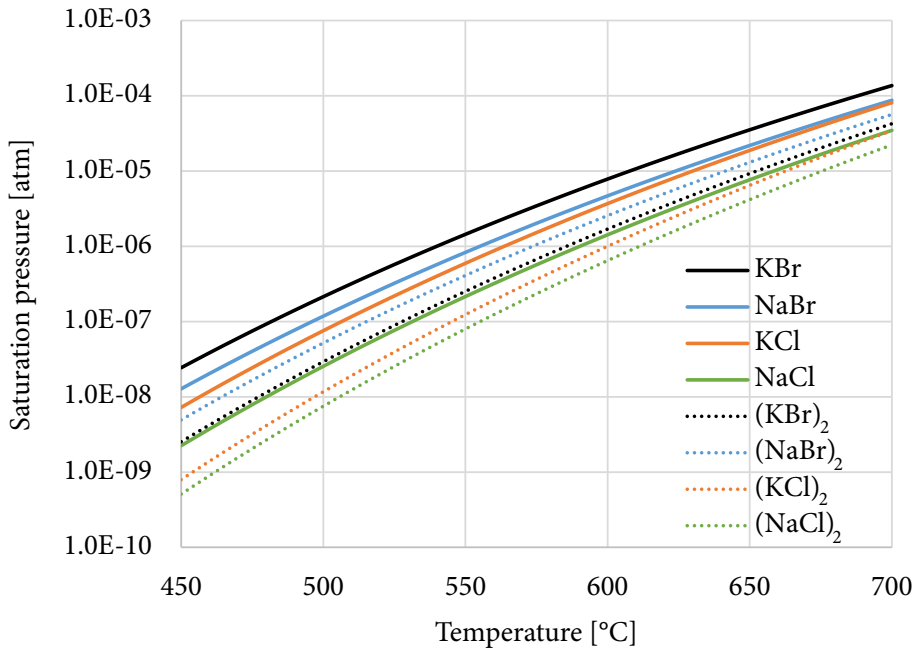

Fig. 24. Saturation pressures of alkali halides expressed as functions of temperature.

The diffusion from the higher temperature into the lower temperature results in supersaturation in the lower temperature, which results in condensation of the volatile species from the gas phase. In addition, the migration of the volatile species from the higher temperature results in partial pressures below the saturation pressure, which enables further vaporization of the volatile species from the solid phase into the gas phase. The transport mechanism is presented schematically in Fig. 25.

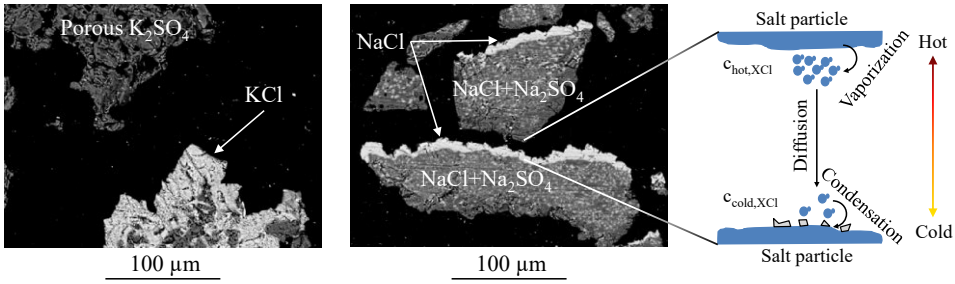

Fig. 25. SEM backscatter images of layers of alkali chlorides in subsolidus regions and a schematic illustration of the alkali halide-migration phenomenon. Reprinted with permission from Paper II. Copyright © 2017 Elsevier.

The thicknesses of the alkali halide layers, that formed in the experiments (Papers I, II and IV), were measured from the SEM backscatter electron images of the deposit-steel surface cross-sections (Papers II and IV). In addition, the distances of the individual layers from the steel surface were measured. The distances of the alkali halide layers from the steel surface were used to calculate a local temperature of each layer within the deposit during the temperature gradient exposure. Further, the bulk temperature gradient across the porous subsolidus layer was estimated. For this, the subsolidus-supersolidus interface seen in the SEM backscatter image was estimated to correspond to the solidus temperature of the salt system in question. The temperature of the steel surface was assumed to correspond to the set, or to the measured, temperature of the steel sample ring. The temperature difference between these points was divided with the distance of the points, after which a linear temperature gradient was assumed for estimating the local temperatures of the different alkali halide layers. When using this approach, the alkali halide layer thickness results could be presented as functions of temperature and compared to the modeled values (Section 3.3.2). Selected measured and modeled layer thickness results are shown in Fig. 26 (for a complete collection of layer thickness results, refer to Papers II and IV).

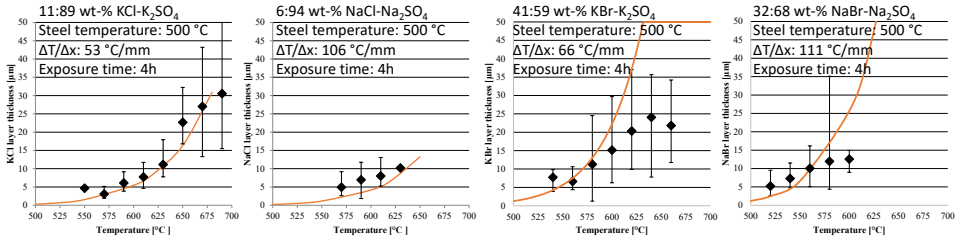

Fig. 26. Average measured alkali halide layer thicknesses (dots) together with modeled results (continuous line) as functions of local temperature within the deposit in individual experiments. The error bars show the maximum and minimum thickness values measured in the temperature interval (20 °C) in question.

The gas phase migration was observed also in the entrained flow reactor experiments (Paper III), thus verifying that the behavior seen in the laboratory experiments is not specific for the temperature gradient furnace set-up. The NaCl and KCl enrichment in the entrained flow reactor exposures occurred already after short exposure times (90 min). The experimental observations from the entrained flow reactor experiments were not compared to the modeled results, because it is challenging to discern the dynamic temperature profile of the growing deposit and to consider it in the model. In addition, some of the alkali chloride layers could have been formed due to alkali chloride deposition directly from the flue gas during the deposit build-up. However, the deposit layers were observed to be qualitatively in the same range as the temperature gradient furnace and model results.

In Paper V, $PbCl_2$ was observed to vaporize from the source deposit and condense within the target deposit. The condensation was observed to occur not only on the target deposit surface but also within the deposit closer to the steel surface. Once the source deposit of $PbCl_2$ started to deplete, the partial pressure of $PbCl_2$ decreased in the furnace, resulting in a re-vaporization of the condensed $PbCl_2$ from the target deposit.

In some experiments, the $PbCl_2$ did not condense on the surface of the target deposit but instead migrated in the gas phase towards the colder locations within the deposit and condensed there. $PbCl_2$ condensed only at sufficiently low temperatures, at which the partial pressure of $PbCl_2$ in the gas phase exceeded the saturation pressure. Therefore, the upper regions within the deposit, i.e. the regions with higher temperatures, were unaffected by the $PbCl_2$.

4.2.2 Liquid phase sintering

After almost all of the experiments, the deposits had sintered to a high degree in the supersolidus temperature range. The main mechanism resulting in the densification of the supersolidus region of the deposit was assumed to be liquid phase sintering [37]. In liquid phase sintering, the liquid phase glues the particles together. In addition, the liquid phase can move due to capillary and gravitational forces, filling the gaps and pores within the particulate microstructure. In the temperature gradient experiments, in which the liquid phase reached lower temperatures within the deposit structure, the primary crystallizing phase precipitated from the melt. This mechanism resulted in a refined structure, in which the primary crystallizing phase was enriched.

In Papers I and II, the alkali chloride-alkali sulfate deposits were observed to sinter differently depending on the ratio of the components of the mixture. Two different types of supersolidus regions were observed: a network-like structure and a compact structure. The different types of supersolidus regions were created depending on the amount of melt present in the deposit. With a higher amount of melt, the deposit's supersolidus structure becomes compact with only small round voids within it. The alkali bromide-alkali sulfate mixtures studied in Paper IV also had compact supersolidus structures, post-temperature-gradient-exposure. The alkali bromide-alkali sulfate mixtures formed 60 wt-% melt at the solidus temperature, which can be considered as a high amount. With a low amount of melt, the deposit structure develops into a network-like structure, where the original particles are bridged together. The different types of supersolidus structures are shown in Fig. 27.

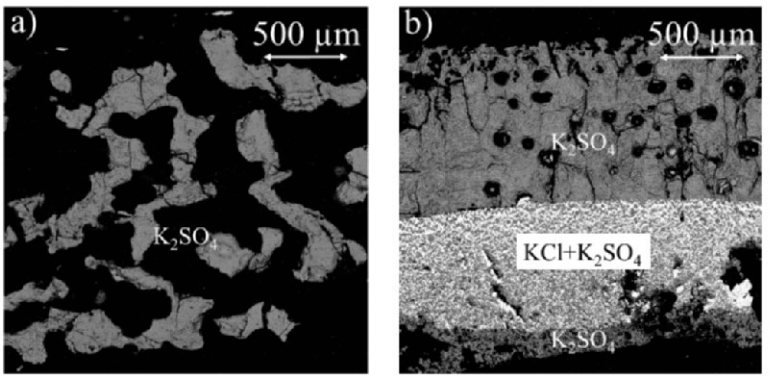

Fig. 27. SEM backscatter images of supersolidus regions of a) K_2SO_4 network structure and b) compact structure of K_2SO_4 with spherical voids. Adapted from Paper II.

The deposits observed in Paper V, containing alkali salts and relatively low amounts of $PbCl_2$, all except the KCl-NaCl mixture, had a network-like structure. Due to the fact that $PbCl_2$ was introduced into the target deposit via the gas phase, the amount of $PbCl_2$ in the target deposit was relatively low. The low $PbCl_2$ amount in the deposit resulted in a low amount of melt and led consequently into a network-like morphology, not a compact morphology seen for the bulk of the alkali halide-alkali sulfate deposits. The experiment where the target deposit was a KCl-NaCl (50:50 wt-%) mixture with a solidus temperature of 657 °C, i.e. the solidus temperature was below the furnace temperature, compact morphology of the deposit was observed in the outer deposit region.

In the entrained flow reactor experiments (Paper III), the same KCl-K_2SO_4 mixture that had in the temperature gradient furnace experiments resulted in a network-like morphology resulted in a compact morphology. In the entrained flow reactor, the salt particles were partially molten when they hit the probe and there was a continuous feed of more partially molten particles to the deposit. The melt fraction of the hot particles entrained in the flue gas was likely to be somewhat higher than in the particles in a stagnant particle bed, and it is likely to be the reason for the difference between the results from the different experimental set-ups.

In deposits with compact supersolidus region, the region often contained spherical voids. The presence of the voids is a clear indication of the liquid phase sintering phenomenon, occurring by a pore-filling mechanism. The formation of the spherical voids in the supersolidus region is similar to effects reported to occur in liquid phase sintering when inert gas is entrapped within the microstructure [37, 108]. According to the pore-filling theory [108], the isolated pores are filled with liquid and grain growth into the pores occurs. The small pores are eliminated first, leading to a situation where the mean pore size is increased during the liquid phase sintering. In case of the temperature gradient experiments, the spherical voids are most likely air-pockets originally present between the particles in the deposit that were trapped in the new solid microstructure.

The difference to the temperature gradient experiments is that in traditional isothermal liquid phase sintering, the amount of liquid that is present is fairly stable, while in the temperature gradient experiments the liquid phase decreases as pore-filling takes place, due to the movement of the liquid phase. As the amount of liquid phase decreases, so does the liquid phase sintering rate, which partly explains why even after 72h exposure there are spherical voids present in the compact supersolidus structure. The decrease in the amount of the liquid phase is due to a combination of vaporization of volatile species into the furnace, movement of the liquid phase towards the lower temperature due to capillary and

gravitational forces, and temperature gradient zone melting, which is discussed in more detail in Section 4.2.3.

4.2.3 Temperature gradient zone melting

The binary alkali chloride-alkali sulfate and alkali bromide-alkali sulfate systems displayed clear and sharp interfaces between the eutectic region and the upper supersolidus region. In addition, the upper supersolidus region was often observed depleted of the minor component, i.e. not the primary crystallizing phase. Parts of the depletion can be accounted to be due to the liquid phase sintering and the flow of the liquid phase towards the steel surface. Regardless, it is unlikely that the refinement of the primary crystallizing phase is purely due to the liquid phase sintering. This is clearly shown in the shorter experiments, where eutectic pockets were observed within the dense upper deposit structure.

Temperature gradient zone melting is suggested to be responsible for the refinement of the primary crystallizing phase in the supersolidus temperatures and for the clear interface between the eutectic region and the upper supersolidus region.

The temperature gradient zone melting phenomenon [56-58, 109] is described schematically in Fig. 28. The liquid phase composition of a binary mixture with eutectic melting behavior depends on the local temperature. Therefore, the liquid phase in a temperature gradient experiences a concentration gradient in the direction of the temperature gradient. In the case of alkali chloride-alkali sulfate and alkali bromide-alkali sulfate mixtures, the melt composition follows the liquidus line of the binary phase diagram of the salt system in question. Due to the concentration gradient across the melt phase, diffusion occurs to balance out the concentration difference. In the example case of Fig. 28, the alkali bromide migrates towards the hotter temperature. The migration shifts the composition at the colder temperature towards the alkali sulfate, resulting in the crystallization of alkali sulfates from the melt. The increased concentration of alkali bromides in the higher temperature range enables more of the alkali sulfate to be incorporated into the melt phase. The overall result is that the alkali bromides, and with them, the molten phase, move towards the hotter temperature. At the top of the deposit, the alkali bromides vaporize into the furnace, leaving behind a refined alkali sulfate structure.

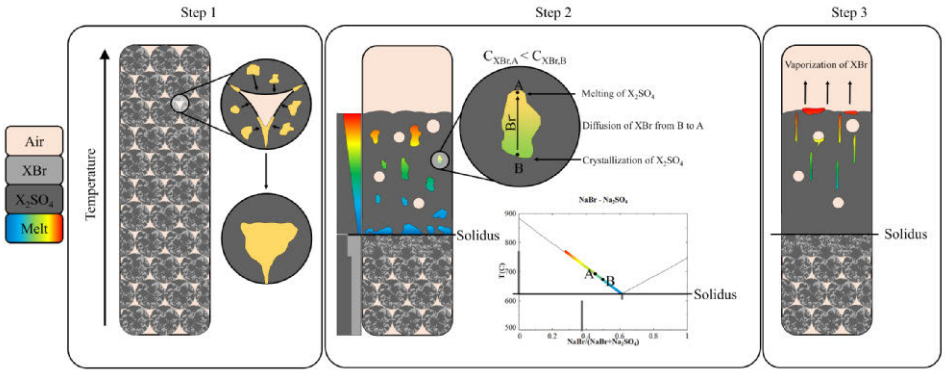

Fig. 28. Schematic image explaining the deposit morphology and chemistry evolution due to liquid phase sintering and temperature gradient zone melting phenomena. Step 1 shows the initial deposit densification by liquid phase sintering. Step 2 shows how the temperature gradient zone melting induces alkali bromide-migration toward the outer surface of the deposit. Step 3 shows a refined alkali sulfate structure and the sharp interface between the eutectic layer and the refined alkali sulfate. Reprinted with permission from Paper IV under a CC-BY-4.0 license. Copyright © 2019 American Chemical Society.

In a number of alkali chloride-alkali sulfate experiments, lamellar solidification patterns were observed in the upper part of the supersolidus region. Kerridge et al. [105] reported that the formation of the lamellar and labyrinth solidification structures in binary eutectic systems is dependent on the quenching rate during the solidification. Lamellar structures are formed with a large difference between the melt and quench temperatures, which corresponds to the temperature conditions in the upper supersolidus region during quenching. In addition, Perrut et al. [110] reported a connection between the lamellar solidification patterns and transverse temperature gradients and they noted that the labyrinth pattern formation is slow, which supports the findings of Kerridge et al. [105].

In the temperature gradient experiments, the microstructure of the eutectic layer was always a labyrinth type, which would indicate that the solidification of the region was slow. The fact that the labyrinth structure is formed slowly implies that the eutectic layer structure was formed during the experiments. In addition, the sharp interfaces observed between the eutectic region and the upper supersolidus region support this claim.

The temperature gradient zone melting can also occur for more complicated systems than binary systems. In the entrained flow reactor experiments (Paper III), where NaCl-Na_2SO_4 and KCl-K_2SO_4 mixtures were fed into the reactor sequentially, the melt pockets within the refined alkali sulfate structure were

observed to contain a mixture of K-Na-Cl-SO_4. When considering the melting characteristics of the mixture, the composition and the temperature affect the melting behavior. To discern the exact local composition of the supersolidus region in the entrained flow reactor experiments is challenging because the two mixtures were introduced into the reactor sequentially. When the exact local composition is unknown, also the liquid phase composition in a given temperature remains unknown. However, regardless of the composition, the K-Na-Cl-SO_4 system is such that in a temperature gradient, there exists a concentration gradient across the melt. Similar to a binary mixture, diffusion occurs to balance out the concentration gradient in the melt phase. The diffusion of species results in a change in the melt composition in the different locations, resulting in precipitation at the lower temperature and further melting at a higher temperature. Differing from the binary mixture, the precipitating phase also depends on the original deposit composition and the local temperature. In addition, the new local composition in a hotter location also results in new local melting characteristics, which makes the system highly dynamic.

An even more complicated case of temperature gradient zone melting was observed in Paper IV, where corrosion products were found at the top of the alkali bromide-alkali sulfate deposits. With the inclusion of corrosion products (e.g., $FeBr_2$, $FeBr_3$, $CrBr_3$, and metal oxides), the melting properties and, consequently, the prediction of the phenomenon becomes more complicated. In addition, the corrosion products can undergo chemical reactions (e.g. oxidation at high enough O_2 partial pressures), altering the composition and as a result making the system even more complicated. Similar results have been earlier reported by Lagerbom et al. [48] and by Lindberg et al. [111].

The ahead mentioned properties of multicomponent systems result in a highly dynamic system, which is hard to describe quantitatively. However, qualitatively, it is clear that the temperature gradient zone melting phenomenon results in species migration also in the more complicated systems, supported by the experimental observations from the Papers III and IV, and by the results of others [48].

4.3 Corrosion mechanisms

In this section, the corrosion results from the temperature gradient furnace measurements are summarized.

4.3.1 Alkali chloride-induced corrosion

Alkali chloride-induced corrosion occurred in all of the experiments with alkali chloride-alkali sulfate mixtures exposed to temperatures >400 °C (Papers I and II). The corrosion rate and mechanisms for 10CrMo9-10 were observed to be qualitatively similar to those reported by others [112].

The exposure of 10CrMo9-10 to KCl for 24h, with steel temperature at 400 °C, resulted in an oxide layer thickness, which was measurable (~5 μm). The oxide layer was compact and it consisted mainly of iron oxide. With steel temperature at 500 °C, the oxide layer was noticeably thicker (~25 μm). The amount of KCl in the salt mixture was not found to affect the corrosion in a significant way; this is probably because even the lowest KCl amount in the salt mixture was relatively high and even low concentrations of KCl have been shown to be corrosive [83].

Next to the steel surface, indications of $FeCl_2$ were observed in some of the experiments. Moving towards the flue gas, the next region was typically a Cr rich layer. The Cr rich layer was followed by a compact iron oxide layer, which by Enestam et al. [112] was named Type 1 oxide. In some of the experiments, the Type 1 oxide was followed by a more porous oxide, similar to the Type 2 oxide observed by Enestam et al. [112]. In addition, the porous Type 2 oxide grew around and within the salt particles. When the oxide was growing inside particles, it was within alkali sulfate particles but together with alkali chlorides.

Corrosion results with NaCl were similar to those with KCl. The main difference was that exposure to NaCl resulted in a higher amount of porous Type 2 oxide. Enestam et al. [112] reported the Type 2 oxide formation to occur with the material temperature at 500 °C with NaCl and at 525 °C with KCl, which is within the same temperature region as the corrosion observed in the temperature gradient furnace experiments in this work.

Alkali chloride-induced corrosion was observed to be highly dependent on the temperature of the steel. With steel temperature at 300 °C, no corrosion was observed. With steel temperature at 400 °C, the oxide layer thickness was measured to be ~5 μm after 24h exposure. The steel temperature of 500 °C induced fast corrosion rates (~25μm/24h) with all deposit compositions.

4.3.2 Alkali bromide-induced corrosion

In the alkali bromide-alkali sulfate experiments (Paper IV), significant corrosion was observed for both the P235GH and 10CrMo9-10 steel grades, with steel temperature at ~500 °C. The typical corrosion of P235GH is shown in Fig. 29, with the steel situated at the bottom of the image. On the steel surface, a presence of iron bromide species was indicated in several experiments. This observation is also supported by results reported by others [75, 76]. Moving toward the flue gas, the following layer is a dense oxide layer consisting of iron oxide (P235GH) or a mixture of iron and chromium oxides (10CrMo9-10). Above the dense oxide layer is a layer with iron oxide mixed with alkali bromides.

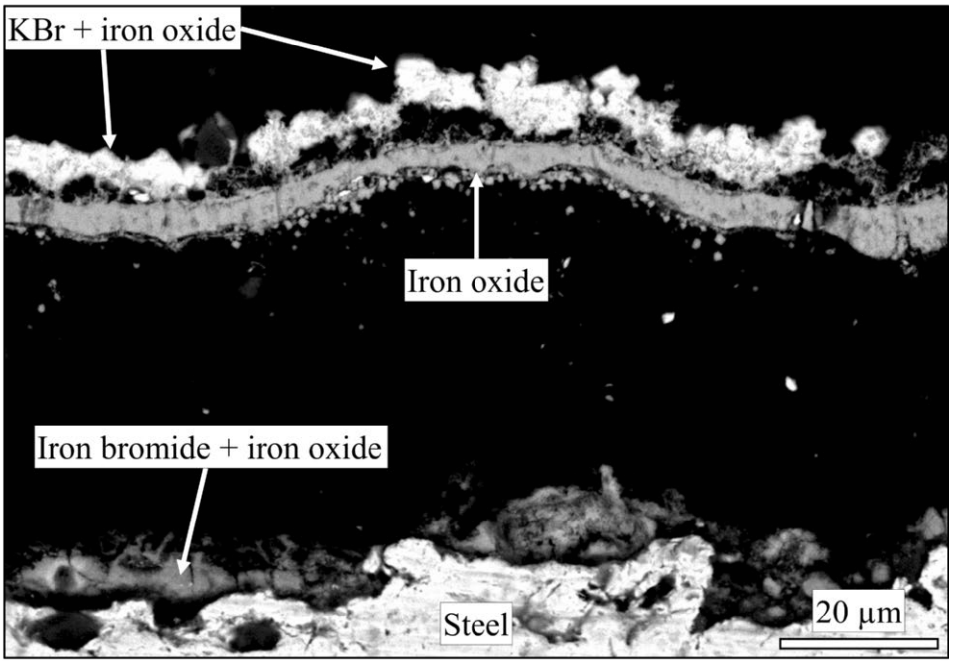

Fig. 29. Corrosion layer of P235GH steel after 4h of exposure to KBr-K_2SO_4. Reprinted with permission from Paper IV under a CC-BY-4.0 license. Copyright © 2019 American Chemical Society.

In an experiment with NaBr-Na_2SO_4 on the P235GH steel, a porous oxide layer grew around the salt grains, which were in contact with the steel surface. The porous oxide layer was found above the dense oxide layer. A similar Type 2 oxide layer also formed in some of the alkali chloride experiments. Similar behavior has been observed before by others, in experiments with NaCl, KCl [112], and KBr [73]. The Type 2 oxide layer formation could not be seen in experiments with the KBr containing deposits. With alkali chlorides, the Type 2 oxide formation has been reported to occur at a lower temperature with NaCl than with KCl, and a

similar difference is possible also for alkali bromides. However, Wu et al. [73] reported similar porous oxide formation with 10CrMo9-10 steel exposed to KBr at 500 °C and above after a 168h exposure. The difference to the temperature gradient furnace results could be due to the large difference in exposure time (8h vs 168h).

4.3.3 Lead chloride-induced corrosion

The corrosion induced by Pb-containing species was studied in Paper V and was observed to be dependent on whether the steel was in contact with pure $PbCl_2$ or some other Pb-containing species. The corrosion layer thickness results are summarized in Fig. 30. The steel material studied was P235GH and the material temperature was 400 °C. In general, the corrosion layer thickness was thicker for deposits, which interacted less with $PbCl_2$. SiO_2 did not interact with the $PbCl_2$ and resulted in the thickest oxide layer out of all the deposit materials tested together with $PbCl_2$.

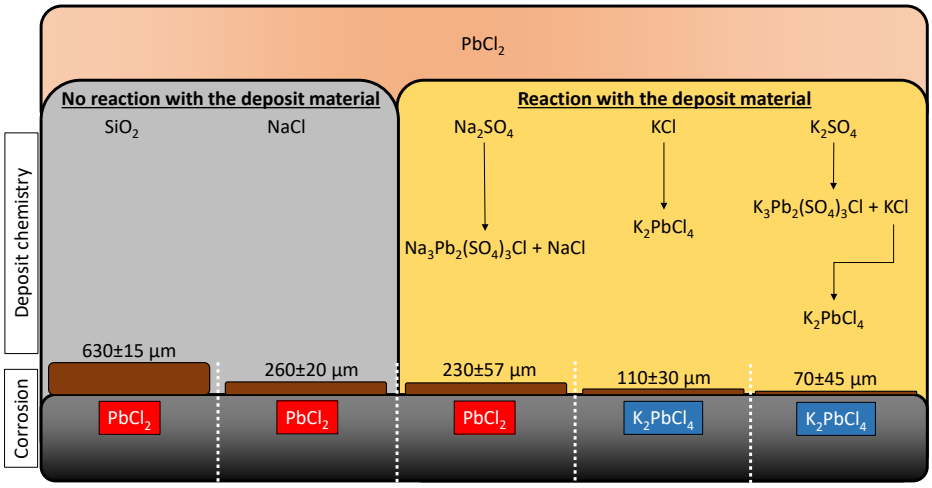

Fig. 30. Summary of the corrosion results in $PbCl_2$ experiments, showing the reactions of the deposit material with $PbCl_2$, the oxide layer thickness results after 24h exposure and the corrosive Pb-species found at and within the oxide layer. Adapted from Paper V.

NaCl forms a eutectic melt system with $PbCl_2$ but does not react to new compounds. The oxide layer below the NaCl deposit was similar to the one with SiO_2. The thinner layer implies that the corrosion mechanisms are the same; only the rate and possibly the initiation were slower.

Na_2SO_4 melted together with $PbCl_2$ and was also observed to react and form new compounds within the deposit. The formation of $Na_3Pb_2(SO_4)_3Cl$ was suggested by the elemental analysis of the phases. The analysis of the oxide layer in the Na_2SO_4

experiment implied that although $Na_3Pb_2(SO_4)_3Cl$ was found on top of the oxide layer, the Pb-species most likely responsible for the observed corrosion was $PbCl_2$ that was identified within the oxide layer. As the oxide layer composition below the Na_2SO_4 deposit was similar to the oxide layers below the SiO_2 and NaCl deposits, the corrosion mechanism is expected to be the same for all these cases.

The KCl and K_2SO_4 deposits resulted in similar oxide layers. In neither case, $PbCl_2$ was identified on or within the oxide layer; instead, K_2PbCl_4 was observed both on and within the oxide layer. With K_2SO_4, the oxide layer was somewhat thinner than with KCl, which could be due to the formation of the $K_3Pb_2(SO_4)_3Cl$, which binds both Pb and Cl into the new compound. In addition, the reaction yields KCl, which can further react with $PbCl_2$ to form K_2PbCl_4. $K_3Pb_2(SO_4)_3Cl$ was not observed on or within the oxide layer; instead, K_2PbCl_4 was suggested to be the corrosive species.

The KCl-NaCl mixture resulted in the thinnest oxide layer (50±13 μm). $PbCl_2$ had reacted to K_2PbCl_4. In addition, the K_2PbCl_4 was incorporated in the salt matrix together with NaCl, thus inhibiting the vaporization, and thereby resulting in a slower migration rate to the steel.

The results indicate that $PbCl_2$ is a more corrosive component than the Pb-bearing compounds $Na_3Pb_2(SO_4)_3Cl$, K_2PbCl_4, or $K_3Pb_2(SO_4)_3Cl$. In all of the experiments, there were strong indications of $FeCl_2$ being present at the steel surface.

4.4 Implications for boiler applications

The synthetic deposits studied in this thesis differ from real boiler deposits in a number of ways. In Papers I, II, IV, and V, the deposit material was applied on top of a probe in powder form, with a particle size of 53-250 μm. The deposit structure and composition were therefore homogeneous at the start of the temperature gradient exposure. The deposit build-up in boilers occurs by a number of different mechanisms [2, 30], and the deposit aging occurs simultaneously. The dynamic build-up leads to more heterogeneous deposits, already at the build-up stage. However, in the present work, even the originally homogeneous particle deposits were observed to form heterogeneous layered structures and species enrichment due to the temperature gradient exposure.

The effect of the simultaneous deposit build-up and aging was considered in the entrained flow reactor experiments (Paper III). The build-up had some effect on the deposit structure, but the overall aging mechanisms, and the structure and composition of the deposit were observed similar to the corresponding temperature gradient furnace experiments, in which there were no build-up

effects. This suggests that the deposit aging mechanisms significantly affect the deposit structure.

Compared to actual boiler ash deposits, the deposit materials studied in this thesis were simplified salt systems with only a handful of different components present in the deposit. As mentioned in Section 2.2, the ash deposits in biomass and waste-fired boiler units can include several different components, and the chemistry is often more complicated than in the synthetic deposits. The ash deposits in black liquor recovery boilers are somewhat simpler compared to other biomass and waste-fired boiler deposits. Black liquor recovery boiler deposits mainly consist of alkali sulfates, sulfides, carbonates, and chlorides. In addition, some of the synthetic alkali halide-alkali sulfate compositions studied in this thesis were relatively high in alkali halides, compared to deposits in boilers. That being said, the deposit aging phenomena observed in the synthetic deposits are likely to also occur in a boiler deposit, although at a different rate.

The gas phase migration of volatile species towards the colder temperature can occur if the deposit is sufficiently porous. Although boiler deposits have been shown to be porous [59, 113, 114], the size and amount of the pores differ depending on a number of factors, e.g. the fuel, the boiler type, and the temperature profile. The pore size will most likely affect the migration rate as it affects the available space for the condensation and it affects the temperature profile [53, 54, 111]. In addition to the pore size, other factors are likely to affect or limit the gas phase migration rate of volatile species within a boiler deposit. One prominent factor is the activity of the migrating species within the deposit. With several elements present, the volatile species are likely to be incorporated into a solid or liquid solution, which will lower their partial pressures, compared to a case where a pure solid phase is present. For example, in black liquor recovery boiler deposits, the alkali chlorides can be incorporated in a KCl-NaCl solid solution or in a melt phase, resulting in lower partial pressures of alkali chlorides compared to when a pure solid alkali chloride phase is present.

The gas phase migration was studied in detail with alkali chlorides and alkali bromides. The results from Paper V indicate that also $PbCl_2$ enriches in colder temperatures due to vaporization-condensation mechanisms. It seems reasonable to expect that the mechanism also occurs with other volatile species. In general, it could be possible to utilize the model developed in this work to obtain a first estimate on the migration rate of volatile species other than those studied in this work. As input to the model, vapor pressures of the volatile species in the desired temperature region should be known.

The liquid phase sintering requires a melt phase and pores to be present to occur. Liquid phase sintering is likely to occur in the boiler deposits, as liquid and viscous melt phases are likely to be present in boiler deposits [40, 42, 43, 49, 64]. The sintering tendency increases with an increasing melt amount and with decreasing particle size [37, 111]. Depending on the type of deposit, the amount of melt in the deposit can vary from high (e.g. in a recovery boiler deposit [29, 33, 64]) to low. The results of this thesis show that liquid phase sintering occurs at a fast pace for synthetic deposits. Even if the sintering would occur at a considerably slower pace in the boiler deposits, the deposits have significantly longer time to mature. In addition, the results from the sequential feeding of NaCl-Na_2SO_4 and KCl-K_2SO_4 systems into the entrained flow reactor (Paper III) show that changes in the fuel quality during boiler operation can also affect mature deposits. A fluxing agent can significantly alter the melting properties of an ash deposit and can result in deposit densification and/or species enrichment.

The amount of melt present in the deposit has been shown to have direct consequences for the deposit adhesion properties [42]. Laxminarayan et al. [43] showed that synthetic deposits that experience liquid phase sintering and gas phase migration of species towards the steel, attach harder to the heat exchanger surfaces. In addition to the deposit removability, the sintering and densification of the deposit structure affect the thermal conductivity of the deposits [45]. Laxminarayan et al. [43] studied deposits containing KCl-K_2SO_4, KCl-K_2SO_4-CaO, KCl-K_2SO_4-$CaSO_4$, KCl-K_2SO_4-$K_2Si_4O_9$, and collected ash from a straw-fired boiler. Although Laxminarayan et al. mainly studied ideal deposit systems in a laboratory environment; their findings imply that the observed aging phenomena are general in nature. In addition, the experiments they conducted using the collected ash sample yielded similar results as their synthetic KCl-K_2SO_4 deposit.

Temperature gradient zone melting requires a melt phase to be present to occur. In addition, the melt needs to be surrounded by its primary crystallizing phase, and the solid phase should preferably be continuous. These conditions are not very likely to occur in a boiler deposit, but there is a possibility that e.g. selected black liquor recovery boiler deposits could fulfill these conditions. The industrial relevance of the temperature gradient zone melting mechanism in boiler deposits remains an unsolved issue and further research on the subject is needed. The temperature gradient zone melting mechanism could be favorable if it results in a migration of corrosive elements away from the steel surface, but it could also induce breakdown and diminishing of the protective oxide layer. There are other reports indicating temperature gradient zone melting occurring for corrosion products [48, 111] but the implications for boilers are still unclear. In addition, the

temperature gradient zone melting mechanism could occur at the corrosion front affecting the corrosion mechanism.

Corrosion of heat exchanger tubes is likely to be affected by the changes in the local deposit composition. Molten salts that contain alkali halides are known to induce rapid corrosion [82-84, 115, 116]. Alkali halides and heavy metal halides are also known to induce heavy corrosion in subsolidus conditions [83, 115, 117]. According to the observations made in this thesis, alkali halides and heavy metal halides are available for enrichment in lower temperatures within deposits, possibly enriching directly on top of heat exchanger surfaces.

Despite the differences between the synthetic deposits and the boiler deposits, the deposit morphologies observed in straw-fired boilers [43, 47, 59-61] are similar to the KCl-K_2SO_4 deposits observed in the temperature gradient furnace experiments. The reason being that the ash composition in straw is high in KCl and K_2SO_4. The results of this thesis contribute to the understanding of the formation mechanism of KCl enriched layers within ash deposits in straw-fired boilers.

Alkali bromides have been observed to enrich in colder temperatures in waterwall deposits. The enrichment of Br reported by Vainikka et al. [69] could also be due to the initial deposition during deposit build-up. However, in the light of the results of this thesis, the enrichment is likely to be partly due to the intradeposit vaporization-condensation mechanism and/or the liquid phase sintering induced alkali bromide enrichment.

Reeve et al. [24] reported deposit measurements conducted in a black liquor recovery boiler. Their results show that there is an increase of both K and Cl content in the colder parts of the deposits. Similar results were observed by Costa and Paoliello [64] in collected superheater deposits. The deposit aging effects could explain the behavior. Costa and Paoliello even note that their results could be due to enrichment effects and that the enrichment of K and Cl results in a lower first melting temperature of the deposit, compared to the electrostatic precipitator ash they collected from the boiler.

For waste-fired units, it is interesting to observe that K-Pb-Cl species seem to be less corrosive than pure $PbCl_2$. In fact, the behavior implies that the corrosive behavior can be related to the stability of Cl-containing species, i.e. how easily the Cl-containing component yields Cl, either as Cl^- or as Cl_2 for the corrosion reaction. In addition, melt formation increases the corrosion rate. The K_2PbCl_4-KCl-NaCl system has been predicted to have a solidus temperature of 398 °C [66], which is lower than the steel temperature (400 °C) in the experiments in question. However, the solidus predictions for the K_2PbCl_4–KPb_2Cl_5–NaCl by Kinnunen et

al. [66] is ~15 °C lower than the reported experimental values [106, 118]. It is possible that also the K_2PbCl_4-KCl-NaCl system solidus prediction is lower than the actual solidus temperature, which would mean that no molten salt is in contact with the steel surface at 400 °C. However, it should be noted that in laboratory conditions the corrosion rates induced by both the $PbCl_2$ and the K_2PbCl_4 with P235GH steel at 400 °C are still extremely high (>50 μm/24h).

5 CONCLUSIONS

In this work, the effects of temperature gradients in ash deposits were studied in a laboratory-scale temperature gradient furnace and in an entrained flow reactor. The objective of this work is to further the understanding of the chemical and physical phenomena occurring in steam boiler deposits due to temperature gradients. The work concentrated on ideal deposits consisting of alkali salts. In addition, the behavior and interactions of $PbCl_2$ with alkali salts in temperature gradients were studied. The results from the laboratory experiments were compared to boiler deposits and to the existing knowledge of boiler deposits. The following phenomena were identified to be relevant for deposit aging:

1) Liquid phase sintering;

2) Temperature gradient zone melting in the sintered part of the deposit;

3) Vaporization-condensation in the porous part of the deposit.

In addition to the experimental work, a mathematical model was developed to predict the intradeposit alkali halide enrichment due to vaporization-condensation.

The main morphological changes in the deposits exposed to temperature gradients were observed to occur due to the local melting of the deposit. Formation of melt induces liquid phase sintering in initially porous deposits. The sintering occurs mainly by a pore-filling mechanism, resulting in dense deposit structures. In addition to structural changes, the local deposit composition was observed to be affected by the liquid phase sintering mechanism. The components incorporated in the melt phase enriched in the location with the temperature corresponding to the solidus temperature of the composition in question. This behavior indicates a possibility for the enrichment of corrosive species in the solidus temperature region. In addition, changes in the local composition can also affect the melting behavior, e.g. lowering the solidus temperature in a given location within a deposit.

Temperature gradient zone melting was observed to affect the deposit chemistry in the supersolidus region of the deposits. In a solid-liquid system where the liquid phase composition is a function of the temperature, e.g. eutectic binary system, which is subjected to a temperature gradient, the liquid phase experiences a concentration gradient. The concentration gradient results in species migration and eventually in the movement of the liquid phase towards the hotter temperature. Temperature gradient zone melting was observed to affect the deposit chemistry in both the binary (e.g. $NaCl$-Na_2SO_4) and higher-order (e.g. KCl-$NaCl$-K_2SO_4-Na_2SO_4) systems. In addition to deposit chemistry, temperature

gradient zone melting was indicated to also affect the corrosion products. The effect of temperature gradient zone melting on high-temperature corrosion remains an unsolved issue and therefore further research is needed to assess the effect.

Vaporization-condensation of volatile species affected the local composition of the porous ash deposits. Alkali chlorides and bromides migrate towards the colder temperatures within synthetic ash deposits due to temperature gradient induced concentration diffusion. The diffusion process was successfully modeled using prime principles, confirming vaporization-condensation as the relevant mechanism. In boiler deposits, the intradeposit migration has the potential to affect the local deposit composition and lead to enrichment of volatile corrosive species on heat exchanger surfaces, enhancing the corrosion rate of the steel.

In addition to the intradeposit enrichment, gaseous $PbCl_2$ condensed within synthetic ash deposits from the hot furnace air when the sufficiently low local temperature was reached. $PbCl_2$ interacted with the alkali salts within the synthetic ash deposits. With NaCl, the interaction was a formation of melt, while with Na_2SO_4, K_2SO_4, and KCl, $PbCl_2$ was observed to also react and form new compounds (K_2PbCl_4, $K_3Pb_2(SO_4)_3Cl$ and $Na_3Pb_2(SO_4)_3Cl$). The new compounds were observed to induce slower corrosion in the carbon steel material than the original $PbCl_2$.

The results obtained from the laboratory scale temperature gradient furnace method were observed to be qualitatively comparable to the results from the entrained flow reactor and from industrial boilers. The method is shown to be a working practical tool for further studies, both on the deposit chemistry and on the deposit induced high-temperature corrosion.

6 FUTURE WORK

The deposit aging mechanisms were studied in relatively simple synthetic salt deposits. With a better understanding of the governing mechanisms, a next step could be to study more complicated and realistic deposit compositions, such as:

- Actual ash collected from boilers and/or ash acquired from ashing of fuels could be aged with the temperature gradient furnace set-up.
- The corrosivity and interactions of $ZnCl_2$ with alkali salts and with $PbCl_2$ in a temperature gradient could be interesting to study from the waste-firing point of view as high amounts of Zn have been reported to be present in waste-firing environments.
- Short and long-term deposit probe measurements in boiler environments to evaluate the deposit aging mechanisms in a realistic environment.

The temperature gradient zone melting phenomenon was observed qualitatively but it was not yet modeled. A next step could be to model the phenomenon by coupling computational fluid dynamics and thermodynamic calculations. In order to validate the modeling results, additional well-controlled temperature gradient experiments should be conducted. Especially the migration of corrosion products (metal chlorides) in partially molten deposits and the implications to high-temperature corrosion of steel would be of interest.

Limiting factors that affect the vaporization-condensation mechanism of alkali halides (and other volatile species) should be assessed. For example, the volatile species might be a part of a solid or liquid solution, resulting in a lower partial pressure compared to when pure solids are present. In addition, in realistic applications, the amount of volatile species is likely lower than in the synthetic deposits described in this work, which translates to mass limitations, which should also be included in the updated versions of the alkali halide-migration model.

REFERENCES

[1] EU, 2030 climate & energy framework, https://ec.europa.eu/clima/policies/strategies/2030_en. 2014 (accessed 30.4.2019).
[2] L.L. Baxter, Ash Deposition during Biomass and Coal Combustion: A Mechanistic Approach, Biomass and Bioenergy 4(2) (1993) 85-102.
[3] J.-M. Brossard, F. Lebel, C. Rapin, J.-F. Mareche, X. Chaucherie, F. Nicol, M. Vilasi, Lab-scale study on fireside superheaters corrosion in MSWI plants, NAWTEC17: Proceedings of the 17th annual North American waste to energy conference, Chantilly, Virginia, USA, 2009, pp. 63-69.
[4] J. Li, A. Brzdekiewicz, W. Yang, W. Blasiak, Co-firing based on biomass torrefaction in a pulverized coal boiler with aim of 100% fuel switching, Applied Energy 99 (2012) 344-354.
[5] T.N. Adams, General Characteristics of Kraft Black Liquor Recovery Boilers, in: T.N. Adams (Ed.), Kraft Recovery Boilers, TAPPI Press, New York, NY, U.S.A., 1997, pp. 3-40.
[6] W.J. Frederick, Black Liquor Properties, in: T.N. Adams (Ed.), Kraft Recovery Boilers, TAPPI Press, New York, NY, U.S.A., 1997, pp. 61-99.
[7] T.N. Adams, A.K. Jones, Recovery Boiler Design and Control, in: T.N. Adams (Ed.), Kraft Recovery Boilers, TAPPI Press, New York, NY, U.S.A., 1997, pp. 349-372.
[8] H. Tran, Upper Furnace Deposition and Plugging, in: T.N. Adams (Ed.), Kraft Recovery Boilers, TAPPI Press, New York, NY, U.S.A., 1997, pp. 247-284.
[9] M. Zevenhoven, P. Yrjas, B.-J. Skrifvars, M. Hupa, Characterization of Ash-Forming Matter in Various Solid Fuels by Selective Leaching and Its Implications for Fluidized-Bed Combustion, Energy & Fuels 26(10) (2012) 6366-6386.
[10] S.V. Vassilev, D. Baxter, L.K. Andersen, C.G. Vassileva, An overview of the chemical composition of biomass, Fuel 89(5) (2010) 913-933.
[11] M. Zevenhoven, P. Yrjas, M. Hupa, Ash-forming matter and ash-related problems, in: M. Lackner, F. Winter, A.K. Agarwal (Eds.), Handbook of Combustion, Wiley-VCH Verlag GmbH & Co. KGaA, Weinheim, Germany, 2010, pp. 493-531.
[12] Y. Liu, W. Fan, X. Wu, X. Zhang, Chlorine-Induced High-Temperature Corrosion of Boiler Steels Combusting Sha Erhu Coal Compared to Biomass, Energy & Fuels 32(4) (2018) 4237-4247.
[13] P. Vainikka, M. Hupa, Review on bromine in solid fuels. Part 1: Natural occurrence, Fuel 95(1) (2012) 1-14.

[14] P. Vainikka, M. Hupa, Review on bromine in solid fuels - Part 2: Anthropogenic occurrence, Fuel 94(1) (2012) 34-51.
[15] S. Cetin, S. Veli, S. Ayberk, An investigation of halogens in Izmit hazardous and clinical waste incinerator, Waste Management 24(2) (2004) 183-191.
[16] S. Enestam, C. Boman, J. Niemi, D. Boström, R. Backman, K. Mäkelä, M. Hupa, Occurrence of zinc and lead in aerosols and deposits in the fluidized-bed combustion of recovered waste wood. Part 1: Samples from boilers, Energy & Fuels 25(4) (2011) 1396-1404.
[17] S. Enestam, R. Backman, K. Mäkelä, M. Hupa, Evaluation of the condensation behavior of lead and zinc in BFB combustion of recovered waste wood, Fuel Processing Technology 105 (2013) 161-169.
[18] D. Lindberg, C. Molin, M. Hupa, Thermal treatment of solid residues from WtE units: A review, Waste Management 37 (2015) 82-94.
[19] J. Werkelin, B.-J. Skrifvars, M. Hupa, Ash-forming elements in four Scandinavian wood species. Part 1: Summer harvest, Biomass and Bioenergy 29(6) (2005) 451-466.
[20] L.L. Baxter, T.R. Miles, T.R. Miles Jr., B.M. Jenkins, T. Milne, D. Dayton, R.W. Bryers, L.L. Oden, The behavior of inorganic material in biomass-fired power boilers: field and laboratory experiences, Fuel Processing Technology 54(1-3) (1998) 47-78.
[21] T.R. Miles, T.R. Miles Jr., L.L. Baxter, R.W. Bryers, B.M. Jenkins, L.L. Oden, Boiler deposits from firing biomass fuels, Biomass and Bioenergy 10(2-3) (1996) 125-138.
[22] W. Ma, G. Hoffmann, M. Schirmer, G. Chen, V.S. Rotter, Chlorine characterization and thermal behavior in MSW and RDF, Journal of Hazardous Materials 178(1-3) (2010) 489-498.
[23] D. Bankiewicz, Corrosion behaviour of boiler tube materials during combustion of fuels containing Zn and Pb, Åbo Akademi University, 2012.
[24] D.W. Reeve, H.N. Tran, D. Barham, Superheater Fireside Deposits and Corrosion in Kraft Recovery Boilers, Tappi Journal 64(5) (1981) 109-113.
[25] K. Nakamura, S. Kinoshita, H. Takatsuki, The origin and behavior of lead, cadmium and antimony in MSW incinerator, Waste Management 16(5-6) (1996) 509-517.
[26] J. Krook, A. Mårtensson, M. Eklund, Sources of heavy metal contamination in Swedish wood waste used for combustion, Waste Management 26(2) (2006) 158-166.
[27] M. Lapuerta, A. Acosta, A. Pazo, Fouling Deposits from Residual Biomass with High Sodium Content in Power Plants, Energy & Fuels 29(8) (2015) 5007-5017.

[28] J. Jermer, A. Ekvall, C. Tullin, Inventory of contaminants in waste wood, Värmeforsk service AB, Stockholm, Sweden, 2001.
[29] R. Backman, M. Hupa, E. Uppstu, Fouling and corrosion mechanisms in the recovery boiler superheater area, TAPPI Journal 70(6) (1987) 123-127.
[30] U. Kleinhans, C. Wieland, F.J. Frandsen, H. Spliethoff, Ash formation and deposition in coal and biomass fired combustion systems: Progress and challenges in the field of ash particle sticking and rebound behavior, Progress in Energy and Combustion Science 68 (2018) 65-168.
[31] M. Broström, S. Enestam, R. Backman, K. Mäkelä, Condensation in the KCl–NaCl system, Fuel Processing Technology 105 (2013) 142-148.
[32] Y. Wang, H. Tan, Condensation of KCl(g) under varied temperature gradient, Fuel 237 (2019) 1141-1150.
[33] H.N. Tran, X. Mao, D.C.S. Kuhn, R. Backman, M. Hupa, The sticky temperature of recovery boiler fireside deposits, Pulp & Paper-Canada 103(9) (2002) 29-33.
[34] M. Theis, B.-J. Skrifvars, M. Zevenhoven, M. Hupa, H. Tran, Fouling tendency of ash resulting from burning mixtures of biofuels. Part 2: Deposit chemistry, Fuel 85(14-15) (2006) 1992-2001.
[35] K. Iisa, Y. Lu, K. Salmenoja, Sulfation of potassium chloride at combustion conditions, Energy & Fuels 13(6) (1999) 1184-1190.
[36] E.A. Olevsky, Theory of sintering: from discrete to continuum, Materials Science & Engineering R-Reports 23(2) (1998) 41-100.
[37] R.M. German, P. Suri, S.J. Park, Review: liquid phase sintering, Journal of Materials Science 44(1) (2009) 1-39.
[38] B.J. Skrifvars, M. Hupa, R. Backman, M. Hiltunen, Sintering mechanisms of FBC ashes, Fuel 73(2) (1994) 171-176.
[39] W.J. Frederick Jr., A. Ling, H.N. Tran, S.J. Lien, Mechanisms of sintering of alkali metal salt aerosol deposits in recovery boilers, Fuel 83(11-12) (2004) 1659–1664.
[40] H.N. Tran, D. Barham, D.W. Reeve, Sintering of Fireside Deposits and its Impact on Plugging in Kraft Recovery Boilers, Tappi Journal 71(4) (1988) 109-113.
[41] H. Zhou, W. Ma, An experimental study on the effects of adding biomass ashes on ash sintering behavior of Zhundong coal, Applied Thermal Engineering 126 (2017) 689-701.
[42] Y. Laxminarayan, P.A. Jensen, H. Wu, F.J. Frandsen, B. Sander, P. Glarborg, Deposit Shedding in Biomass-Fired Boilers: Shear Adhesion Strength Measurements, Energy & Fuels 31(8) (2017) 8733-8741.
[43] Y. Laxminarayan, A.B. Nair, P.A. Jensen, H. Wu, F.J. Frandsen, B. Sander, P. Glarborg, Tensile Adhesion Strength of Biomass Ash Deposits: Effect of the

Temperature Gradient and Ash Chemistry, Energy & Fuels 32(4) (2018) 4432-4441.
[44] H. Kinnunen, D. Lindberg, T. Laurén, M. Uusitalo, D. Bankiewicz, S. Enestam, P. Yrjas, High-temperature corrosion due to lead chloride mixtures simulating fireside deposits in boilers firing recycled wood, Fuel Processing Technology 167 (2017) 306-313.
[45] A.L. Robinson, S.G. Buckley, N. Yang, L.L. Baxter, Experimental measurements of the thermal conductivity of ash deposits: Part 2. Effects of sintering and deposit microstructure, Energy & Fuels 15(1) (2001) 75-84.
[46] Y. Kawahara, Evaluation of high-temperature corrosion life using temperature gradient corrosion test with thermal cycle component in waste combustion environments, Materials and Corrosion 57(1) (2006) 60-72.
[47] H.P. Michelsen, F. Frandsen, K. Dam-Johansen, O.H. Larsen, Deposition and high temperature corrosion in a 10 MW straw fired boiler, Fuel Processing Technology 54(1-3) (1998) 95-108.
[48] J. Lagerbom, T. Lepistö, R. Backman, M. Hupa, Behavior of alkaline sulfate-chloride salts in temperature gradient corrosion test furnace, VTT Symp, 2001, pp. 541-551.
[49] A. Zbogar, F. Frandsen, P.A. Jensen, P. Glarborg, Shedding of ash deposits, Progress in Energy and Combustion Science 35(1) (2009) 31-56.
[50] R.E. Carter, J.S. Nadeau, J.H. Rosolowski, Temperature Gradient Induced Migration of Helium Filled Pores in KCl, Journal of Nuclear Materials 30(1-2) (1969) 166-169.
[51] R.E. Carter, J.H. Rosolowski, J.S. Nadeau, Temperature Gradient Induced Migration of Gas-Filled Bubbles in KCl, Journal of Applied Physics 42(6) (1971) 2186-2193.
[52] J.S. Nadeau, R.E. Carter, J.H. Rosokowski, Morphology of Migrating Bubbles in KCl crystals, Journal of Applied Physics 42(6) (1971) 2194-2202.
[53] P.J. Lemaire, H.K. Bowen, Migration of Large Gas-filled Pores in Potassium Chloride Due to a Temperature Gradient, Journal of the American Ceramic Society 65(1) (1982) 41-48.
[54] P.J. Lemaire, H.K. Bowen, Migration of Small Pores in Potassium Chloride Due to a Temperature Gradient, Journal of the American Ceramic Society 65(1) (1982) 49-52.
[55] F.A. Nichols, Kinetics of Diffusional Motion of Pores in Solids, Journal of Nuclear Materials 30(1-2) (1969) 143-165.
[56] W.G. Pfann, TEMPERATURE GRADIENT ZONE MELTING, Transactions of the American Institute of Mining and Metallurgical Engineers 203(9) (1955) 961-964.

[57] M. Rettenmayr, Melting and remelting phenomena, International Materials Reviews 54(1) (2009) 1-17.
[58] W.A. Tiller, Migration of a Liquid Zone through a Solid: Part I, Journal of Applied Physics 34(9) (1963) 2757-2762.
[59] P.A. Jensen, F.J. Frandsen, J. Hansen, K. Dam-Johansen, N. Henriksen, S. Hörlyck, SEM investigation of superheater deposits from biomass-fired boilers, Energy & Fuels 18(2) (2004) 378-384.
[60] L.A. Hansen, H.P. Nielsen, F.J. Frandsen, K. Dam-Johansen, S. Horlyck, A. Karlsson, Influence of deposit formation on corrosion at a straw-fired boiler, Fuel Processing Technology 64(1-3) (2000) 189-209.
[61] D. Wu, K.V. Dahl, J.L. Madsen, T.L. Christiansen, M. Montgomery, J. Hald, Effects of Different Fuel Specifications and Operation Conditions on the Performance of Coated and Uncoated Superheater Tubes in Two Different Biomass-Fired Boilers, ACS Applied Energy Materials 1(4) (2018) 1463–1475.
[62] C.W. Bale, E. Belisle, P. Chartrand, S.A. Decterov, G. Eriksson, A.E. Gheribi, K. Hack, I.H. Jung, Y.B. Kang, J. Melancon, A.D. Pelton, S. Petersen, C. Robelin, J. Sangster, P. Spencer, M.A. Van Ende, FactSage thermochemical software and databases, 2010-2016, Calphad-Computer Coupling of Phase Diagrams and Thermochemistry 54 (2016) 35-53.
[63] M. Broström, H. Kassman, A. Helgesson, M. Berg, C. Andersson, R. Backman, A. Nordin, Sulfation of corrosive alkali chlorides by ammonium sulfate in a biomass fired CFB boiler, Fuel Processing Technology 88(11-12) (2007) 1171-1177.
[64] D.S. Costa, F.A. Paoliello, Experience of recovery boiler superheater corrosion at Cenibra, International Chemical Recovery Conference, Halifax, Nova Scotia, Canada, 2017.
[65] K. Persson, M. Broström, J. Carlsson, A. Nordin, R. Backman, High temperature corrosion in a 65 MW waste to energy plant, Fuel Processing Technology 88(11-12) (2007) 1178-1182.
[66] H. Kinnunen, M. Hedman, M. Engblom, D. Lindberg, M. Uusitalo, S. Enestam, P. Yrjas, The influence of flue gas temperature on lead chloride induced high temperature corrosion, Fuel 196 (2017) 241-251.
[67] M. Hedman, H. Kinnunen, N. Engblom, S. Enestam, Presence and behaviour of lead in a full-scale waste wood fired BFB-boiler, Nordic Flame Days, Stockholm, Sweden, 2017.
[68] P. Vainikka, S. Enestam, J. Silvennoinen, R. Taipale, P. Yrjas, A. Frantsi, J. Hannula, M. Hupa, Bromine as an ash forming element in a fluidised bed boiler combusting solid recovered fuel, Fuel 90(3) (2011) 1101-1112.

[69] P. Vainikka, D. Bankiewicz, A. Frantsi, J. Silvennoinen, J. Hannula, P. Yrjas, M. Hupa, High temperature corrosion of boiler waterwalls induced by chlorides and bromides. Part 1: Occurrence of the corrosive ash forming elements in a fluidised bed boiler co-firing solid recovered fuel, Fuel 90(5) (2011) 2055-2063.
[70] D. Lindberg, R. Backman, P. Chartrand, Thermodynamic evaluation and optimization of the ($NaCl+Na_2SO_4+Na_2CO_3+KCl+K_2SO_4+K_2CO_3$) system, The Journal of Chemical Thermodynamics 39(7) (2007) 1001-1021.
[71] M. Engblom, D. Lindberg, J. Niemi, M. Hupa, Mathematical Modeling of Intradeposit Alkali Chloride Enrichment in Biofuel Boiler Superheaters, Impacts of Fuel Quality on Power Production, The 26th International Conference, Prague, Czech Republic, 2016.
[72] P. Vainikka, Occurrence of bromine in fluidised bed combustion of solid recovered fuel, VTT Publication 778, VTT Technical Research Centre of Finland, 2011.
[73] H. Wu, P. Yrjas, M. Hupa, Laboratory Studies of Potassium-Halide-Induced High-Temperature Corrosion of Superheater Steels. Part 1: Exposures in Dry Air, Energy & Fuels 29(2) (2015) 1186-1195.
[74] H. Wu, D. Bankiewicz, P. Yrjas, M. Hupa, Laboratory Studies of Potassium-Halide-Induced High-Temperature Corrosion of Superheater Steels. Part 2: Exposures in Wet Air, Energy & Fuels 29(4) (2015) 2709-2718.
[75] S. Lee, S. Tsujikawa, Corrosion behavior of Fe-Cr and Fe-Ni-base commercial alloys in flowing Ar-42.6%O_2-14.7%Br_2 gas mixture at 700 degrees °C, Materials and Corrosion 48(6) (1997) 364-371.
[76] J. Lehmusto, M. Bergelin, J.-O. Lill, Production and use of radioactive [^{82}Br]KBr in high-temperature corrosion studies, Corrosion Science 148 (2019) 24-30.
[77] D. Bankiewicz, P. Vainikka, D. Lindberg, A. Frantsi, J. Silvennoinen, P. Yrjas, M. Hupa, High temperature corrosion of boiler waterwalls induced by chlorides and bromides - Part 2: Lab-scale corrosion tests and thermodynamic equilibrium modeling of ash and gaseous species, Fuel 94 (2012) 240-250.
[78] H.J. Grabke, E. Reese, M. Spiegel, The effects of chlorides, hydrogen chloride, and sulfur dioxide in the oxidation of steels below deposits, Corrosion Science 37(7) (1995) 1023-1043.
[79] N. Folkeson, T. Jonsson, M. Halvarsson, L.-G. Johansson, J.-E. Svensson, The influence of small amounts of KCl(s) on the high temperature corrosion of a Fe-2.25Cr-1Mo steel at 400 and 500°C, Materials and Corrosion 62(7) (2011) 606-615.
[80] H.T. Ma, C.H. Zhou, L. Wang, High temperature corrosion of pure Fe, Cr and Fe-Cr binary alloys in O_2 containing trace KCl vapour at 750 °C, Corrosion Science 51(8) (2009) 1861-1867.

[81] A. Talus, R. Norling, L. Wickström, A. Hjörnhede, Effect of Lead Content in Used Wood Fuel on Furnace Wall Corrosion of 16Mo3, 304L and Alloy 625, Oxidation of Metals 87(5-6) (2017) 813-824.
[82] M. Spiegel, Salt melt induced corrosion of metallic materials in waste incineration plants, Materials and Corrosion 50(7) (1999) 373-393.
[83] B.-J. Skrifvars, R. Backman, M. Hupa, K. Salmenoja, E. Vakkilainen, Corrosion of superheater steel materials under alkali salt deposits Part 1: The effect of salt deposit composition and temperature, Corrosion Science 50(5) (2008) 1274-1282.
[84] H.P. Nielsen, F.J. Frandsen, K. Dam-Johansen, L.L. Baxter, The implications of chlorine-associated corrosion on the operation of biomass-fired boilers, Progress in Energy and Combustion Science 26(3) (2000) 283-298.
[85] P. Viklund, A. Hjörnhede, P. Henderson, A. Stålenheim, R. Pettersson, Corrosion of superheater materials in a waste-to-energy plant, Fuel Processing Technology 105 (2013) 106-112.
[86] J. Lehmusto, P. Yrjas, B.-J. Skrifvars, M. Hupa, High temperature corrosion of superheater steels by KCl and K_2CO_3 under dry and wet conditions, Fuel Processing Technology 104 (2012) 253-264.
[87] A. Talus, H. Kinnunen, R. Norling, S. Enestam, Corrosion of carbon steel underneath a lead/potassium chloride salt mixture, Materials and Corrosion 70(8) (2019) 1450-1460.
[88] J.M. Brossard, I. Diop, X. Chaucherie, F. Nicol, C. Rapin, M. Vilasi, Superheater fireside corrosion mechanisms in MSWI plants: Lab-scale study and on-site results, Materials and Corrosion 62(6) (2011) 543-548.
[89] Y. Liu, W. Fan, X. Zhang, X. Wu, High-Temperature Corrosion Properties of Boiler Steels under a Simulated High-Chlorine Coal-Firing Atmosphere, Energy & Fuels 31(4) (2017) 4391-4399.
[90] B.S. Covino Jr., G.R. Holcomb, S.D. Cramer, S.J. Bullard, M. Ziomek-Moroz, M.L. White, Corrosion in a temperature gradient, 17th Annual Conference on Fossil Energy Materials (2003).
[91] R. Shenassa, H. Tran, D.C.S. Kuhn, Dynamic study of carryover deposition in kraft recovery boilers using an entrained flow reactor, Pulp & Paper-Canada 100(10) (1999) 56-62.
[92] R.F. Rea, Temperature-measuring cones, Journal of the American Ceramic Society 21 (1938) 98-101.
[93] A.P. Palkin, S.D. Gromakov, P.F. Reshetnikov, N.I. Semenov, M.G. Turusov, Ternary fusibility systems, Acta Univ. Voronegiensis (U. S. S. R.) 10(4) (1939) 5-39.

[94] S.D. Gromakov, Some rules pertaining to the determination of the type of phase diagrams of binary systems, Zhurnal Fizicheskoi Khimii 25 (1951) 1014-1025.
[95] H. Flood, T. Forland, A. Nesland, Cryoscopic measurements in fused salts at elevated temperatures, Acta Chemica Scandinavica 5 (1951) 1193-1198.
[96] R.N. Nyankovskaya, Fusion diagram for the system of the sulfates and bromides of sodium and potassium, Zhurnal Neorganicheskoi Khimii 4 (1959) 2591-2595.
[97] A.D. Pelton, P. Chartrand, G. Eriksson, The modified quasi-chemical model: Part IV. Two-sublattice quadruplet approximation, Metallurgical and Materials Transactions a-Physical Metallurgy and Materials Science 32(6) (2001) 1409-1416.
[98] D.R. Lide, CRC Handbook of Chemistry and Physics, 84th ed., CRC Press, New York, 2003.
[99] P.D. McCaffrey, R.J. Mawhorter, A.R. Turner, P.T. Brain, D.W.H. Rankin, Accurate Equilibrium Structures Obtained from Gas-Phase Electron Diffraction Data: Sodium Chloride, Journal of Physical Chemistry A 111(27) (2007) 6103-6114.
[100] T. Torring, S. Biermann, J. Hoeft, R. Mawhorter, R.J. Cave, C. Szemenyei, The structure of alkali halide dimers: A critical test of ionic models and new ab initio results (vol 104, pg 8032, 1996), Journal of Chemical Physics 124(7) (2006).
[101] T. Torring, S. Biermann, J. Hoeft, R. Mawhorter, R.J. Cave, C. Szemenyei, The structure of alkali halide dimers: A critical test of ionic models and new ab initio results, Journal of Chemical Physics 104(20) (1996) 8032-8042.
[102] R.D. Shannon, Revised effective ionic radii and systematic studies of interatomic distances in halides and chalcogenides, Acta Crystallographica Section A 32(SEP1) (1976) 751-767.
[103] L. Shen, Z.X. Chen, Critical review of the impact of tortuosity on diffusion, Chemical Engineering Science 62(14) (2007) 3748-3755.
[104] J.W. Beeckman, Mathematical description of heterogeneous materials, Chemical Engineering Science 45(8) (1990) 2603-2610.
[105] D.H. Kerridge, A. Horsewell, R.W. Berg, The structure of solid salt eutectics - Why lamellar or conglomerate?, Solid State Ionics 180(28-31) (2009) 1453-1456.
[106] A. Gabriel, A.D. Pelton, Phase diagram measurements and thermodynamic analysis of the $PbCl_2$–NaCl, $PbCl_2$–KCl, and $PbCl_2$–KCl–NaCl systems, Canadian Journal of Chemistry 63(11) (1985) 3276-3282.
[107] A.V. Knyazev, E.N. Bulanov, N.N. Smirnova, V.Z. Korokin, A.N. Shushunov, A.G. Blokhina, Low-temperature heat capacity and thermal expansion of synthetic caracolite $Na_3Pb_2(SO_4)_3Cl$, Thermochimica Acta 596 (2014) 1-5.

[108] S.M. Lee, S.-J.L. Kang, Theoretical analysis of liquid-phase sintering: Pore filling theory, Acta Materialia 46(9) (1998) 3191-3202.
[109] H. Engelhardt, M. Rettenmayr, Diffusion in a temperature gradient – A single cycle method to determine frequency factor and activation energy of solid diffusion coefficients in alloys, Acta Materialia 95 (2015) 212-215.
[110] M. Perrut, A. Parisi, S. Akamatsu, S. Bottin-Rousseau, G. Faivre, M. Plapp, Role of transverse temperature gradients in the generation of lamellar eutectic solidification patterns, Acta Materialia 58(5) (2010) 1761-1769.
[111] D. Lindberg, J. Niemi, M. Engblom, T. Laurén, P. Yrjas, M. Hupa, Experimental and modeling approaches to simulate temperature-gradient induced intradeposit chemical processes with implications for biomass boiler corrosion, 23rd International Conference on Fluidized Bed Conversion, Seoul, South Korea, 2018.
[112] S. Enestam, D. Bankiewicz, J. Tuiremo, K. Mäkelä, M. Hupa, Are NaCl and KCl equally corrosive on superheater materials of steam boilers?, Fuel 104 (2013) 294-306.
[113] A. Zbogar, F.J. Frandsen, P.A. Jensen, P. Glarborg, Heat transfer in ash deposits: A modelling tool-box, Progress in Energy and Combustion Science 31(5-6) (2005) 371-421.
[114] H. Zhou, B. Zhou, H.L. Zhang, L.T. Li, K.F. Cen, Investigation of Slagging Characteristics in a 300 kW Test Furnace: Effect of Deposition Surface Temperature, Industrial & Engineering Chemistry Research 53(17) (2014) 7233-7246.
[115] B.-J. Skrifvars, M. Wésten-Karlsson, M. Hupa, K. Salmenoja, Corrosion of super-heater steel materials under alkali salt deposits. Part 2: SEM analyses of different steel materials, Corrosion Science 52(3) (2010) 1011-1019.
[116] Y.S. Li, M. Spiegel, S. Shimada, Corrosion behaviour of various model alloys with NaCl-KCl coating, Materials Chemistry and Physics 93(1) (2005) 217-223.
[117] C. Pettersson, J. Pettersson, H. Asteman, J.-E. Svensson, L.-G. Johansson, KCl-induced high temperature corrosion of the austenitic Fe–Cr–Ni alloys 304L and Sanicro 28 at 600 °C, Corrosion Science 48(6) (2006) 1368-1378.
[118] K. Treis, Crystallographic and thermal investigation of systems formed by lead chloride with the chlorides of univalent metals, Jahrb Min Beil-Bd 37 (1914) 766-818.

RECENT REPORTS FROM THE COMBUSTION AND MATERIALS RESEARCH GROUP OF THE JOHAN GADOLIN PROCESS CHEMISTRY CENTRE:

15-01	Petteri Kangas	Modelling the super-equilibria in thermal biomass conversion – Applications and limitations of the constrained free energy method
15-02	David Agar	The Feasibility of Torrefaction for the Co-Firing of Wood in Pulverised-Fuel Boilers
16-01	Tooran Khazraie Shoulaifar	Chemical Changes in Biomass during Torrefaction
16-02	Hao Wu	Chemistry of potassium halides and their role in corrosion in biomass and waste firing
19-01	Jingxin Sui	Initial Stages of Alkali Salt Induced High Temperature Corrosion Mechanisms
19-02	Hanna Kinnunen	The Role and Corrosivity of Lead in Recycled Wood Combustion

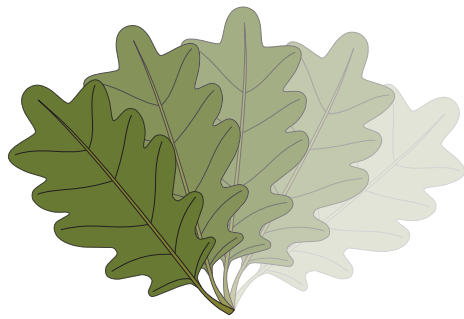

ISBN 978-952-12-3865-9 (printed)
ISBN 978-952-12-3866-6 (digital)
Turku, Finland, 2019

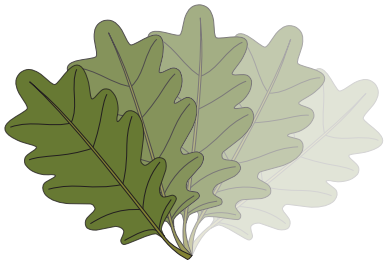

Johan Gadolin
Process Chemistry Centre

ISBN 978-952-12-3866-6